POLARIZED RADIATION AS TRACER OF MAGNETIC FIELDS IN STAR FORMATION

Dissertation
zur Erlangung des Doktorgrades
der Mathematisch-Naturwissenschaftlichen Falkultät
der Christian-Albrechts-Universität zu Kiel

vorgelegt von

GESA H.-M. BERTRANG

Kiel, 2015

Referent: Prof. Dr. Sebastian Wolf
Koreferent: Prof. Dr. Robert F. Wimmer-Schweingruber

Tag der mündlichen Prüfung: 18.09.2015
Zum Druck genehmigt: 18.09.2015

gez. Prof. Dr. Wolfgang J. Duschl, Dekan

If people sat outside and looked at the stars each night,
I'll bet they'd live a lot differently.

- Bill Watterson

Abstract

Magnetic fields are observed on a wide range of astronomical scales: from the entire cosmos, galaxies and giant molecular clouds, to smaller molecular clouds with low-mass star formation and protostellar disks, to protoplanetary disks. There is an ongoing debate about whether magnetic fields play an important role in star and planet formation. For a better understanding of the influence of magnetic fields during this process, it is necessary to study the magnetic fields on different evolutionary stages of star and planet formation with both observations and simulations. This is the goal of this thesis, which is therefore split into two parts.

The first part addresses the earliest phase of star formation and presents an observational multi-wavelength polarimetry study of low-mass star-forming regions. Until now, there exists no observational evidence of a general influence of magnetic fields during the initial collapse of molecular clouds. This study examines magnetic fields and their influence during the initial collapse of low-mass star-forming regions on a wide range of spatial scales. The large-scale magnetic field structure was traced on scales of $10^3 - 10^5$ AU in the local environment of the three Bok globules B335, CB68, and CB54, by optical and near-infrared polarimetry. These measurements are combined with existing sub-millimeter measurements characterizing the small-scale magnetic field structure on $10^2 - 10^3$ AU. For the first time, magnetic fields in three Bok globules with different complex density structures were found to be well-ordered and dominant on large scales.

The second part deals with a more evolved phase of star and planet formation, with protoplanetary disks. (Sub-)Millimeter observations of polarized radiation from protoplanetary disks enable us to study the magnetic fields within the disk. In the context of this thesis, the 3D radiative transfer code MC3D was extended by including the treatment of thermal polarization and dust grain alignment of non-spherical grains. These pioneering simulations achieve the characterization and theoretical explanation of observations of polarized radiation towards protoplanetary disks, performed for instance with the Atacama Large Millimeter/submillimeter Array (ALMA). In addition to these extensions of the radiative transfer simulations, this code can be combined with magnetohydrodynamic simulations. With this polarized radiative transfer code, it is possible to model polarization maps, intensity maps, as well as polarized and unpolarized spectral energy distributions of thermal dust emission and dichroic extinction that can be fitted to or constrained by observations. These simulations demonstrate the feasibility of polarimetry on protoplanetary disks with ALMA. With simulations and observations in combination, it is possible to distinguish between different models of protoplanetary disks and magnetic fields therein.

Zusammenfassung

Magnetfelder lassen sich auf allen astronomischen Größenskalen finden: von kosmischen Skalen, Galaxien und Riesenmolekülwolken, über kleinere, massearme Molekülwolken, bis hin zu protoplanetaren Scheiben. Die Frage, ob Magnetfelder eine wichtige Rolle in der Stern- und Planetenentstehung spielen, ist Gegenstand anhaltender Debatte. Um das Verständnis über den Einfluss von Magnetfeldern auf die Entstehung von Sternen und Planeten zu erweitern, ist es wichtig Magnetfelder auf den verschiedenen evolutionären Stufen der Stern- und Planetenentstehung mit Beobachtungen und Simulationen zu erforschen. Dies ist das Ziel der vorliegenden Arbeit, welche aus diesem Grund in zwei Teile gegliedert ist.

Der erste Teil behandelt die früheste Phase der Sternentstehung, und präsentiert eine Multiwellenlängenpolarisationsstudie, durchgeführt an massearmen Sternentstehungsregionen. Bis heute gibt es keinen Hinweis aus Beobachtungen für den generellen Einfluss von Magnetfeldern auf die initiale Phase des Kollapses der Molekülwolke. Ziel dieser Studie ist es, die Magnetfelder in diesen massearmen Molekülwolken zu untersuchen und ihren Einfluss auf den initialen Kollaps weitskalig zu erforschen. Hierzu wurde die großskalige Magnetfeldstruktur auf Skalen von $10^3 - 10^5$ AE in der lokalen Umgebung dreier Bok Globulen, B335, CB68 und CB54, mittels optischer und Nah-Infrarotpolarimetrie bestimmt, und kombiniert mit archivierten Daten aus dem Submillimeterbereich, welche das kleinskalige Magnetfeld auf Skalen von $10^2 - 10^3$ AE charakterisieren. Auf diese Weise wurden erstmalig geordnete und damit dominierende Magnetfeldstrukturen in drei verschieden komplexen Bok Globulen über weite Skalen hinweg gefunden.

Der zweite Teil beschäftigt sich mit einer fortgeschrittenen Phase der Stern- und Planetenentstehung, mit protoplanetaren Scheiben. Im Rahmen dieser Arbeit ist der 3D Strahlungstransportcode MC3D um die Effekte von thermischer Polarisation und Ausrichtung von asphärischen Staubkörnern an Magnetfeldern erweitert worden. Diese Simulationen gehören zu den ersten ihrer Art und dienen dazu Beobachtungen von polarisierter Strahlung von protoplanetaren Scheiben zu charakterisieren und theoretisch zu fundieren, welche etwa mit dem Atacama Large Millimeter/submillimeter Array (ALMA) durchgeführt werden können. Zusätzlich wurde MC3D angepasst, um die aus Magnetohydrodynamiksimulationen resultierenden Staubdichteverteilungen und Magnetfelder zu verarbeiten. Mit diesem Strahlungstransportcode ist es nun möglich Polarisationskarten, Intensitätskarten, sowie polarisierte und unpolarisierte spektrale Energieverteilungen thermischer Staubemission und dichroitischer Absorption zu modellieren, welche zur Analyse und Vorhersage von Beobachtungsdaten dienen. Diese Simulationen demonstrieren die Machbarkeit polarimetrischer Beobachtungen protoplanetarer Scheiben mit ALMA. Mit beidem in Kombination gelingt es unterschiedliche Modelle von protoplanetaren Scheiben und ihren Magnetfeldern zu differenzieren.

Contents

1. Introduction

Magnetic fields are a matter of human interest since early civilizations. Aristotle was discussing magnetism with Thales of Miletus (Fowler 1997), while in ancient India, the Indian surgeon Sushruta was using a magnet for surgical purposes (Vowles 1932). Nowadays, we encounter magnetic fields routinely in our daily life, in computers, in engines, in medical equipment. We learned that magnetic fields shield us from cosmic rays (e.g., Tarduno et al. 2010), we even measure them in the sun and trace them up to the border of our solar system (e.g., Burlaga et al. 2013). Naturally, we ask where they originate and when they were created for the first time. Current research on the origin of the first magnetic field, the primordial magnetic field, is going back to the earliest moments of the universe. The primordial magnetic field could have been generated by i) quantum perturbations during the phase of inflation (e.g., Liddle & Lyth 2000), it could have been generated by ii) cosmological electroweak phase transitions (e.g., Quashnock et al. 1989), or the primordial magnetic field could have been generated by iii) dynamo effects during and after the epoch of photon last scattering (e.g., Ichiki et al. 2006). Despite of the differences of these approaches, all of them assume that magnetic fields have originated at some point in the very young universe. Since then, they have spread throughout the universe. We find magnetic fields everywhere in the cosmos, yet, we do not know much about their role in shaping the cosmos by the formation of galaxies, stars, and planets. Approximately 99% of the visible material in the universe is in a plasma state (e.g., Mrówczyński & Thoma 2007) and can therefore be influenced by magnetic forces. Under certain circumstances, the same applies to solid bodies such as dust grains (e.g., Andersson 2015). High sensitivity observations of galactic halos have revealed a general X pattern of magnetic fields within these halos. These so-called X-shape magnetic fields are characterized by a vertical (i.e., perpendicular to the galactic disk plane) component that increases with both galactic radius and height in the four quadrants (e.g., Krause 2009). The same magnetic field pattern is predicted for regions of low-mass, i.e., sun-like star formation (e.g., Crutcher 2006), though, it is observed significantly less often. The processes that lead to this magnetic field structures are the same. It is assumed that gas and dust in interstellar space is accumulated into clouds that become at some point massive enough to start collapsing under the action of their own gravity, and by this, form a new star. By the effect of optical depth, the cloud shields its interior from cosmic rays. Thereby, the atoms in the gas are able to form molecules that will not immediately be destroyed by high energetic radiation. Some molecules stay in gas phase, and some condensate on dust grain surfaces. A certain amount of the matter is ionized, and the cloud is permeated by the homogenous local interstellar magnetic field. Now that the cloud is collapsing, its material begins to behave differently depending on its ionization state. While the electrically neutral gas and dust particles are driven mainly by gravity, the ionized particles are coupled to the magnetic field and follow gravity only parallel to the magnetic field lines. After a while, enough material collapsed towards the center and by this, enhances the density in the mid-plane of the cloud. At that point, the ionized particles in the mid-plane do not only experience gravitational and magnetic forces, but additionally, collisions occur between ionized particles and neutral particles that still move towards the center of the cloud. This results in a net motion of the ionized particles perpendicular to the magnetic field line towards the center of the cloud. The ionized particles drag the magnetic field lines with them. Of course, this is only possible if the magnetic field strength is high enough to hold the ionized particles but weak enough to allow movement perpendicular to its field lines due to collisions. These processes result in the X shape structure of the magnetic field in the star-forming cloud (e.g., Mouschovias & Ciolek 1999; Vallée 2002; Crutcher 2006). The common term for this field configuration in the star formation community is hour-glass shape (see Fig.1.1).

This hourglass-shaped magnetic field was observed for the first time in the low-mass star-forming region NGC 1333 IRAS 4A (Girart et al. 2006; see Fig. 1.1). This is only one of three observations that show this magnetic field structure in these

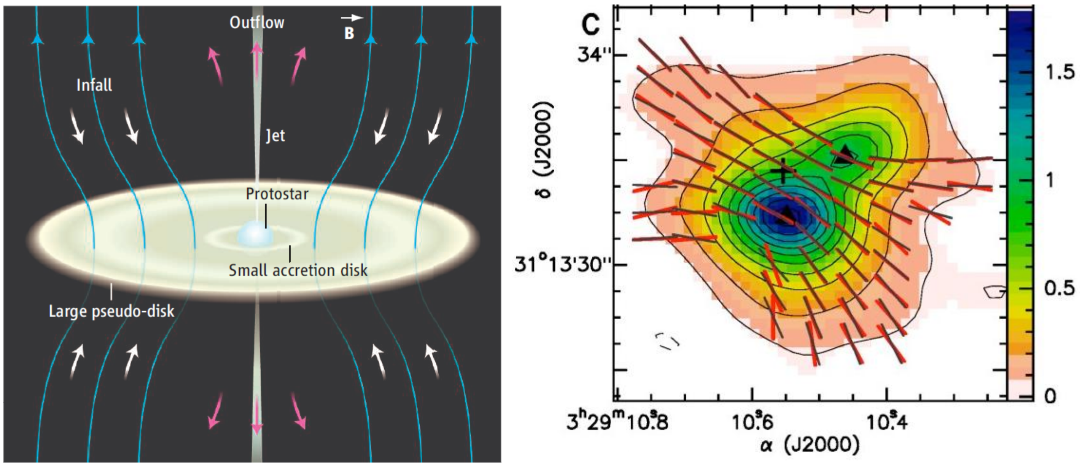

Fig. 1.1.: The magnetic field structure in low-mass star formation resulting from the collapse of the cloud is an hourglass shape (*left*; artistic impression from Crutcher 2006; reprinted with permission from AAAS). For the first time this magnetic field structure (red lines, *right*) was found in the low-mass star-forming region NGC 1333 IRAS 4A (from Girart et al. 2006; reprinted with permission from AAAS).

objects. Due to the lack of observational constrains, the role of magnetic fields in low-mass star formation is still in debate. Since magnetic fields cannot be measured directly, magnetic field observations are in fact observations of polarized radiation that make use of the dust contained in the cloud. Atoms merge and build molecules which then become even larger until they stop binding chemically but physically. When that happens they have typical sizes of a few nanometers and are considered to be dust grains. This process of growth will most likely not result in perfect spheres. Thus, it is a good assumption that we deal with non-spherical grains. Similar to iron filings, these non-spherical dust grains trace magnetic field lines, and because of their non-spherical shape, they polarize light. Both of these properties are used to measure magnetic fields in distances we cannot access with probes. But polarization measurements are very sensitive to many effects that complicate the identification of the magnetic field from the signal. Important effects are the projection along the line of sight and, connected to this, the influence of noise signals. Recent publications of BICEP2, PLANCK, and the Keck Array (Ade et al. 2014; BICEP2/Keck and Planck Collaborations et al. 2015) demonstrated that accurate analysis of potential noise signals is absolutely essential for a proper analysis of polarimetric data. Keeping this in mind, this thesis seeks to take new paths in the research on the role of magnetic fields in low-mass star formation by both multi-wavelength polarization observations and sophisticated radiative transfer simulations of polarized dust emission. In the context of the multi-wavelength polarization study it shall be demonstrated that magnetic fields are dominant on large scales in low-mass star-forming regions of various grades of geometric complexity. The goal of the second part of this thesis has been the development of one of the first radiative transfer codes capable of simulating the polarized dust emission of aligned non-spherical grains within protoplanetary disks.

This thesis starts with the basic physics of magnetic fields in star formation (chapter 2), continues with part I of this thesis which describes the observational work (chapter 3, 4), while part II of this thesis is devoted to the computational work (chapter 5, 6), the concluding remarks, summary and outlook, complete this thesis in chapter 7.

2. Physics of magnetic fields in star formation

In star formation, indications of magnetic fields are found on a wide range of scales. On the largest scales of about $10 - 1000\,\mathrm{pc}$ there are massive star-forming regions, also known as Giant Molecular Clouds (GMCs, see Fig. 2.1). The main questions about magnetic fields on these scales concern the origin of and the coupling between the magnetic field of the GMC and the galactic magnetic field (e.g., Li & Henning 2011; Stephens et al. 2011). On the intermediate scales of star formation of about $0.1 - 1\,\mathrm{pc}$, there are smaller, less massive molecular clouds, also called Bok globules, which are regions of low-mass star formation (see Fig. 2.2). The role of magnetic fields on the low-mass star formation process is described in detail in Sect. 2.1. On the smallest scales, smaller than $0.1\,\mathrm{pc}$, there are protoplanetary systems, a protostar surrounded by a protoplanetary disk (see Fig. 2.3). These protoplanetary systems will evolve into planetary systems (for details, see Sect. 2.2). During the transformation from the protoplanetary system to the planetary system, the gas component of the system needs to be dispersed as well as angular momentum must be extracted. Both conditions can be explained by the influence of magnetic fields within the protoplanetary system (e.g., Pudritz et al. 2007; Suzuki & Inutsuka 2009). Additionally, the accretion of gas and dust from the inner edge of the protoplanetary disk onto the protostar can be explained by magnetically-channeled accretion along the magnetic field lines onto the star (e.g., Bouvier et al. 2007). This stage of star formation is the focus of the second part of this thesis (see chapters 5, 6).

Evidently, magnetic fields do play some role in star formation. This thesis is committed to the influence of magnetic fields in low-mass star formation in the intermediate and small scales as defined above. In this chapter, the physical basics and ideas of this field are presented. The concepts and models discussed here form the basis of this thesis. Theoretical background concerning only the observational part of this thesis or only the computational part of this thesis, is described in the corresponding chapter (chapter 3, resp. chapter 5).

2.1. Magnetic fields in low-mass star formation

To understand the role of magnetic fields in low-mass star formation, it is necessary to understand the idea of this process. Therefore, this section addresses the current

Fig. 2.1.: The Carina Nebula, for example, is a giant molecular cloud (GMC). GMCs have a typical span of 10 − 1000 pc. Inside the GMC, clusters of massive stars are forming (NASA/ESA/M. Livio, The Hubble Heritage Team & Hubble 20th Anniversary Team (STScI), Id 225225).

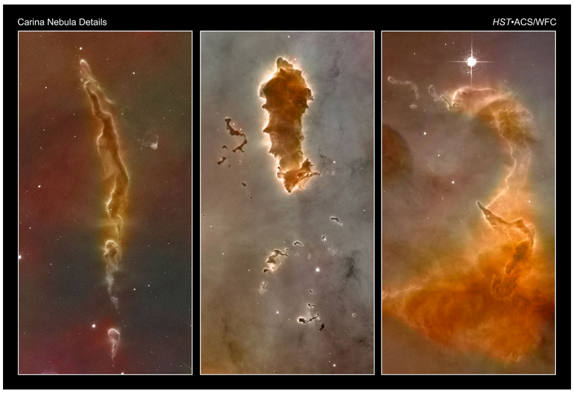

Fig. 2.2.: Bok globules are a common place of low-mass, i.e., sun-like star formation. Bok globules have a typical span of 0.1 − 1 pc. (NASA, ESA, N. Smith (University of California, Berkeley), and The Hubble Heritage Team (STScI/AURA)).

Fig. 2.3.: Protoplanetary systems, here shown in an artistic impression, are composed of a protostar that is surrounded by a protoplanetary disks and will evolve into a planetary system. They have a typical span of less than 0.1 pc (NASA/JPL-Caltech).

state of research on the low-mass star formation, and describes the role of magnetic fields during this process.

Low-mass star-forming regions, Bok globules (see Fig. 2.2), are relatively isolated molecular clouds. They contain molecules that can form deeply embedded inside the globule since the dense gas and dust shield them from the highly energetic interstellar radiation. They have simple structures and are small in diameter ($0.1 - 2\,\mathrm{pc}$; Clemens et al. 1991) with masses of $2 - 100\,\mathrm{M}_\odot$ (Bok 1977). These objects are common places of low-mass star formation. They inhibit bipolar molecular outflows, infrared colors, and sub-mm properties that are consistent with embedded Class 0 or Class I objects (e.g., Launhardt & Henning 1997; see Sect. 2.2).

The basic idea of star formation is well accepted. The star-forming region, the slowly rotating molecular cloud, is undergoing a self-gravitational collapse. Radially dependent, pressure and temperature increase until nuclear fusion starts in the center of the cloud - the protostar is formed and surrounded by a protostellar disk, a result of angular momentum conversation. The protoplanetary system evolves, planets form from the disk. A planetary system is created (see Fig. 2.4 and Sec. 2.2). By applying this scheme, the star formation rate (SFR), the newly formed stellar mass per year per selected test volume, can be determined theoretically (e.g., Agertz et al. 2013). Comparisons of the theoretically predicted SFR and SFRs derived from observations reveal that both values deviate from each other significantly by $\mathrm{SFR}_{\mathrm{theo}} \approx 100 \times \mathrm{SFR}_{\mathrm{obs}}$ (e.g., Kennicutt & Evans 2012). This deviation indicates that the star formation process is influenced by an effect that slows down the gravitational collapse of the globule and has been neglected in the scheme so far (e.g., Padoan et al. 2013; and references therein). Several processes and effects have been suggested, the two most important ones are turbulences and magnetic fields. Bok globules do not show any sign of strong turbulences (e.g., Epstein 1977; Yen et al. 2014), thus, a dominant influence of magnetic fields is the preferred process to explain the observed lower SFR for low-mass star formation. The predicted influence of magnetic fields on the contraction time-scale of low-mass star forming-regions is described in the following.

Magnetic fields permeate Bok globules and are coupled to the ionized particles within the globule (see Fig. 2.5). As a result of collisions between ionized and neutral particles, the coupling of the ionized particles and the magnetic field slows down the gravitational collapse. This happens under the condition that the coupling is strong enough, i.e., if the magnetic field is strong enough to dominate against gravity (e.g., Crutcher 2006; Mouschovias & Ciolek 1999). In that case, ordered magnetic field lines are expected. If, contrarily, the magnetic field is too weak to resist gravity, the magnetic field lines will be carried along with the self-gravitational collapsing gas and dust. In the latter case, random magnetic field structures are expected. Thus, the key to verify the magnetic field influence on low-mass star formation is the determination of the magnetic field structure. However, magnetic fields cannot be measured directly, since astronomical objects are simply too far away. For that reason, astronomers make use of the dust grains in molecular clouds. Just like non-spherical iron grains being aligned by magnetic fields can be used on Earth to trace the field line structure, non-spherical dust grains that are aligned by the magnetic field are used to trace the magnetic field structure in space. Because dust grains are natural polarizers of electromagnetic radiation, their alignment with the magnetic fields in Bok globules hundreds of parsecs away can be traced (see Sect. 2.4.2). Therefore, observations of the polarized radiation reveal the magnetic field structure (see Sect. 2.3). This way, the influence of magnetic fields on the low-mass star-forming process can be verified.

In the following, an introduction of the different stages of star formation is given in Sect. 2.2, Sect. 2.3 addresses the basics of polarization, and Sect. 2.4 concludes with the basics of dust grains, the tracers of magnetic fields.

2.2. Stages of star formation

This thesis deals with several stages of star formation. For this reason, this section gives an overview on the evolutionary stages of young stellar objects (YSOs) which are divided into four classes, Class 0, I, II, and III (Lada & Wilking 1984; Lada 1987, 1999; see Fig. 2.6). This empirical classification scheme is based on observations of spectral energy distributions (SEDs), or more precisely, on the slope of the observed SEDs. This can be made more quantitative by defining the spectral index, α_{IR}, with

$$\alpha_{\mathrm{IR}} = \frac{\mathrm{d}\log(\lambda \mathrm{F}_\lambda)}{\mathrm{d}\log(\lambda)}\,, \tag{2.1}$$

for wavelengths, λ, between $2.2\,\mu$m and $25\,\mu$m, and fluxes F_λ. The four classes characterize the transformation of the molecular cloud into a planetary system, while Class 0 and Class I objects are protostars, and Class II and Class III objects are pre-main sequence stars. These classes are described in more detail in the following (e.g., Lada & Wilking 1984; Lada 1987, 1999; Williams & Cieza 2011).

Class 0 objects are the youngest objects that are called protostars. Class 0 objects are deeply embedded into the collapsing molecular cloud, the Bok globule, which they accrete. Yet, most of the mass of the resulting star is still bound to the globule. The protostar is not observable in the optical or near-IR, thus, α_{IR} is undetermined. However, due to the large amount of dust with temperatures of a few Kelvin, these objects radiate very efficiently in the sub-mm and mm wavelength range. Class 0 objects and the associated collimated bipolar molecular mass outflows are considered as typical signs of star formation in Bok globules.

The observational part of this thesis (see chapters 3, 4) is focused on this stage of star formation as well as on objects during the transition from Class 0 to Class I.

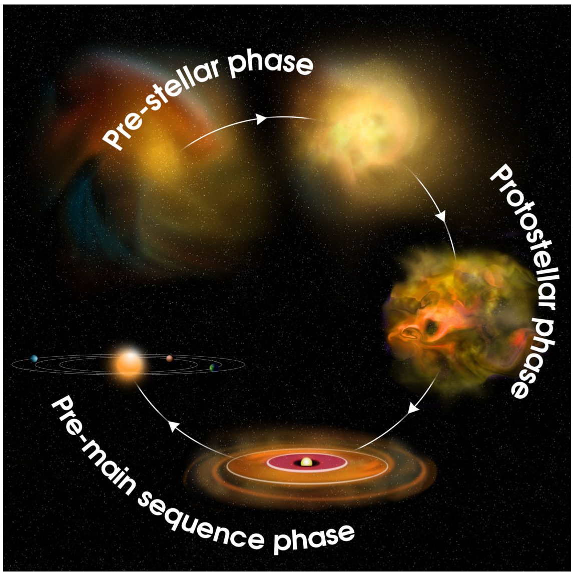

Fig. 2.4.: The theory of star and planet formation: Within giant clouds of gas and dust in interstellar space, clumps begin to form (pre-stellar phase) and within the clumps, dense cores are formed (Class 0 objects, see Sect. 2.2). These dense cores condense into young stars (protostellar phase, Class I objects) surrounded by dusty disks (pre-main sequence phase, Class II objects). Planets form from the disks, and a new solar system is born (Class III objects) (adapted from Bill Saxton/NRAO/AUI/NSF).

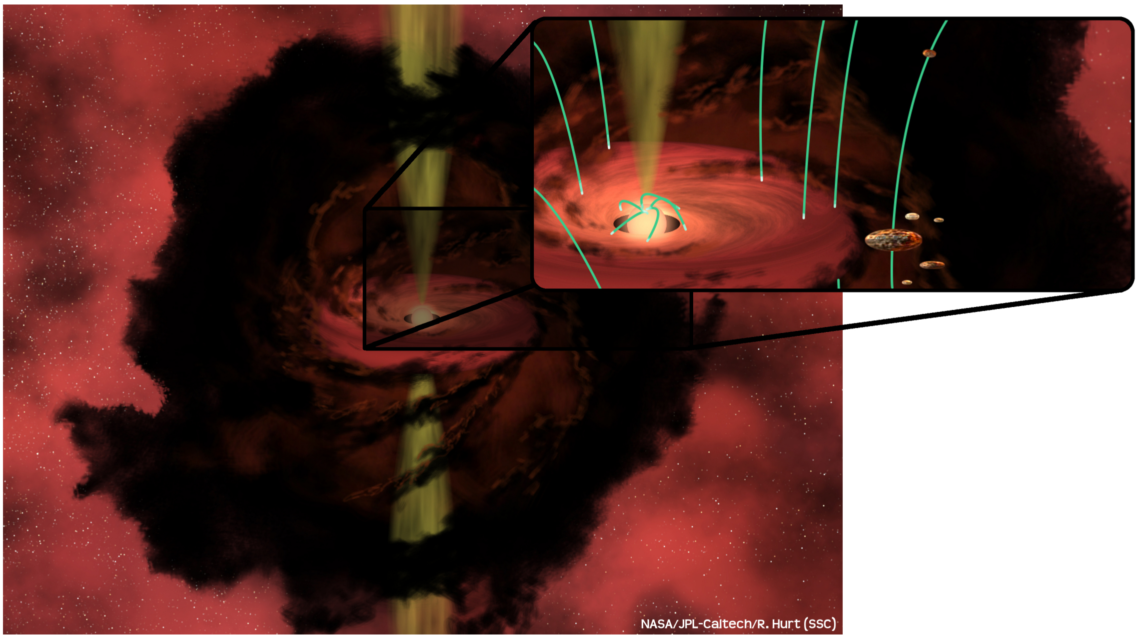

Fig. 2.5.: Magnetic field inside a Bok globule: This artistic impression shows an Bok globule with an young stellar object inside, transitioning from Class 0 to Class I (see Sect. 2.2). The dust grains contained within this globule are aligned by the magnetic field (green lines) that permeates the globule. These aligned, non-spherical dust grains are used to trace the magnetic field structure by polarimetric observations (see Sect. 2.3) (adapted from NASA/JPL-Caltech/R. Hurt, SCC).

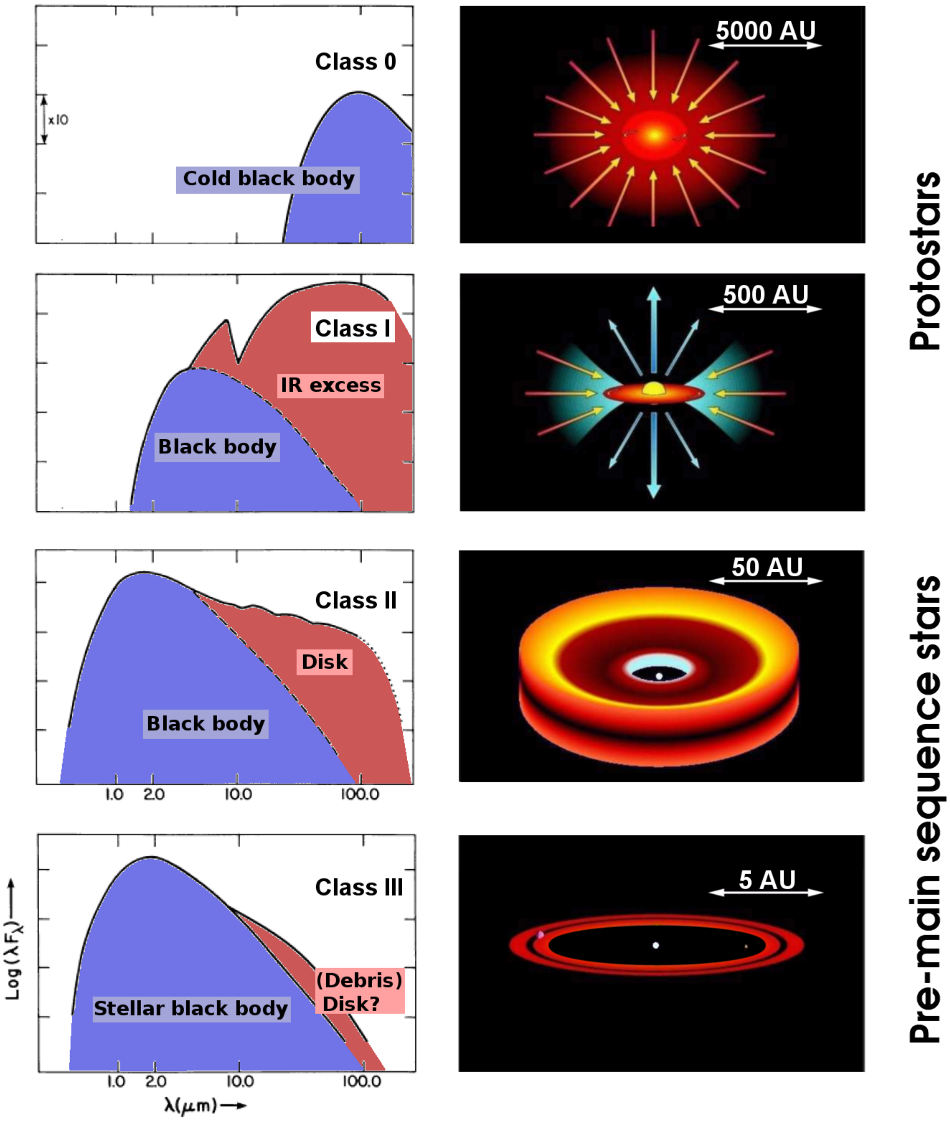

Fig. 2.6.: Empirical classification scheme for YSOs based on the slopes of their SEDs (left panels): Class 0 : young protostar deeply embedded in a cold, $20-30\,\mathrm{K}$, molecular cloud, peaking in the sub-mm wavelength range. Class I : evolved protostar with IR excess, emission from a warm envelope heated by the accretion luminosity, that peaks in the far-IR. Class II : Classical T Tauri star surrounded by a protoplanetary disk. The peak shifts to mid- and near-IR as a disk forms and depends on whether the disk is passive or active. Class III : Weak-line T Tauri star, possibly surrounded by a debris disk and planets (adapted from Gräfe (2013), *left*, and Isella (2006), *right*).

Class I objects are evolved protostars that have already accreted most of their final mass from the enveloping cloud and accumulate circumstellar material, a primordial disk. Due to this and to the bipolar outflows, the envelope has lost most of its mass and is heated by the accretion luminosity. The emission of the warm envelope peaks in the far-IR where it shows an IR excess additional to the stellar photosphere. There are hints that the primordial disks around Class I objects are still growing by accretion of mass from the envelope (Yen et al. 2014). Characteristically, Class I objects have steep SEDs from the far-IR to the near-IR with $0 < \alpha_{\mathrm{IR}} \lesssim 3$.

Class II objects are classical T Tauri stars (cTTS). From this stage on, the central star is no longer a protostar but a pre-main sequence star. A Class II object lost its envelope and accretes mass only from the surrounding protoplanetary disk. It becomes observable in the optical, for the first time, unless it is obscured by the disk. In the IR and sub-mm wavelength range, the SED is dominated by the protoplanetary disk and depends on whether the disk is passive (merely re-processing the radiation form the central star) or active (also kept hot by ongoing accretion). With continuing processing of the dust in the disk, the IR excess becomes less important. Typical spectral indices of Class II object are $-2 \lesssim \alpha_{\mathrm{IR}} \leq 0$.

The computational part of this thesis (see chapters 5, 6) is focused on this stage of star formation.

Class III objects are all weak-line T Tauri stars (wTTS) since they show only little or no H_{α} emission. Class III objects show barely any IR excess. Thus, they are not longer surrounded by a massive disk but possibly by a debris disk. The gas component in the disk disappeared almost completely. Due to grain growth mechanisms, larger bodies are created within the disk, potentially even planets, in addition to smaller grains that are created by collisions of larger bodies (e.g., D'Alessio et al. 2001; Meru et al. 2014). Such debris disks can still be found around main sequence stars (e.g., Meyer et al. 2007). The SED of Class III objects is clearly dominated by the stellar photosphere with characteristically spectral indices of $-3 < \alpha_{\mathrm{IR}} \lesssim -2$.

2.3. Polarization

Polarization is a basic property of electromagnetic waves. This property is described by the location of the electric field vector, $\vec{E}$, relatively to the yz-plane, which is perpendicular to the propagation direction of the wave, x. In general, its components E_{y} and E_{z} are phase-shifted. In the yz-plane, E_{y} and E_{z} draw an ellipse (see Fig. 2.7), the polarization ellipse (see Fig. 2.8). The polarization ellipse is the most general case, linear polarization and circular polarization are degenerate cases. The polarization ellipse is defined by its direction of rotation, by its inclination relative to a reference axis, γ with $0 \leq \gamma \leq \pi$, by its radiant intensity, $c^2 = a^2 + b^2$, and the angle between its half-axes, η with

$$\tan \eta = \frac{b}{a}, \qquad \eta \in \left[-\frac{\pi}{4}, \frac{\pi}{4}\right]. \tag{2.2}$$

The general case of an elliptically polarized wave is a superposition of both linearly and circularly polarized waves. For a perfectly circularly polarized wave, the half-axes of the polarization ellipse are equal, i.e., $a = b$ and $\eta = \pi/4$. In the case of a perfectly linearly polarized wave one half-axis disappears such that $\eta = 0$ and $b = 0$. Another way to describe polarization is by giving the Stokes parameters, I, Q, U, V, as described in the next section.

2.3.1. Stokes parameters

In general, astronomical observations deal with light intensities rather than with electric field components (E_y, E_z). For this reason, a commonly used way to quantify polarization is not giving the polarization ellipse but characteristic intensities, the Stokes parameters, I, Q, U, V (Stokes 1852). The definition of each parameter can be explained with an ideal intensity measurement, respectively, with an ideal observation like it is displayed in Fig. 2.9.

The first Stokes parameter, I, represents the total, or unpolarized, intensity. I can be observed either without polarization filter or as the sum of two polarization directions, which are perpendicular to each other. The other three Stokes parameters are differences of intensities observed with different polarization vectors, perpendicular to each other. Q and U characterize the linear polarization, while V represents circular polarization. For mathematical treatment, the Stokes parameters are combined into the Stokes vector, $\vec{S} = (I, Q, U, V)^\mathbf{T}$. The Stokes parameters can be defined by intensity measurements, parameters of the polarization ellipse, and by spherical coordinates of the Poincaré sphere (see Fig. 2.8, 2.10):

$$\begin{aligned}
I &= I_{0^\circ} + I_{90^\circ} &&= I\,, \\
Q &= I_{0^\circ} - I_{90^\circ} &&= I_\mathrm{P} \cos 2\eta \cos 2\gamma\,, \\
U &= I_{45^\circ} - I_{135^\circ} &&= I_\mathrm{P} \cos 2\eta \sin 2\gamma\,, \\
V &= I_\mathrm{R} - I_\mathrm{L} &&= I_\mathrm{P} \sin 2\eta\,.
\end{aligned} \tag{2.3}$$

The factor of two in front of γ is due to the fact that any polarization ellipse is indistinguishable from one rotated by 180°, while the factor of two in front of η indicates that an ellipse is indistinguishable from one with the semi-axis lengths swapped accompanied by a 90° rotation.

For purely monochromatic coherent radiation, Eq. (2.3) results in

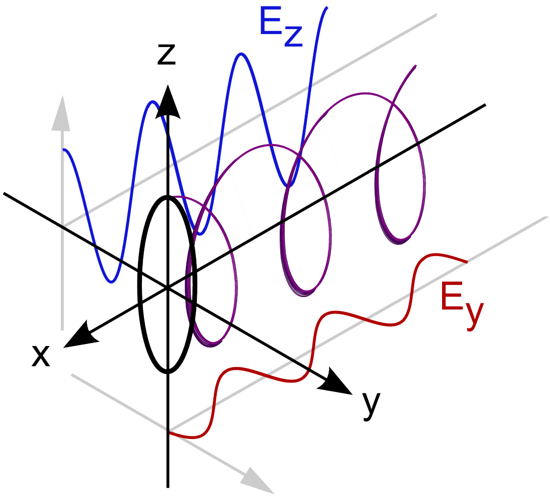

Fig. 2.7.: ELECTRIC FIELD VECTOR $\vec{E}$ (violet wave) is split into two components perpendicular to the direction of propagation, E_y (red wave) and E_z (blue wave). In the yz-plane, E_y and E_z draw the polarization ellipse (adapted from Bertrang 2010).

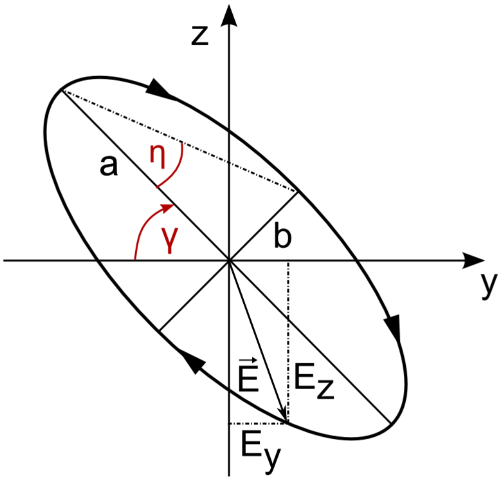

Fig. 2.8.: THE POLARIZATION ELLIPSE is defined by its direction of rotation, by its inclination relative to a reference axis, γ, by the relation of its half-axes, η, and its radiant intensity, $c^2 = a^2 + b^2$ (adapted from Bertrang 2010).

$$Q^2 + U^2 + V^2 = I^2. \tag{2.4}$$

In general, the (non-coherent) wave is not perfectly polarized, i.e.,

$$Q^2 + U^2 + V^2 \leq I^2. \tag{2.5}$$

However, by defining the total polarization intensity, I_P, Eq. (2.5) is expressed by

$$Q^2 + U^2 + V^2 = I_\mathrm{P}^2, \tag{2.6}$$

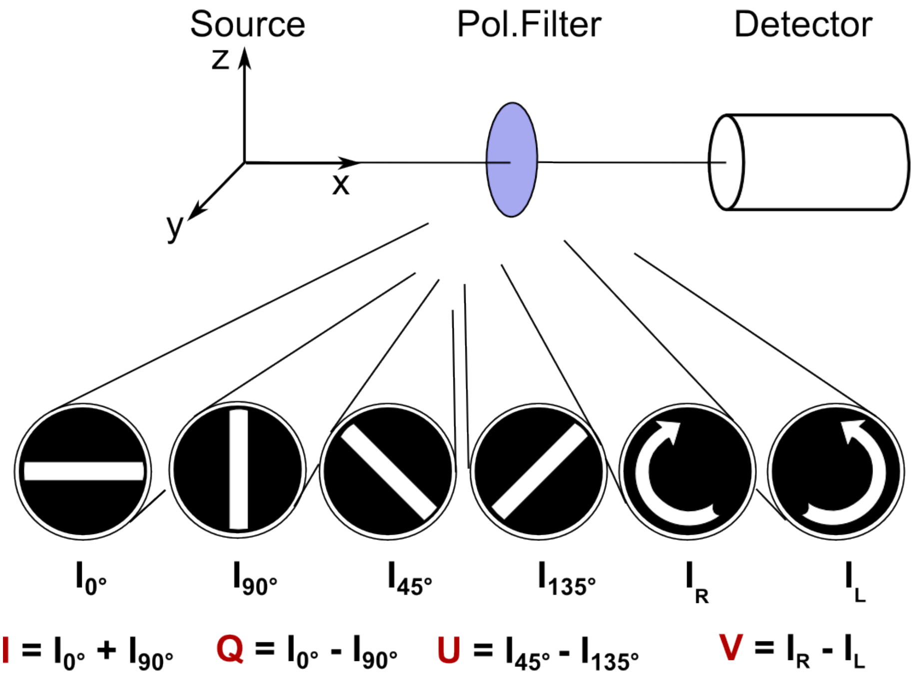

Fig. 2.9.: Ideal measurement of stokes parameters. The Stokes parameters, I, Q, U, V, can be determined by observations with different polarization filters (adapted from Fischer 1992).

where

$$\frac{I_{\mathrm{P}}}{I} = \frac{\sqrt{Q^2 + U^2 + V^2}}{I} = P\,, \qquad P \in [0,1]\,, \tag{2.7}$$

is the total degree of polarization, P. The polarization degree can be split into a linear polarization part, P_{L}, and a circular polarization part, P_{C}:

$$P_{\mathrm{L}} = \frac{\sqrt{Q^2 + U^2}}{I}\,, \qquad P_{\mathrm{C}} = \frac{V}{I}\,. \tag{2.8}$$

Unless declared otherwise, P refers to P_{L} in this thesis.

Notably, the Stokes parameters Q, U, V can be negative as well. The sign of V indicates the type of circular polarization. A positive sign of V means counterclockwise rotation, i.e., left-handed circular polarization, and, vice versa, a negative sign of V implies right-handed circular polarization. Likewise, the preferred orientation of linear polarization is given by the angle of polarization, γ (see Fig. 2.8, 2.10). The polarization angle is a quantity of linear polarization, thus, it is defined by the Stokes parameters Q, U:

$$\gamma = \frac{1}{2} \arctan\left(\frac{U}{Q}\right), \qquad \gamma \in [0, \pi]. \tag{2.9}$$

By convention, the polarization angle is measured from the y axis, positive in clockwise direction as shown in Fig. 2.8.

In the case of an unpolarized wave, the polarization ellipse turns into a circle ($Q = U = V = 0$), the polarization degree P drops to zero, and the Stokes vector becomes $\vec{S} = (1, 0, 0, 0)^{\mathbf{T}}$. A visualization of the polarization characterized by the Stokes vector is the Poincaré sphere (see Fig. 2.10). Assessing the Stokes parameters (Q, U, V) as a three-dimensional vector in Cartesian coordinates, then $(I_{\mathrm{P}}, 2\gamma, 2\eta)$ is the corresponding vector in spherical coordinates (see Eq. 2.3). The length of the polarization vector in the Poincaré sphere represents the polarized intensity, I_{P}, or the polarization degree, P, if the Poincaré sphere is normalized to the total intensity I (see Eq. 2.7). Any two antipodal points on the Poincaré sphere refer to orthogonal polarization states. The overlap between two arbitrary polarization states depends only on the distance between their locations along the Poincaré sphere. This characteristic, which can only be true when pure polarization states are mapped onto a sphere, is the motivation for the invention of the Poincaré sphere and the use of Stokes parameters which are thus plotted on (or beneath) it. The projection of the polarization vector onto the QU-plane gives the pure linear polarization state.

The observation of linear dust-induced polarization gives access to the magnetic field structure if the dust grains are aligned along the line-of-sight (LOS). How grain alignment works is explained in the next section.

2.4. Dust: Tracer of magnetic fields

Although the vast majority of mass in molecular clouds consists of gaseous molecular hydrogen, H_2, it is the dust that is optically thick, and thus dominates the optical properties of the cloud. The canonical average gas-to-dust ratio found in the literature for the interstellar medium (ISM) up to Class II objects is of the order of 100 (e.g., Lilley 1955; Lada et al. 2007; Hales et al. 2014). This section provides the introduction of the basic dust properties (Sect. 2.4.1), the polarization properties of grains (Sect. 2.4.2), and grain alignment mechanisms (Sect. 2.4.3) as needed to understand the role of dust in the context of this thesis.

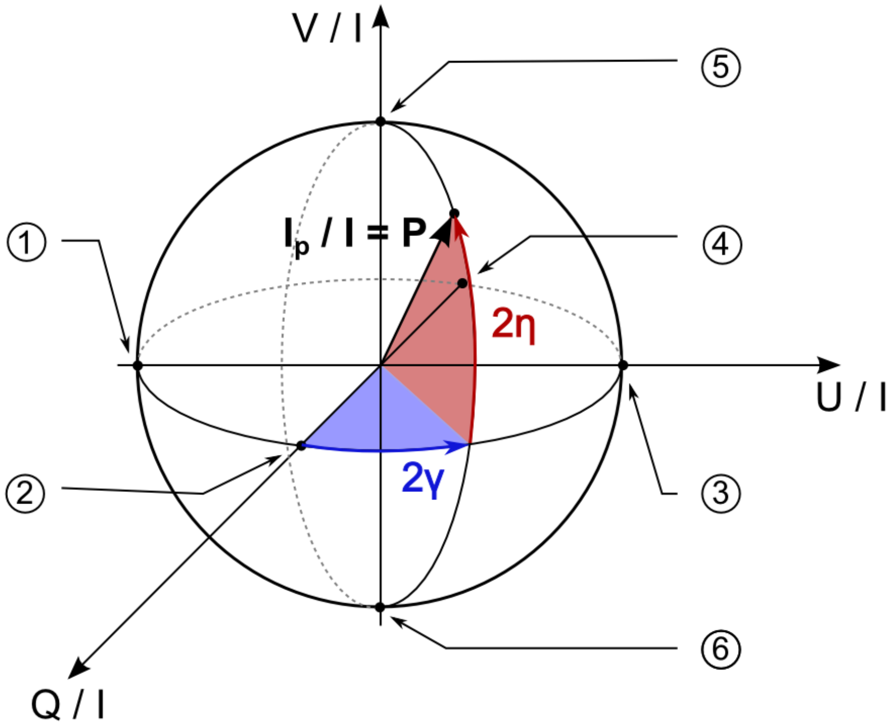

① Linearly polarized: $\gamma = 3\pi/4, \quad \begin{pmatrix} 1 \\ 0 \\ -1 \\ 0 \end{pmatrix}$

② Linearly polarized: $\gamma = 0, \quad \begin{pmatrix} 1 \\ 1 \\ 0 \\ 0 \end{pmatrix}$

③ Linearly polarized: $\gamma = \pi/4, \quad \begin{pmatrix} 1 \\ 0 \\ 1 \\ 0 \end{pmatrix}$

④ Linearly polarized: $\gamma = \pi/2, \quad \begin{pmatrix} 1 \\ -1 \\ 0 \\ 0 \end{pmatrix}$

⑤ Right-circularly polarized: $\begin{pmatrix} 1 \\ 0 \\ 0 \\ 1 \end{pmatrix}$

⑥ Left-circularly polarized: $\begin{pmatrix} 1 \\ 0 \\ 0 \\ -1 \end{pmatrix}$

Fig. 2.10.: The Poincaré sphere is the representation of the Stokes parameters, Q, U, V, in a spherical coordinate system. The degree of polarization, P, is defined as $P = I_{\mathrm{P}}/I = \sqrt{(Q/I)^2 + (U/I)^2 + (V/I)^2}$. The angles γ and η are the same as in the polarization ellipse (see Fig. 2.8; adapted from Bertrang 2010).

2.4.1. Properties of dust grains

Dust grains, as they grow from molecules to much larger bodies, are generally non-spherical. They mainly consist of a mixture of amorphous silicate and carbonaceous grains (e.g., Draine 2003). The dust grain size depends on the evolutionary stage of star formation, since the dust grains grow during the formation of the molecular cloud to the planetary system (e.g., Natta et al. 2007; see Sect. 2.6). In the interstellar medium (ISM) dust grains are typically of sub-μm size (e.g., Mathis et al. 1977). As they are accumulated to molecular clouds, grain growth starts and is characterized by the dynamical interaction between gas and dust, leading to collisions between solid particles and finally coagulation. The grains have typical sizes of $\lesssim 1\,\mathrm{mm}$ in protoplanetary disks (e.g., Natta et al. 2007; Ricci et al. 2010) and even grow to planets in the latest stages of star formation. The dust grain properties assumed for the computational part of this thesis are described in chapter 5.

2.4.2. Dust as polarizer

In order to understand the validity of dust-induced polarization measurements, it is necessary to understand the role of dust grains as polarizers. In general, there are three ways for dust to polarize light: dichroic absorption of background star light by aligned dust grains, thermal emission of aligned dust grains, and scattering of light (e.g., Weintraub et al. 2000; see Fig. 2.11).

Dichroic absorption of background star light requires both non-spherical dust grain shapes as well as optical depths that allow for transmission of background star light through the dust distribution to polarize light. As a light wave impinges upon a dust grain, the grain absorbs the wave components dependent on its shape in the plane of the electric field vector of the wave, $\vec{E}$. Thereby, the vector components are attenuated to different degrees. Assuming an oblate dust grain that is aligned perpendicular to the magnetic field line with respect to its longest grain axis and an impinging light wave as in Fig. 2.11. Then, the components of $\vec{E}$ along the longest grain axis are absorbed the most. As a result, the light wave is polarized perpendicular to the long grain axis, and respectively, the resulting light wave is polarized parallel to the magnetic field line.

Since this polarization mechanism is dependent on extinction, dichroic absorption of background star light by dust grains typically found in star-forming regions is observed in the optical and near-IR wavelength ranges.

Thermal dust emission by non-spherical dust grains is polarized intrinsically. Due to the non-spherical shape, the light wave emitted by such a dust grain consists of unequal electric field vector components. Thus, the emitted light wave of such a grain is intrinsically polarized. Assuming that the dust grain is aligned perpendicular to the magnetic field lines with respect to the longest grain axis, the emitted light wave is polarized parallel to the longest axis of the grain, i.e., the thermal dust emission is polarized perpendicular to the magnetic field line.

The wavelength of the dust emission is dependent on the grain temperature. For typical conditions found in star-forming regions, the polarized dust emission is observable in the (sub-)mm wavelength range.

Scattering of light itself works as a polarizer. Contrary to the described mechanisms above, scattering of light does not require a special dust grain shape to polarize light, even though the resulting polarization depends, i. a., on this characteristic. As a light wave impinges upon a dust grain, the wave stimulates oscillations of the dipoles within the grain which then act as Hertzian dipoles. The polarization state caused by scattering of light changes with, for example, dust grain shape, grain size, grain porosity, alignment of non-spherical grains by magnetic fields, grain location relative to radiation source and observer, and dust density distribution of the object (e.g., Wolf et al. 2002*b*; Kirchschlager & Wolf 2014; Marino et al. 2015).

Since the scattering of light depends on the wavelength relative to the dust grain size (e.g., Bohren & Huffman 1998), observations of scattered light are performed in the UV, the optical, and the near-IR wavelength ranges.

The polarizing properties of dust grains make these grains to tracer of magnetic fields, only if the alignment of dust grains to the magnetic field is understood. This is described in the next section.

2.4.3. Dust grain alignment

The knowledge of dust grain alignment is essential for our understanding of the observed dust-induced polarization, whether we are interested in the signal itself or the polarization signal is only foreground noise added to our observations (e.g., Lazarian & Finkbeiner 2003). The theoretical description of grain alignment had started shortly after the discovery of polarized stellar radiation in the middle of the 20th century (Hall 1949; Hiltner 1949), has long been controversial and has been reduced to a rule of thumb: *All grains are always aligned and the alignment happens with the longer grain axes perpendicular to the magnetic field.* However, a number of observations have indicated that this approach is far too simple: i) Dust grains smaller than a critical size are not or marginally aligned (Mathis 1986; Kim & Martin 1995); ii) Dust grains align dependent on their chemical composition (Mathis 1986); iii) A significant portion of dust grains deep within molecular clouds are not aligned

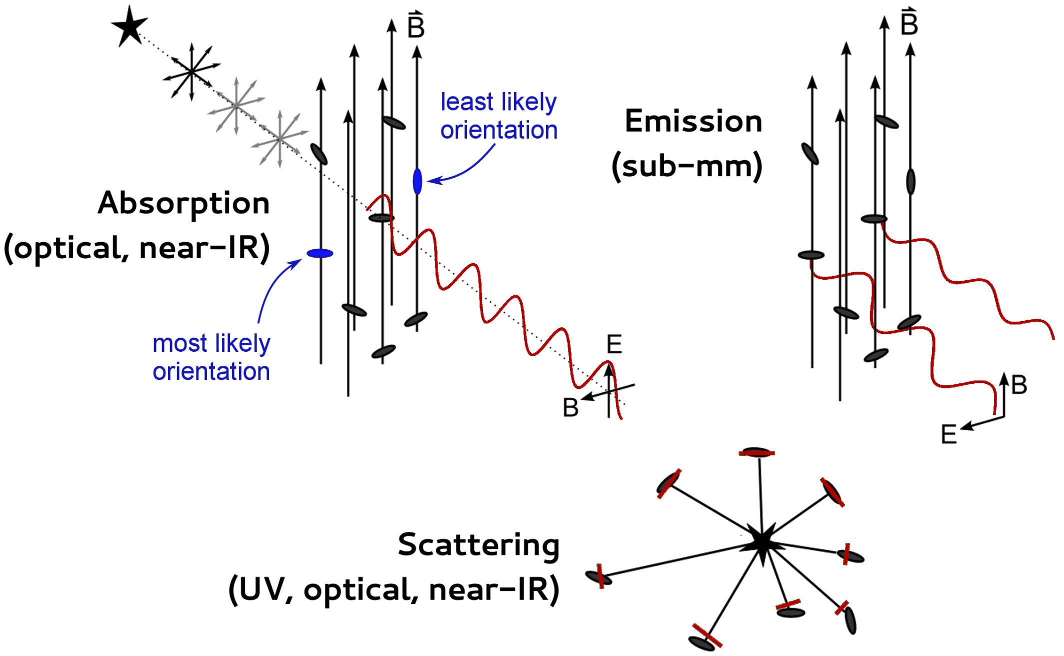

Fig. 2.11.: Dust grains are polarizers: Polarized light is generated by dust grains in three different ways: thermal emission of aligned dust grains (observable in the (sub-)mm range), dichroic absorption of background star light by aligned dust grains (observable in the optical and near-IR range), and scattering of light by dust grains (observable in the UV, the optical, and near-IR range). Usually the grains get aligned by magnetic fields with their long axis perpendicular to the field lines (adapted from Weintraub et al. 2000; see Sect. 2.4.2).

(e.g., Goodman et al. 1995; Lazarian et al. 1997); iv) Dust grains might align, rarely, with their longest axis parallel to the magnetic field line (Rao et al. 1998). However, grain alignment theory is still a matter of debate (e.g., Lazarian 2007; Lazarian et al. 2015). Yet, it is generally accepted that grains need to rotate supra-thermally to be aligned to the magnetic field. In this section, the most important grain alignment and de-alignment mechanisms are briefly summarized. The focus will be on the alignment mechanism which is currently discussed as the major contributor to grain alignment, on radiative torques.

Paramagnetic alignment (Davis & Greenstein 1951) was long considered as a "textbook example" of grain alignment. The alignment of thermally rotating paramagnetic dust grains has been elaborated in various studies over years (e.g., Jones & Spitzer 1967; Purcell 1979; Mathis 1986; Roberge & Lazarian 1999). The basic idea of paramagnetic alignment is the energy dissipation of the rotating paramagnetic dust grain due to its rotation in an external magnetic field. A paramagnetic grain has unpaired electrons which are aligned by an ambient magnetic field. Brownian grain rotation with the effective temperature equal to the mean of the grain and the gas temperatures is assumed (Jones & Spitzer 1967). The grain rotation annuls the alignment of its unpaired electrons with the ambient magnetic field. Thus, the unpaired electrons keep re-aligning to the magnetic field. As a result, the grain rotation suffers from energy loss. Static balance for the unpaired electrons is achieved as soon as the grain rotation no longer annuls its alignment to the ambient magnetic field, i.e., once the grain rotates with its longest axis perpendicular to the ambient magnetic field. This mechanism aligns grains with radii smaller than $0.1\,\mu$m very efficiently. However, paramagnetic alignment does not align dust grains larger than $0.1\,\mu$m (Lazarian et al. 2015), thus it cannot be the major alignment mechanism.

Mechanical alignment, established by Gold (1952*a*,*b*), explains the alignment of dust grains by supersonic flows. A non-spherical grain in a particle stream experiences inelastic collisions. During this process, angular momentum perpendicular to both the longest grain axis and the direction of the flow is transferred from the streaming particles to the dust grain. In turn, the sum of these angular momenta is perpendicular to the direction of the flow. A grain is aligned only if all particles are coming from the same direction, relative to the grain. This can be accomplished only in supersonic flows. The mechanical alignment mechanism was extended by later work (e.g., Lazarian 1995; Efroimsky 2002). Yet, sufficiently strong flows do not dominate the physics in space, thus mechanical alignment by supersonic flows is only of limited importance. Lazarian & Hoang (2007*b*) show that helical grains in subsonic flows tend to align with long axes perpendicular to magnetic fields similar to radiative torques. However, Lazarian et al. (2015) state that irregular grains may not show well-defined helicity in the process of grain interaction with gaseous flows and that limits the applicability of the subsonic mechanical alignment process, in general.

Radiative torques (RATs) as grain alignment mechanism has been discovered by Dolginov & Mytrophanov (1976). They have dealt with a dust grain of irregular shape that has different cross sections for left-handed and right-handed polarized radiation. Dolginov and Mytrophanov have recognized that such a grain spins up if it is radiated by unpolarized light. However, they have not been able to describe the mechanism quantitatively. Only when RATs had been implemented into the discrete dipole approximation code (DDSCAT; Draine & Flatau 1994), empirical studies have become possible and have revealed the significance of this alignment mechanism (e.g., Draine 1996; Draine & Weingartner 1996, 1997; Weingartner & Draine 2003). Abbas et al. (2004) have confirmed the spin up of grains by RATs experimentally under laboratory conditions. The effect of RATs is twofold. On the one hand, RATs can spin up dust grains, on the other hand, they can drive

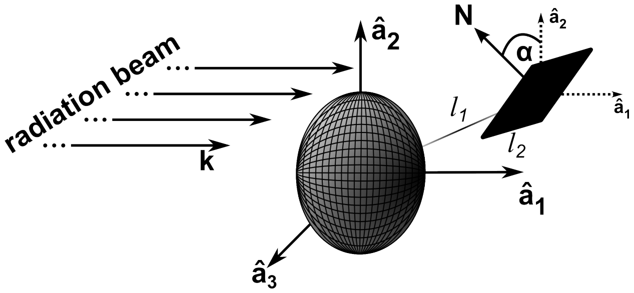

Fig. 2.12.: A HELICAL GRAIN like this is assumed in AMO (Lazarian & Hoang 2007*a*) to analytically compute radiative torques induced by radiation beam **k**: a perfectly reflecting oblate spheroid connected with a weightless mirror by a rod l_1. $\hat{a}_1$ is the symmetry axis of the grain, $\hat{a}_2$, $\hat{a}_3$ are two principal axes perpendicular to $\hat{a}_1$. $\hat{a}_1\hat{a}_2\hat{a}_3$ defines a reference system fixed to the grain. l_2 ($\ll l_1$) is the length and N is the normal vector of the mirror. N lies in the plane $\hat{a}_1\hat{a}_2$ and makes an angle α with $\hat{a}_2$. To change this left-handed helical grain into a right-handed grain, the mirror must be turned by 90° (adapted from Lazarian & Hoang 2007*a*).

the alignment of the dust grain. Although, Dolginov & Mytrophanov (1976) had assumed that RATs spin up the dust grain which will then align paramagnetically, Lazarian & Hoang (2007*a*) have identified the helicity of the grain as the feature that drives grain alignment by RATs. The challenge of a theoretical description of RATs is the absence of an analytical theory of irregular grain scattering. Therefore, Lazarian & Hoang (2007*a*) have assumed a helical grain as a composite of an oblate spheroid and a mirror attached by a weightless rod (see Fig. 2.12). This model, called AMO (Analytical MOdel) represents grain helicity in terms of its interaction with the radiation field. AMO is based on a perfectly reflecting oblate spheroid with an axis of maximum moment of inertia $\hat{a}_1$, and minor axes $\hat{a}_2$ and $\hat{a}_3$. A weightless mirror connected to the spheroid by a rod of length l_1 is used to obtain the scattering properties of a helical grain. The orientation of the mirror is determined by its normal vector N, which is assumed to be fixed in the plane $\hat{a}_1\hat{a}_2$ and makes an angle α with $\hat{a}_2$. While the grain is rotating, α is constant. The mirror size l_2 is supposed to be much smaller than its distance to the spheroid l_1. The physics behind AMO can be described as follows. When incident photons are reflected by the mirror or the spheroid, they transfer parts of their momenta to the grain. This results in an instantaneous radiative torque. After one rotation period around $\hat{a}_1$, the radiative torques due to scattering by the spheroid are canceled out, because of their symmetry. However, the radiative torques due to scattering by the mirror do have a net effect on the grain. Lazarian & Hoang (2007*a*) showed that this simple model of a helical grain is able to reproduce the basic properties of RATs as derived from numerical simulations with DDSCAT. AMO represents left-handed and right-handed grain models due to a change of the angle at which the mirror is attached to the grain. Actual irregular grains are supposed to vary in handedness. With AMO, findings of earlier numerical studies, e.g. of the fundamental study of Draine & Weingartner (1996, 1997), that had shown substantial differences in RATs on different grains, can be explained as a result of helical grains of different handedness. Anyway, the variety of properties of irregular grains is multifarious and cannot be reproduced by a simple toy model like AMO. Moreover, AMO does not account for the much more complex scattering process of light induced by an irregular grain. Nevertheless, AMO is currently the most evolved approach to turn RATs into a predictive theory.

De-aligning processes. For a profound understanding of dust grain alignment, it is important to consider de-aligning processes as well. In fact, processes that align dust grains to the magnetic field can be likewise the source of de-alignment. To give an example: Additional to the grain alignment mechanisms described above there exists internal relaxation. Internal relaxation minimizes the kinetic energy for a given angular momentum. As a result, the dust grain rotates around its axis of maximal angular momentum. The major components of the internal relaxation are the relaxations associated with the nuclear momenta of the grain. These are coupled to the vibrational and rotational degrees of motion of the grain. As a consequence, thermal fluctuations within the grain prohibit a perfect alignment of the grain to the angular momentum. In addition, thermal fluctuations cause fast flip overs and “thermal trapping” of sufficiently small grains. Thereby, the grain fails to gain enough rotational energy for supra-thermal rotation. The only alignment mechanism that is not affected by de-aligning internal relaxation is mechanical alignment. Though, mechanical alignment itself is able to destroy already existing grain alignment. Dust grains located in the vicinity of an outflow that fulfills the requirements of mechanical alignment will be re-aligned mechanically inside the influence zone of the outflow, irrespectively of the foregoing cause of alignment.

These are the fundamentals for both parts of this thesis. The following is dedicated to observations of low-mass star-forming regions in part I (chapter 3, 4) and simulations of protoplanetary disks in part II (chapter 5, 6). This work is summarized and concluded in chapter 7.

Part I.

Magnetic Fields In Star-Forming Regions – Observations

3. Observational basics

In astronomy, radiation is the main access to study the physical conditions of the object of interest. Depending on the research topic, the observations are focussed on certain wavelength regimes. The observations performed for this thesis (see chapter 4) have been obtained from different earthbound telescopes in different wavelength ranges, from the optical to the sub-millimeter (sub-mm) range. This chapter is the basis of this part of this thesis and presents the observational basics and notations (see Sect. 3.1), as well as the post-processing steps that are necessary to analyze the observed data (see Sect. 3.2).

3.1. Polarimetry

Polarimetry is the observational technique that is used to observe polarized light. In this section, the basics and common notations of polarimetry are covered in Sect. 3.1.1, and the technical details of polarimetry in the optical, near-IR, and sub-mm range are described in Sect. 3.1.2.

3.1.1. Basics and notations

At first glance, polarimetry is quite similar to standard intensity observations (classical imaging): Light enters the telescope, is reflected and directed to the instrument where it is caught by the detector and can be measured as an intensity. However, polarimetry differs from classical imaging mainly due to the additional use of a polarization filter (e.g., a Wollaston prism or half-wave plate; see Fig. 2.9). The technical background for polarimetry is given in Sect. 3.1.2, the applied steps of data reduction and analysis are given in Sect. 3.2, and the main effects that influence intensity measurements in general as well as notations with importance to these observations are described in the following paragraphs.

Diffraction. The observation of two sources as individuals is specified by the diffraction limit of a telescope. Considering only a light beam of a point source that enters the telescope while neglecting the atmosphere of Earth, the image of this point source on the detector of the telescope is not a point. The light is diffracted by the aperture of the telescope and takes shape of the diffraction pattern (point spread function, PSF). The PSF is an Airy disks in the case of an ideal, circular aperture. Assuming an observation of two point sources, A and B. To observe two individuals, the intensity maximum of B should be located at least in the first minimum of the Airy disk of A. This results in the minimal angular resolution of a telescope, the diffraction limit, $\delta \approx 1.22\,\lambda/D$, where D is the diameter of the aperture.

Seeing. The atmosphere of Earth varies not only in optical depth for different wavelength ranges. It varies also in its density structure because of turbulences in the atmosphere on scales of 10^{-2} s, for a good astronomical site. The diffraction of light passing through the varying atmosphere is described as seeing. The light of a point source is diffracted differently strong when it passes through differently dense regions of the atmosphere. As described above, without an atmosphere, a point source would appear on a detector of a telescope with an apparent size, as an Airy disk. However, due to the turbulences in the atmosphere, the Airy disk flares. The diameter of the flared Airy disks, or seeing disks, most often defined as the full width at half maximum (FWHM), is the seeing. A typical seeing for a good astronomical site is about $1\farcs$ in the optical range. Using modern techniques like adaptive optics, the seeing can be extenuated.

Noise. As for all kinds of measurements, the noise level determines the significance of an detection of an astronomical signal. This significance is expressed in the signal-to-noise ratio (SNR). It is generally assumed that no significant detection corresponds to a SNR < 3, whereas a definitive detection corresponds to a SNR > 5. However, due to the weak signal in most cases of polarimetry, SNR > 2 are usually also taken into account, with correct treatment of the resulting uncertainties. The sources of noise in the observations in this work are described in Sect. 3.2.

Airmass is the optical path length through the atmosphere of Earth. As light passes through the atmosphere, it is attenuated by scattering and extinction. The longer the path length, the greater the attenuation of the light. For small to moderate zenith angles, $z \lesssim 75°$, a good approximation for the airmass is given by a homogeneous plane-parallel atmosphere where airmass $=$ $\sec z$. In general, it is recommendable to observe objects at airmasses $\lesssim 2$.

Standard stars are the calibrators of astronomical observations. In general, properties of standard stars are very accurately determined. In polarimetry, there are two kinds of standard stars: polarized and unpolarized standard stars. Unpolarized standard stars are stars with an negligible intrinsical polarization. By determining the measured polarization degree, the instrumentally induced degree of polarization can be derived. On the other hand, polarized standard stars are stars with a well established instrinsical polarization. Thus, polarized standard stars are used to determine the deviation in the polarization angle induced by the instrument.

3.1.2. Polarimetry in the optical, near-Infrared, and sub-millimeter range

As introduced in chapter 2.3, polarimetry is an observation technique that makes use of polarization filters to determine the state of polarization of the observed light coming from the target of interest. There are various ways to realize a polarization filter. The two most common types installed in astronomical instruments are the Wollaston prism and the half-wave plate (HWP). Five telescopes, operating in the optical, near-IR, and the sub-mm wavelength range, were used to perform the observations shown in chapter 4. Each of them makes use of one of these two types of polarization filters. This section addresses the technical setup of these polarimeters. Based on this, the data reduction and analysis is described in Sect. 3.2.

3.1.2.1. Polarimetry in the optical and sub-mm range with IFOSC/IGO, IMPOL/GIRT, and SCUPOL/JCMT

The polarimeters of the 2 m IUCAA Faint Object Spectrograph & Camera (IFOSC) at the IUCAA Girawali Observatory (IGO, India) and the Imaging Polarimeter (IMPOL) at the Gurushikhar Infrared Telescope (GIRT, India), both operating in the optical, as well as the polarimeter of the Submillimetre Common User Bolometer Array Polarimeter (SCUPOL) at the James Clerk Maxwell Telescope (JCMT, Hawaii) use a HWP as polarization filter. A HWP consists of a birefringent material (e.g., calcite) and shifts the phase between two perpendicularly polarized components of a light wave. This happens because birefringence is the optical property of a material with a refractive index that depends on the polarization state and the propagation direction of light. The ordinary part of a light wave, which is polarized perpendicular to the optical axis of the material, experiences the refractive index n_o. The extraordinary part of the light wave, which is polarized parallel to the optical axis of the material, experiences the refractive index n_e. Since the velocity of propagation of light through material is depending on the refractive index,

$$v_\mathrm{o} = \frac{c}{n_\mathrm{o}} \qquad \text{resp.,} \qquad v_\mathrm{e} = \frac{c}{n_\mathrm{e}}, \tag{3.1}$$

where c is the light speed, both polarization components of the light wave are shifted in phase by ξ,

$$\xi = \frac{2\pi\,\Delta n\, L}{\lambda_0}\,, \tag{3.2}$$

where $\Delta n = n_\mathrm{e} - n_\mathrm{o}$ quantifies the birefringence, L is the thickness of the crystal, and λ_0 is the vacuum wavelength of the light. In the case of a HWP, these parameters are chosen in a way that the phase shift between the two polarization components is $\xi = \pi$. Behind the HWP, the light passes a splitter that divides the two phase-shifted components and hits the detector (see Fig. 3.4 for a raw data frame obtained with IFOSC/IGO). Similar to the measurement with a Wollaston prism, one Stokes parameter is obtained with one exposure. To obtain the other Stokes parameter, Q, resp. U, the HWP is rotated by 45°.

The field of view for the polarimetry mode of IFOSC/IGO is about $4' \times 4'$.

3.1.2.2. Near-Infrared polarimetry with ISAAC/VLT and SOFI/NTT

The two near-IR instruments that have been used for the observational study conducted in the context of this thesis are nearly identical but mounted on different telescopes. While the Infrared Spectrometer And Array Camera (ISAAC) was mounted until December 2013 (now decommissioned) at ESO's 8 m Very Large Telescope (VLT; Paranal, Chile), the instrument Son OF ISAAC (SOFI) is mounted at the 3.58 m New Technology Telescope (NTT; La Silla, Chile). Both instruments use a Wollaston prism as polarization filter and separate the two beams with a polarimetric mask (see Fig. 3.1, 3.2). In each exposure, two orthogonal orientations of polarization can be obtained, the ordinary and the extraordinary ray (see Fig. 3.3). As a result, in a single image frame, each star is displayed twice. Thus, one Stokes parameter, either Q or U, can be derived from one frame. However, to determine the polarization state, both linear Stokes parameters are needed. So, another frame needs to be obtained which is rotated by 45° relative to the first frame. This means that the full polarization information state of a star is stored in four images of this star. Due to the rotation of the instrument, it can happen that a star is covered by the polarimetric mask in the rotated frame. To observe the complete FOV and by this, ensure that all stars within the FOV are observed under all necessary polarization filter orientations, a series of three frames with offsets perpendicular to the polarimetric mask fields for each rotator position must be acquired (see Fig. 3.1).

3.2. Data reduction, analysis, and calibration

All observed raw, unprocessed data include systematic errors that need to be removed before data analysis can be carried out. The raw data, the image, can be expressed as mathematical function:

$$\text{Image} = [(\text{Object} + \text{Sky}) \cdot \text{Flatfield}] + \text{Dark Current} + \text{Bad Pixels} + \text{Noise}. \quad (3.3)$$

Since the archival data used for the study in chapter 4 had been reduced by the original authors, this section is limited to the data reduction and analysis of the near-IR and optical observations performed in the context of this thesis. Data reduction pipelines for ISAAC/VLT, SOFI/NTT, and IFOSC/IGO had not been provided by the instrument operators or available pipelines had been insufficient for the needs of the polarization data. For that reason, the data reduction and analysis pipelines for these instruments have been developed in the context of this thesis. They are based on ESO manuals (for ISAAC/VLT and SOFI/NTT; Schmidtobreick and the IOT 2011; Mason et al. 2007; Wolf et al. 2002*a*) and on the basis of communications with experienced IFOSC/IGO users (H. S. Das and A. Chakraborty, Assam University) since no official user manual has been provided for IFOSC/IGO.

Due to the extent of the data set obtained with each instrument, automatized pipelines are expedient. Since each instrument differs to a greater or lesser degree from the other, three individual data reduction pipelines have been developed for this thesis. The general idea is the same for every single pipeline, however, the technical implementation is instrument dependent. All three pipelines, written in Python, are of modular design and make use of modules especially developed in the context of this thesis and of well established modules that are publicly available (for details, such as flow charts of the pipelines, see appendix A).

3.2.1. Detector Specifications

All three instruments use Charge-Coupled Devices (CCDs) as detectors. The structurally identical instruments SOFI/NTT and ISAAC/VLT are equipped with infrared (IR) arrays (Rockwell Hg:Cd:Te 1024 × 1024 Hawaii array) that show very low dark currents of $< 0.1\,\mathrm{e^-/s}$ (ISAAC/VLT; Moorwood et al. 1998), respectively

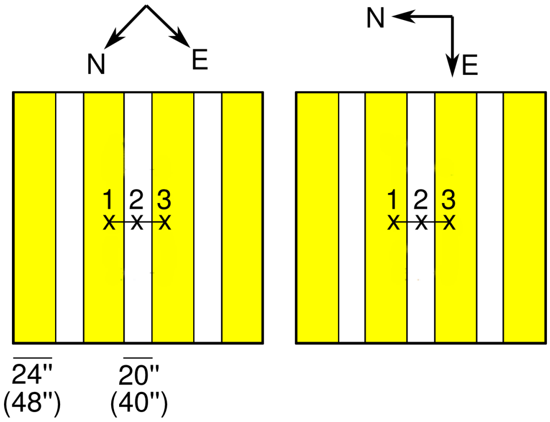

Fig. 3.1.: ACQUISITION TEMPLATE FOR POLARIMETRY WITH ISAAC/VLT (SOFI/NTT). The cross represents the position of a star. With this sequence, in total 6 exposures, the entire FOV is imaged: 3 offsets, each of 15″ (32″) in x-direction, and 2 orientations of the instrument (yellow fields are opaque; adapted from the ISAAC User manual: Schmidtobreick and the IOT 2011).

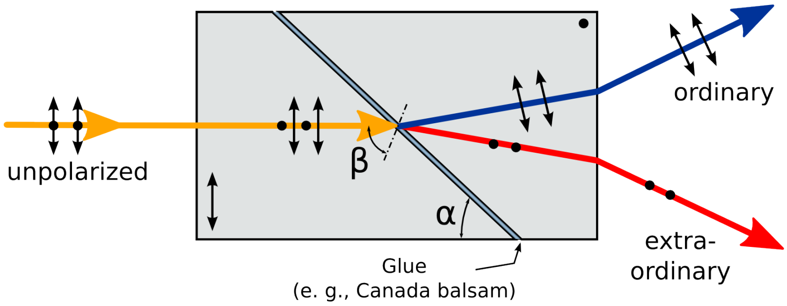

Fig. 3.2.: A Wollaston prism is an optical device that manipulates polarized light. It consists of two orthogonal prisms of a birefringent material (e.g., calcite). Both prisms are glued together by, e.g., Canada balsam, to create a new prism with two orthogonal optical axes. Incoming light diverges in two perpendicularly polarized, ordinary and extraordinary, light waves. The divergence angle is dependent on both the wedge angle, α, of the prism and the wavelength of the incoming light.

20 e^- / hour (SOFI/NTT; Saviane 2012). IR arrays are slightly different from optical CCDs such as the EEV (English Electric Valve Company) 2 K × 2 K (2048 × 2048 pixels) detector of IFOSC/IGO. A zero second exposure is not possible with the IR array. Therefore, all exposures without direct illuminated can be understood as dark frames. In this context, biases are integral and indistinguishable parts of dark frames.

3.2.2. Data reduction

The first steps of data reduction is the elimination of the bulk component, also known as overscan level (see Fig. 3.4), bias, bad pixels, i.e., pixels that show technical failures by being either constantly saturated (*hot pixels*) or do not react on impinging photons at all (*dead pixels*), as well as impacts of cosmic particles that create a small number of connected saturated pixels (*cosmics*; see Fig. 3.3). The final standard reduction steps are dark current reduction and flat fielding. In general, flat fielding requires a source of even illumination, typically a blank plane within the dome of the observatory that is illumination with a lamp (*dome flats*, performed with SOFI/NTT), or the twilight sky (*twilight/sky flats*, performed with ISAAC/VLT and IFOSC/IGO since dome flats are infeasible). For SOFI/NTT, a special flat fielding procedure is applied (for details, see appendix A).

3.2.3. Data analysis

Once all data frames are reduced, the pipelines start to analyze the polarimetric data. This is implemented in three basic steps, 1) the assignment of the complete

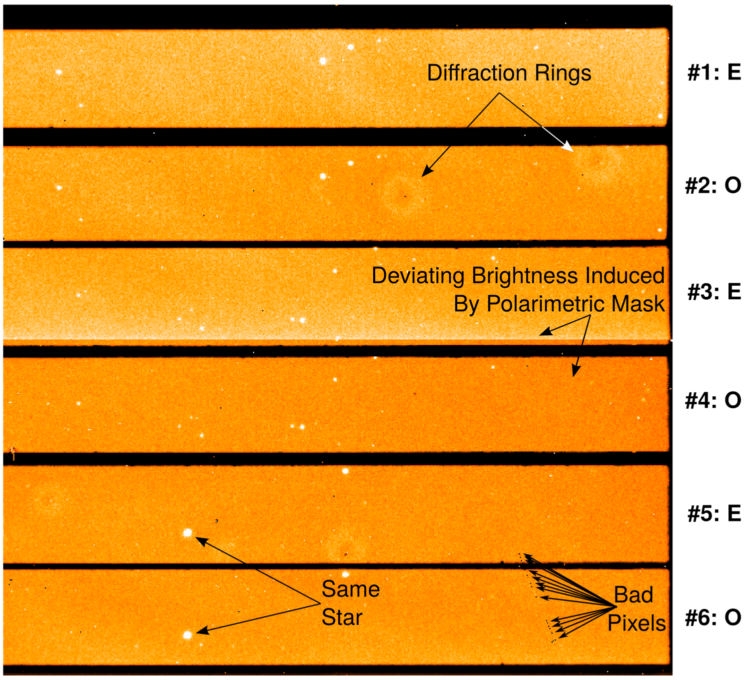

Fig. 3.3.: The SOFI/NTT polarimeter uses a Wollaston prism and separates the ordinary (O; component of the incoming light parallel to the axis of the analyzer) and extraordinary (E; component of the incoming light perpendicular to the analyzer axis) ray with a mask in the optical path. Thus, each star is imaged twice, in an O stripe and in an E stripe. This picture shows a raw data frame of a field of stars towards the Bok globule CB54.

data set to each observed star, 2) determination of the measured intensities by aperture photometry, and finally, 3) the computation of the Stokes parameters and the polarization parameters.

The four images of each star are distributed over six data frames. To assign the four corresponding images of a star to each other, they must be identified and correlated. An incorrect assignment would create a wrong polarization signal. The four corresponding images of each star were identified and correlated manually with the help of celestial maps for the data obtained with ISAAC/VLT and SOFI/NTT. Since IFOSC/IGO is not provided with a polarimetric mask in the optical path (see Fig. 3.4), the well-established code SourceExtractor (`SExtractor`; Bertin 2012) has been applied.

Once all corresponding images of the stars are correlated, aperture photometry is applied to all those stars where the full polarization information is measured, i.e., for which the Stokes parameters Q and U can be derived. In this way, the local background noise level is removed from the data which narrows the generation of

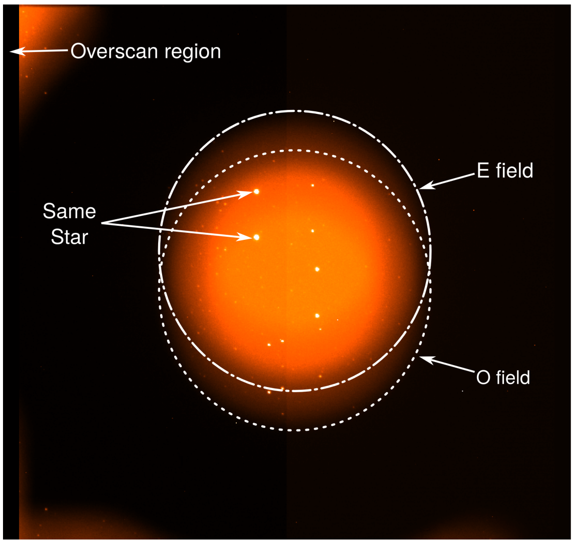

Fig. 3.4.: THE IFOSC/IGO POLARIMETER uses a HWP but does not separate the ordinary and extraordinary ray with a mask. Thus, each star is observed twice in this frame but often, o and e rays are overlapping. This is why aperture photometry is applied in order to minimize artificially induced errors due to flawed background subtraction. The overscan region can be found at the left side of this frame. This picture shows a raw data frame of a field of stars towards the Bok globule CB68.

artificial polarization to a negligible minimum (see appendix A for details).

The next step in the data analysis process is the computation of the Stokes parameters and, subsequently, of the polarization parameters from the background-subtracted intensity measurements. Since the state of the linear polarization reveals the magnetic field structure, the linear Stokes parameters, I, Q, U, must be computed from the data (see chapter 2.3):

$$\begin{aligned} I &= I_{0^\circ} + I_{90^\circ} = I_{45^\circ} + I_{135^\circ}, \\ Q &= I_{0^\circ} - I_{90^\circ}\,, \\ U &= I_{45^\circ} - I_{135^\circ}\,, \end{aligned} \tag{3.4}$$

where the orientation of the ordinary field (O) of the image is the orientation angle of the polarimeter and the extraordinary field (E) is shifted by 90° (see Fig. 3.3).

The accuracy of the measurement is increased due to oversampling by measuring the intensity for more than two orientations of the polarimeter (differing by 45°). If q and u are the normalized Stokes parameters,

$$\begin{aligned} q &= \frac{Q}{I}\,, \\ u &= \frac{U}{I}\,, \end{aligned} \tag{3.5}$$

and ϵ_0 is the arbitrary initial orientation of the polarimeter, then the oversampled Stokes parameters are (Wolf et al. 2002*a*)

$$\begin{aligned}
\tilde{q} &= \frac{I(\epsilon_0) - I(\epsilon_0 + 90°)}{I(\epsilon_0) + I(\epsilon_0 + 90°)}, \\
\tilde{u} &= \frac{I(\epsilon_0 + 45°) - I(\epsilon_0 + 135°)}{I(\epsilon_0 + 45°) + I(\epsilon_0 + 135°)}.
\end{aligned} \tag{3.6}$$

From this, the degree of linear polarization, P, and the angle of linear polarization, γ, are derived:

$$\begin{aligned}
P &= \sqrt{\tilde{q}^2 + \tilde{u}^2} \\
\gamma &= \frac{1}{2} \arctan\left(\frac{\tilde{u}}{\tilde{q}}\right) + \epsilon_0.
\end{aligned} \tag{3.7}$$

The standard deviations for the polarization degree and the polarization angle are given by (Wardle & Kronberg 1974; Wolf et al. 2002*a*):

$$\sigma_{\mathrm{P}} = \frac{\sqrt{(q\,\sigma_{\mathrm{q}})^2 + (u\,\sigma_{\mathrm{u}})^2}}{P} \tag{3.8}$$

and

$$\sigma_\gamma = \begin{cases} 29° \frac{\sigma_{\mathrm{P}}}{P} & : \quad P \gg \sigma_{\mathrm{P}} \\ 52° & : \quad P \approx 0 \end{cases} \tag{3.9}$$

where the value $\sigma_\gamma \approx 52°$ results from the uniform distribution of the angles of polarization within the interval $[0°, 180°]$ for the case of $P \approx 0$.

Finally, the polarization data is visualized in the common form of a polarization map where the state of polarization of each data point is given by a polarization vector (centered on the data point). A polarization vector does not have a preferential sign, its length represents the degree of polarization, and its orientation relative to the horizontal of the map represents the polarization angle. Usually, a map of the total intensity of the object is used as background for polarization maps. The polarization maps produced by these pipelines are presented in Fig. 4.4, 4.5, and 4.6.

3.2.4. Instrumental polarization

Every instrument or telescope may influence the polarization state of the incoming light through its instrumental polarization. Therefore, the instrumental polarization needs to be considered during the data reduction process. The assumption here is that the instrumental polarization is mainly created by a non-ideal transmission ratio of the Wollaston prism. The ideal transmission ratio would be a 50% : 50% ratio of the intensities of the ordinary (O) to the extraordinary (E) field (see Fig. 3.3). However, material characteristics and defects can lead to deviations from the ideal transmission ratio. To correct for this deviation, a correction factor, C_λ, is introduced (Wolf et al. 2002*a*):

$$\begin{aligned} i_{\mathrm{O},2} &= i_{\mathrm{O},1} \cdot C_\lambda \\ i_{\mathrm{E},2} &= i_{\mathrm{E},1} \end{aligned} \tag{3.10}$$

To determine the instrumental polarization, C_λ has to be adjusted in such a way that the measured polarization of the unpolarized standard star is minimal. The value of C_λ that meets this requirement is the correction factor of the data images. The residual polarization of the unpolarized standard star gives an estimate for the instrumental polarization.

For the observations of the Bok globule CB54 and the unpolarized standard stars HD64299 and WD0310-688 (see Tab. 3.1), performed with SOFI/NTT in the J band that are presented in chapter 4, a correction factor of

$$C_{\mathrm{Js}} = 0.898 \pm 0.018 \tag{3.11}$$

was determined (see Fig. 3.5).

The ISAAC/VLT observations of this study were performed in service mode between March 27 and May 27, 2012. Each night, two observations of unpolarized standard stars, GJ1178 and EGGR118 (see Tab. 3.1), were performed. When its right ascension meant that GJ1178 was no longer observable, two observations of EGGR118 were made in the same night. Thus, observations of EGGR118 exist for the complete observing period of two months, always performed with the very same procedure.

An instrumental polarization is determined that shows a strong dependence on the airmass of the object, respectively the elevation angle of the telescope. In Fig. 3.6 the correction factor, C_{Js}, is plotted over the airmass of EGGR118. The correction factor varies about 10 % between the beginning of the observations (airmass ≈ 1) and the end of the observations (airmass ≈ 2.4). Since the Stokes parameters, Q and U, are linearly dependent on C_λ, the instrumental polarization itself changes significantly with the airmass of the observed object. For EGGR118, a deviation of $\Delta P \approx 1.4$ % is found.

To correct for this effect, a second-degree polynomial is fitted to the values of C_{Js} that were determined for the different airmasses EGGR118 was observed at (see Fig. 3.6). Then, the polynomial fit is used to determine the corresponding correction factors for the airmass intervals of the Bok globule observations of each field (see Fig. 3.7).

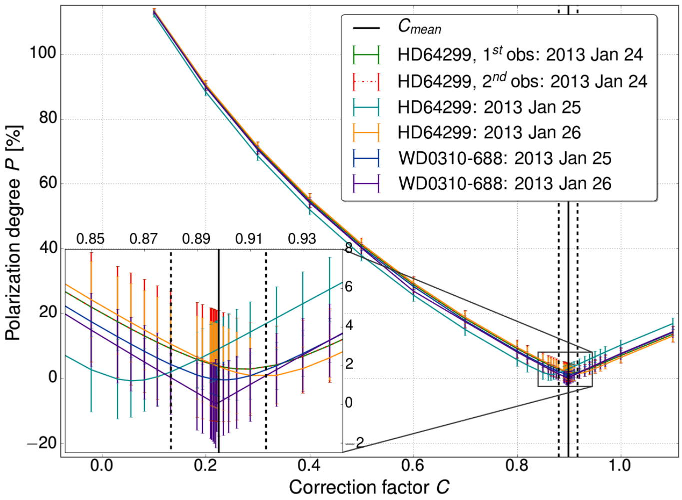

Fig. 3.5.: Correction factor for transmission ratio of the non-ideal Wollaston prism of SOFI/NTT. By determining the minimum polarization degree of the unpolarized standard stars (for this, the pipeline has to be applied to the standard star data), the correction factor $C_{\mathrm{Js}} = 0.898 \pm 0.018$ (black line, errors in dashed lines) is validated as the mean of the individually determined correction factors.

The elevation angle dependency of the instrumental polarization clearly shows the invalidity of the assumption that the non-ideal Wollaston prism is the only source of the instrumental polarization that has to be considered. Since ISAAC/VLT does not contain any components that move after the basic setup of the instrument is completed, this dependency indicates significant influence by either the telescope itself or the atmosphere. An additional source of the instrumental polarization can be the deformation of the mirrors at different elevation angles, causing artificial polarization as the light beam is reflected.

3.2.5. Data calibration

In the course of the multi-wavelength polarimetry study, observations have been performed with ISAAC/VLT at orientations of the Wollaston prism of $0°, 45°$. During the SOFI/NTT and IFOSC/IGO observations, observations have been performed respectively with the Wollaston prism and the half-plate at four different orientations of $0°, 22.5°, 45°, 67.5°$. Unpolarized and polarized standard stars have been observed to determine the instrumental polarization. Tab. 3.1 summarizes the general information for these stars. The correction technique that has been applied to correct for instrumental polarization effects has proved successful as the observational results of the polarized standard star of the SOFI/NTT observations after bias correction correspond well to the literature values (see Tab. 3.1, 3.2).

Table 3.1.: Polarization standard stars (literature values).

Instrument	Object	α_{2000} (hh:mm:ss.ss)	δ_{2000} (dd:mm:ss.ss)	Type	P (%)	γ (°)	Filter	Ref.
ISAAC/VLT	EGGR118	16:17:55.26	-15:35:51.93	unpolarized	< 1.79		J	1
	GJ1178	13:47:24.36	+10:21:37.90	unpolarized	< 1.08		J	1
SOFI/NTT	CMa R1 No.24	07:04:47.36	-10:56:17.44	polarized	2.1 ± 0.05	86 ± 1	J	2
	HD64299	07:52:25.51	-23:17:46.78	unpolarized	0.151 ± 0.032		B	3
	WD0310-688	03:10:31.02	-68:36:03.39	unpolarized	0.051 ± 0.09		V	4
IFOSC/IGO	HD251204	06:05:05.67	+23:23:38.54	polarized	4.04 ± 0.066	147	V	3
	GD319	12:50:05.00	+55:06:00.00	unpolarized	0.045 ± 0.047		B	3
	HD65583	08:00:32.12	+29:12:44.40	unpolarized	0.013 ± 0.02	144.7 ± 30	B	5

References. (1) Russell & Fender (2008); (2) Whittet et al. (1992); (3) Turnshek et al. (1990); (4) Fossati et al. (2007); (5) Clayton & Martin (1981).

Table 3.2.: Observational results for the polarized standard star of CB54.

Object	Obs. date	P (%)	σ_{P} (%)	γ (°)	σ_{γ} (°)
CMa R1	2013 Jan 24	2.34	0.94	85.52	56.0
No.24	2013 Jan 25	1.73	1.11	96.78	56.0
	2013 Jan 26	2.42	1.11	78.24	56.0

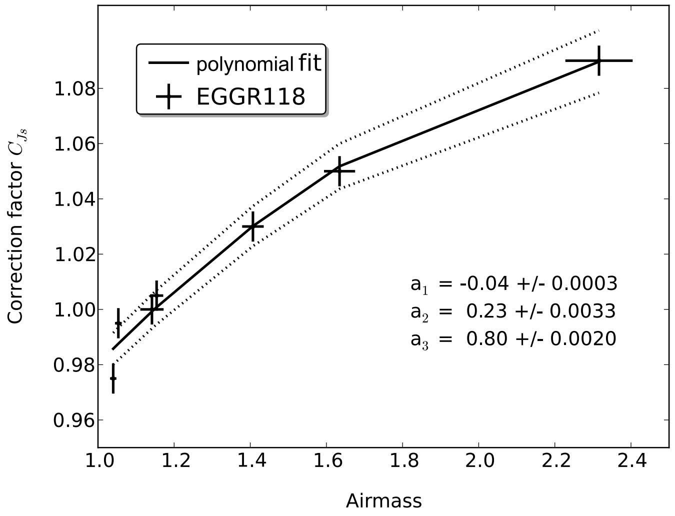

Fig. 3.6.: The plot shows the determined correction factors, C_{Js}, of EGGR118 over the corresponding airmasses and the fit to the data points (solid line, errors in dotted lines), a 2nd degree polynomial. The coefficients of the polynomial are given by the $\mathrm{a_i}$.

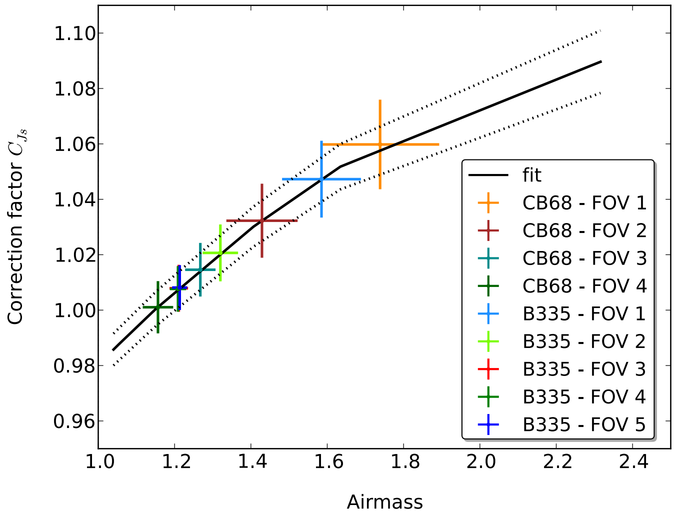

Fig. 3.7.: The corresponding correction factors, C_{Js}, of the airmass intervals of the globule observations are determined by using the polynomial fit (solid line, errors in dotted lines; see Fig. 3.6). The error bars in airmass direction give the airmass interval of the observation of each field. The error bars in C_{Js}-direction give the error of the estimated correction factor of each data point, including photometric and fitting errors.

4. Multi-wavelength polarization study of large-scale magnetic fields in Bok globules

In this chapter, the observational results of this thesis are presented. As described in the preceding chapters, the role of magnetic fields in the star formation process is a contentious matter of debate. In particular, no clear observational proof of a general influence by magnetic fields during the initial collapse of molecular clouds exists. The aim is to examine magnetic fields and their influence on a wide range of spatial scales in low-mass star-forming regions. Therefore, the large-scale magnetic field structure is traced on scales of $10^3 - 10^5$ AU in the local environment of Bok globules through optical and near-infrared polarimetry. These measurements are combined with existing sub-millimeter measurements that characterize the small-scale magnetic field structure on scales of $10^2 - 10^3$ AU.

For the first time, polarimetric observations in the optical and near-infrared wavelength range of the three Bok globules B335, CB68, and CB54, combined with archival observations in the sub-millimeter and the optical range are presented. A significant polarization signal ($P \gtrsim 2$ %, $P/\sigma_{\mathrm{P}} > 3$) is found in the optical and near-infrared for all three globules. Additionally, a connection between the structure on scales of $10^2 - 10^3$ AU and $10^3 - 10^4$ AU for both B335 and CB68 is detected. Furthermore, for CB54, ordered polarization vectors on scales of $\sim 10^5$ AU are traced. In the context of this study, a magnetic field orientation is ascertained that is aligned with the CO outflow in the case of CB54, but nearly perpendicular to the CO outflow for CB68. For B335, a change in the magnetic field oriented toward the outflow direction is found. This study reveals strongly aligned polarization vectors that indicate dominant magnetic fields on a wide range of spatial scales.

The content of this chapter has been published in the journal *Astronomy & Astrophysics* (Bertrang et al. 2014).

4.1. Introduction

As described in chapter 2, observations of the polarized radiation allow an assessment of the relative importance of uniform and tangled magnetic fields: A high level of polarization, uniform in direction, indicates a well-ordered field that is not significantly tangled on scales smaller than the beam size, i.e., a magnetic field that plays an important role in the evolution of the local density structure during the star formation.

A very good environment for studying the role of magnetic fields is given in low-mass star-forming regions, so-called Bok globules. These objects are less affected by large-scale turbulences and other nearby star-forming events.

Given the sensitivity of millimeter/sub-millimeter (sub-mm) telescopes that allow for polarimetric observations, the thermal emission of the dust grains, observable in the sub-mm, traces the densest, central part of a Bok globule. The less dense, outer parts are traced with polarized observations of background starlight that is dichroic absorbed and observable in the near-infrared (near-IR) / optical. Thus, multi-wavelength observations that combine sub-mm, near-IR, and optical wavelength ranges reveal the magnetic field geometry from the smallest to the largest scales of the Bok globule. So far, there have only been about two dozen sub-mm polarimetric observations of Bok globules, while only about half a dozen of these show ordered magnetic field structures (Matthews et al. 2009; Dotson et al. 2010). The majority of the observations of polarized sub-mm radiation show tangled field patterns, an indicator for negligible magnetic fields. Contrary to that, the near-IR and optical observations of Alves et al. (2011), Stephens et al. (2013), and Sen et al. (2000) revealed ordered field structures in the less dense, outer parts, indicating dominant magnetic fields in these parts of low-mass star-forming regions. Motivated by this, this polarization study of Bok globules was performed with two morphologically different globule types: B335 and CB68 are small globules with simple structures, whereas CB54 is a larger Bok globule with a more complex structure. In this chapter, polarimetric observations are presented, observed in the optical and near-IR of the three Bok globules B335, CB68, and CB54, combined with archival sub-mm and optical observations.

This study starts with a description of the sources and the selection criteria in Sect. 4.2. In Sect. 4.3 the polarization maps are analyzed, and Sect. 4.4 and 4.5 discuss the magnetic field and the correlation between the magnetic field structure and the CO outflows. In Sect. 4.6 the observability of the gap regions between the sub-mm and near-IR observations is discussed and the results of this study are summarized.

4.2. Description of the sources

The aim of this study is to observe the polarization structure and, by this, the magnetic field structure on a wide range of scales with as few external influences as possible, e.g., nearby star-forming activity or reflection nebulae. This restricts this study to isolated and compact Bok globules with available archival sub-mm polarization maps that show regular magnetic field structures. Additionally, the globules ought to have a high number of potential background stars in the particular wavelength range and to be observable from sites with access to optical or near-IR polarimeters. By applying these selection criteria to the legacy catalogs of the 350 μm polarimeter, Hertz, at the Caltech Submillimeter Observatory (CSO, Dotson et al. 2010) and the 850 μm polarimeter for SCUBA, SCUPOL, at the James Clerk Maxwell Telescope (JCMT, Matthews et al. 2009), it became evident that these criteria are satisfied only by the three Bok globules B335, CB68, and CB54.

B335 is a Bok globule at a distance of only ~ 100 pc (Olofsson & Olofsson 2009; see Fig. 4.1), and it accommodates one of the best-studied low-mass protostellar cores (e.g., Harvey et al. 2003; Evans et al. 2005). Its protostar drives a collimated bipolar outflow with a dynamical age of $\sim 3\times10^4$ yr (e.g., Chandler & Sargent 1993). The dense core in B335 is generally recognized as the best protostellar collapse candidate, and the emission from different molecular lines has been successfully modeled in terms of an inside-out collapse (Shu 1977) with an infall age of $\sim 10^5$ yr and a current protostar mass of $\sim 0.4\,\mathrm{M}_\odot$ (e.g., Choi et al. 1995). A total envelope mass of $\sim 4\,\mathrm{M}_\odot$ within a radius of 1.5×10^4 AU was derived from sub-mm observations by Wolf et al. (2003).

CB68 is a globule in a distance of ~ 160 pc (Launhardt & Henning 1997; see Fig. 4.2). It is remarkable for the very high percentage of polarization near 850 μm (Vallée et al. 2000). The small core of CB68 with a mass of $\sim 0.9\,\mathrm{M}_\odot$ and a diameter of 0.03 pc is just below the critical size scale of 0.05 pc, identified as the diameter where there is a break in star formation processes and below which there is a coherent core (Vallée et al. 2000). Roughly perpendicular to its bipolar CO outflow, there is an elongated structure seen in both dense gas and dense dust, indicating a pseudo-disk (Vallée et al. 2003). Sub-mm polarization data obtained with SCUBA/JCMT implies an hourglass-type magnetic field structure (Vallée & Fiege 2007).

CB54 is a large Bok globule, associated with the molecular cloud BWW 4 at a distance of ~ 1100 pc (Brand & Blitz 1993; see Fig. 4.3). The globule contains a massive dense core of $M_\mathrm{H} \sim 100\,\mathrm{M}_\odot$ that drives a bipolar molecular outflow (Launhardt & Henning 1997; Yun & Clemens 1994). At near-IR wavelengths, a small, deeply embedded young stellar cluster becomes visible (Wolf et al. 2004). CB54 shows a randomly oriented polarization pattern in the sub-mm (Henning et al. 2001; see Fig. 4.6 b). However, in the optical the polarization pattern appears more homogenous (Sen et al. 2000; see Fig. 4.6 c).

Object	Instrument	Filter	Date
B335	ISAAC/VLT	Js	2012 Mar-May
CB68	ISAAC/VLT	Js	2012 Mar-May
	IFOSC/IGO	R	2012 Mar 21-22
CB54	SOFI/NTT	Js	2013 Jan 24-26

Table 4.1.: Summary of the observations.

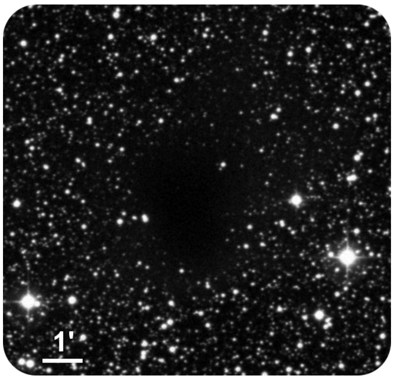

Fig. 4.1.: B335: Distance: 100 pc; Core dia.: 10^4 AU
Core mass: 4 $M_\odot$; CO outflow,

shown here in the optical (DSS). The dust is optically thick so that background star light cannot pass through the dens globule center. This region is traced in the sub-mm. The less dense, outer regions of the globule are optically thin, so that the background star light can pass through the globule. This region is traced in the optical and near-IR.

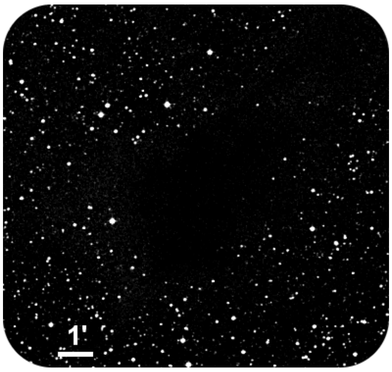

Fig. 4.2.: CB68: Distance: 160 pc
Core mass: 0.9 $M_\odot$
Core dia.: 6×10^3 AU
CO outflow

(Same as in Fig. 4.1)

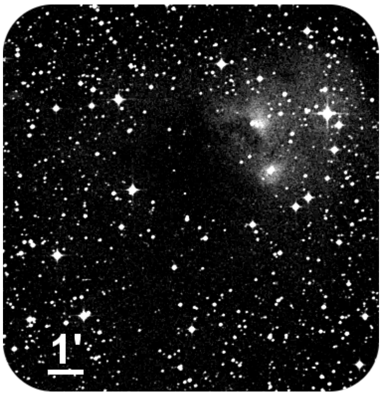

Fig. 4.3.: CB54: Distance: 1100 pc
Core mass: 100 $M_\odot$
CO outflow
Deeply embedded YSO cluster

(Same as in Fig. 4.1)

The observations were performed in the near-IR (Js-band, 1.24 μm) with ISAAC/VLT and SOFI/NTT as well as in the optical (R band, 0.6 μm) with IFOSC/IGO (see Tab. 4.1). In this context, five fields of B335 and CB68 with ISAAC/VLT, four fields of CB54 with SOFI/NTT, and four fields of CB68 with IFOSC/IGO have been observed.

4.3. Polarization maps

In this section, the polarization maps in the sub-mm, in the near-IR, and in the optical wavelength range of the three Bok globules B335, CB68, and CB54 are presented. For comparing the sub-mm maps with the near-IR and optical maps, it has to be taken into account that the polarization arises from two different physical processes: while thermal emission is observed in the sub-mm, dichroic absorption is observed in the near-IR and the optical range. Thus, the polarization of a dust grain observed in the sub-mm is oriented perpendicular to the polarization of the very same dust grain observed in the near-IR or optical range.

The sub-mm maps of the three objects of this study are each available in two versions, the originally published maps by Wolf et al. (2003), Vallée et al. (2003), and Henning et al. (2001), as well as re-reduced maps by Matthews et al. (2009). Matthews et al. (2009) reduced all polarimetric observations again that have been executed with SCUBA/JCMT and cover a huge variety of objects, from planets up to galaxies, in a single procedure. In doing so, Matthews et al. (2009) applied very strict criteria for the decision of including or omitting science data of an object and remark that data that was omitted by these generalized regulations may still be usable, and even part of publications, but would require too much individual assessment to meet the requirements of their systematic re-reduction. For this reason, this study uses the originally reduced and published sub-mm polarization maps in the discussion (see Fig. 4.4, 4.5, 4.6).

In the following, the polarization maps are discussed separately for each observed wavelength, as well as in comparison to the maps of the additional wavelength ranges.

4.3.1. Bok globules with simple morphology: B335 and CB68

The polarization maps of the Bok globules B335 and CB68 are shown in Fig. 4.4 and 4.5. Both globules disclose a significant polarization signal ($P \gtrsim 1\ \%$, $P/\sigma_{\mathrm{P}} > 3$) in their outer, less dense parts in the near-IR as well as in the optical for CB68 (see Fig. 4.7). The near-IR polarization vectors appear ordered very well in the case of CB68 ($\overline{\gamma} = 84.21° \pm 3.39°$, see Fig. 4.8) and largely well-ordered in the case of B335 ($\overline{\gamma} = 103.94° \pm 5.01°$, see Fig. 4.4, 4.8). According to ESO regulations, there are no observations of polarized standard stars for the near-IR data observed with ISAAC/VLT. Thus, no independent quantitative measure of the reliability of the observed polarization angles exists.

In both globules a clear spatial gap remains between the polarization vectors in the sub-mm and in the near-IR. The gap width in B335 amounts to about $70''(\approx 7 \times 10^3$ AU) and to about $100''(\approx 1.6 \times 10^4$ AU) in CB68. Launhardt et al. (2013) observed the hydrogen column densities, N_{H}, of CB68 and B335. In the region traced by SCUBA/JCMT, they determine $N_{\mathrm{H}} \gtrsim 10^{22}\mathrm{cm}^{-2}$ and in the region traced by ISAAC/VLT and SOFI/NTT they find $N_{\mathrm{H}} \lesssim 10^{21}\mathrm{cm}^{-2}$. This gives a benchmark for the feasibility to observe the morphology of the globules with the applied observing techniques and instrumentation and explains the gap.

In the case of B335, the orientation of the near-IR polarization vectors in the eastern and southern part of the globule matches to the orientation of the sub-mm polarization vectors very well. In the north-western part the polarization orientation shows local varieties in the sub-mm but not in the near-IR, even though the near-IR polarization pattern appears slightly unordered (see Fig. 4.4).

In the case of CB68, there are near-IR polarization vectors with $P/\sigma_{\mathrm{P}} > 3$ only in the western and in the south-eastern part. Vallée et al. (2003) observed a spiral polarization pattern in the sub-mm. One polarization 'spiral-arm' points toward the southeastern globule part and thus, matches well to the near-IR polarization vectors. For the polarization vectors in the western part, this is not the case. However, one has to keep in mind that there can also be an influence by that arm of the globule that stretches in the northwestern direction. The optical polarization vectors of CB68 in the most outer parts of the globule are rather unordered. However, the polarization vectors in the northern part (see Fig. 4.5 b.2) follow the smaller gas-dust branch that is perpendicular to the north-western arm of CB68. Additionally, in the southern part (see Fig. 4.5 b.3, upper half of the left field) the optical polarization vectors follow the small extension of the globule, too. There is a slight deviation of the orientation of the polarization vectors observed in the optical from those observed in the near-IR. The most straight forward explanation is that the different vectors trace the magnetic field in different regions of the globule.

4.3.2. Bok globule with more complex morphology: CB54

The polarization map of the Bok globule CB54 is shown in Fig. 4.6. The observations show a significant polarization signal ($P \gtrsim 2$ %, $P/\sigma_{\mathrm{P}} > 3$) in the near-IR across the entire globule (see Fig. 4.7). As in the case of the globules CB68 and B335, a clear spatial gap with a width of about $1'$ (corresponding to about 7×10^4 AU) between the polarization vectors measured in the sub-mm and in the near-IR in CB54 is found.

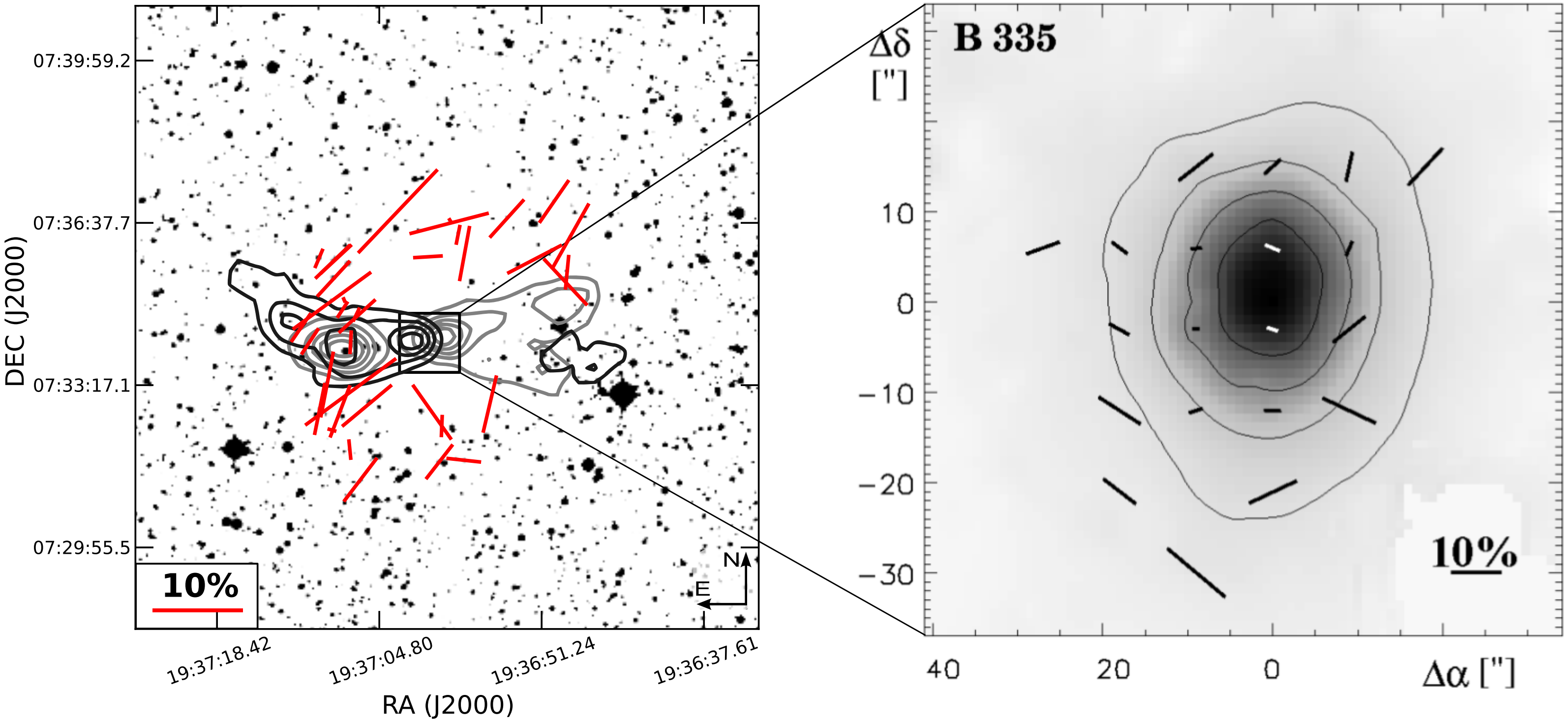

Fig. 4.4.: B335 - *Left:* DSS-map with overlaid near-IR polarization vectors observed with ISAAC/VLT. The length of the vectors shows the degree of polarization, and the direction gives the position angle. Only vectors with $P/\sigma_{\rm P} > 3$ are plotted. The contour lines represent the ^{12}CO$(2-1)$ OTF channel maps obtained with the HHT on Mount Graham. The black (gray) contour lines give the blue-shifted (red-shifted) eastern (western) outflow lobe. The contour levels are $\{1, 2, 3, 4, 5, 6, 8, 10, 12, 14, 16\} \times 0.5\ \mathrm{K} - T_A^*$ (from Stutz et al. 2008; beam size of 32″; reproduced by permission of the AAS). *Right:* Intensity map overlaid with polarization vectors obtained with SCUBA/JCMT in the sub-mm (from Wolf et al. 2003; reproduced by permission of the AAS).

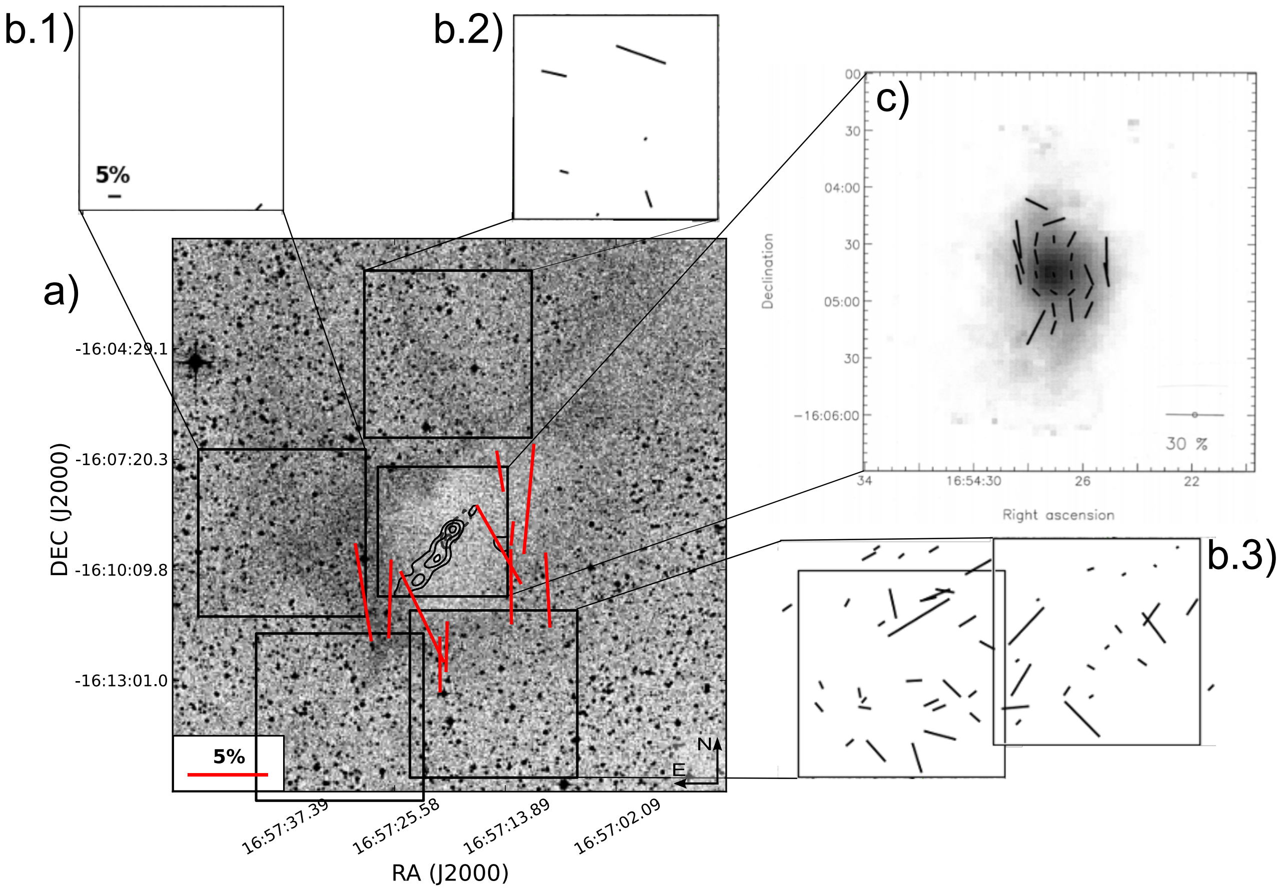

Fig. 4.5.: CB68 - *a)* DSS-map with overlaid near-IR polarization vectors observed with ISAAC/VLT. The length of the vectors shows the degree of polarization, and the direction gives the position angle. Only vectors with $P/\sigma_{\mathrm{P}} > 3$ are plotted. The contour lines represent the ^{12}CO$(3-2)$ spectral channel maps obtained with the JCMT. The black contour lines give the blue-shifted (south-eastern), the gray, dotted contour lines give the red-shifted (north-western) outflow lobe. Contour levels at $0.25, 0.50, 0.75, \ldots$ K (from Vallée et al. 2000; HPBW of $14''$; reproduced by permission of the AAS). *b.1-3)* Same as *a)* but with polarization vectors obtained with IFOSC/IGO in the optical. *c)* Intensity map overlaid with polarization vectors obtained with SCUBA/JCMT in the sub-mm (from Vallée et al. 2003; reproduced by permission of the AAS).

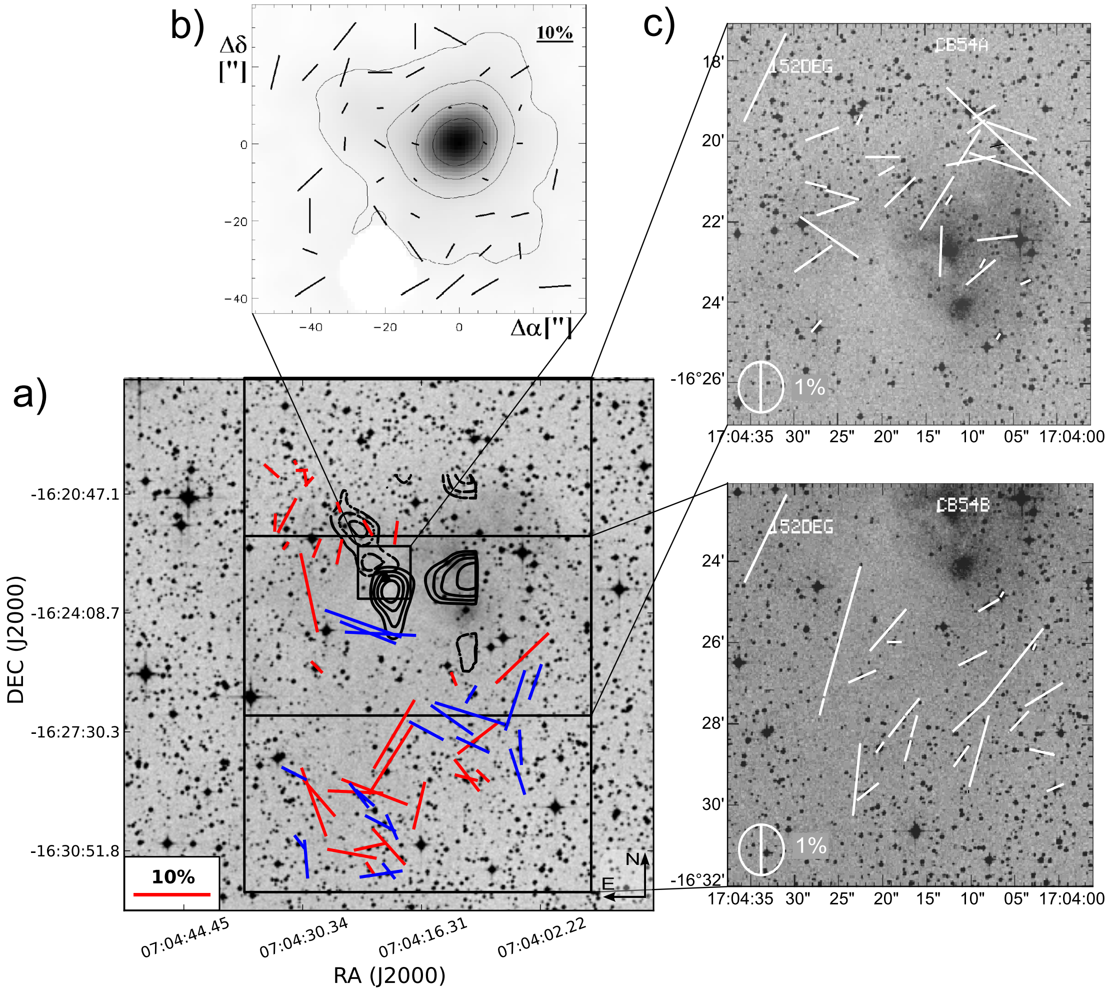

Fig. 4.6.: CB54 - *a)* DSS-map with overlaid near-IR polarization vectors observed with ISAAC/VLT. The length of the vectors shows the degree of polarization, and the direction gives the position angle. Only vectors with $P/\sigma_{\mathrm{P}} > 3$ are plotted. Blue vectors have a better error statistic than the red vectors, since they are based on more than one set of observations. The contour lines represent the ^{12}CO$(1-0)$ spectral channel maps obtained with the Five College Radio Astronomy Observatory. The solid contour lines give the blue-shifted (south-western), and the dotted contour lines give the red-shifted (north-eastern) outflow lobe. Contour levels are spaced at 0.3 K km s^{-1} intervals of 1.7 K km s^{-1} (blue), and 0.15 K km s^{-1} intervals of 0.45 K km s^{-1} (red), respectively (from Yun & Clemens 1994; beam size of 48″; reproduced by permission of the AAS). *b)* Intensity map overlaid with polarization vectors obtained with JCMT/SCUBA in the sub-mm (from Henning et al. 2001; reproduced by permission of the AAS) *c)* Intensity map overlaid with polarization vectors obtained with IMPOL/GIRT in the optical (from Sen et al. 2000).

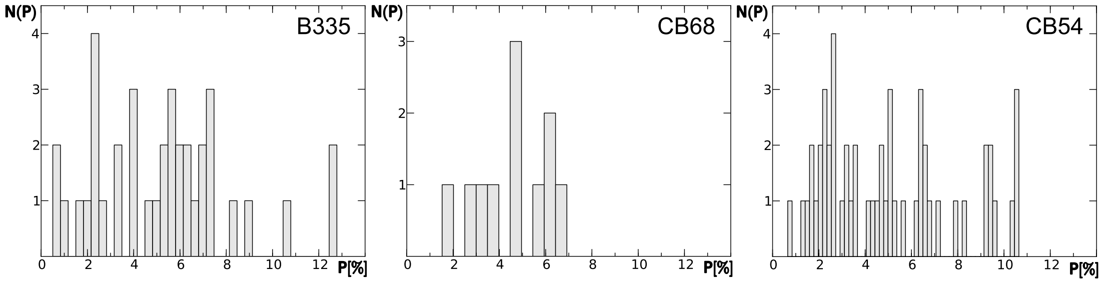

Fig. 4.7.: Histograms showing the distribution of the degree of polarization, P for $P/\sigma_{\mathrm{P}} > 3$, counts given by N(P), of B335, CB68, and CB54, observed in the near-IR.

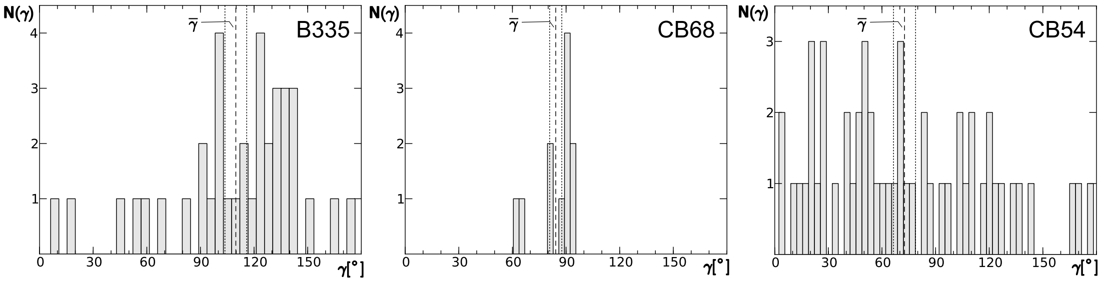

Fig. 4.8.: Histograms showing the distribution of the polarization angle, γ, counts given by N(γ), of B335, CB68, and CB54, observed in the near-IR. The dashed lines represent the mean polarization angles, $\overline{\gamma}$, with the corresponding 1σ levels (dotted lines).

Figure 4.6 displays polarization vectors that cover the globule on scales from $10^3 - 10^4$ AU up to 10^5 AU. Given the complex structure of this Bok globule, it is not necessarily expected to find uniformly ordered polarization vectors across such large scales. However, on smaller scales ($\sim 10^4$ AU), by a factor of $\gtrsim 2$ larger than the region traced by the sub-mm map, this near-IR observations and the optical observations by Sen et al. (2000) reveal ordered polarization vectors.

The southern field of the optical data (Fig. 4.6 c, lower field) overlaps with a part of the near-IR data. The optical polarization degree is about one order of magnitude stronger than that in the near-IR. This factor is significantly higher than the difference of about a factor of two which it is expected from dust properties obtained from Mie theory (Mie 1908). However, in terms of the orientation, the optical and near-IR vectors fit well to each other ($\Delta\gamma \lesssim 10°$).

The region around the sub-mm map is of particular interest. In the sub-mm, Wolf et al. (2003) found randomly oriented polarization vectors. However, the near-IR observations of this study reveal ordered polarization vectors on larger scales around the sub-mm map (see Fig. 4.6 a).

4.4. Magnetic fields

In the analysis it is assumed that the magnetic field is oriented perpendicular to the measured polarization vectors in the sub-mm and parallel oriented to the measured polarization vectors in the near-IR and in the optical. This widely applied concept is based on the finding that, independently of the alignment mechanism, charged interstellar dust grains would have a substantial magnetic moment leading to a rapid precession of the grain angular momentum around the magnetic field direction, implying a net alignment of the grains with the magnetic field (see, e.g., Draine & Weingartner 1997; Lazarian 2007). However, one has to keep in mind that polarimetry strongly suffers from projection effects along the line-of-sight (LOS). Thus, for a comprehensive understanding of the magnetic field structure additional 3D radiative transfer modeling is essential but beyond the scope of this study.

In general, a high degree of polarization is connected to a magnetic field that is strong enough to align enough dust grains along the LOS to prevent the annihilation of the polarized signal that is expected from randomly oriented grains along the LOS. In the observations of all three Bok globules, B335, CB68, and CB54, strongly ordered magnetic fields are found. Additionally, the observations show well-ordered polarization vectors on scales of $\lesssim 10^4$ AU for all three Bok globules. Thus these observations imply magnetic fields that are strongly ordered over large parts of the globules. And finally, in the case of B335 and CB68, the near-IR and optical observations of this study trace polarization patterns that fit to the polarization patterns observed in the sub-mm by Wolf et al. (2003) and Vallée et al. (2003), which implies strong and ordered magnetic fields on scales from $10^2 - 10^3$ AU to 10^4 AU.

Besides this analysis of the magnetic field, Chandrasekhar & Fermi (1953) give an estimate for the magnetic field strength in the plane-of-sky (POS; CF method):

$$\left|\vec{B}_{\text{pos}}\right| = \sqrt{\frac{4\pi}{3}\,\varrho_{\text{gas}}}\;\frac{v_{\text{turb}}}{\sigma_\gamma}, \tag{4.1}$$

where ϱ_{gas} is the gas density in units of g cm^{-3}, v_{turb} the rms turbulence velocity in units of cm s^{-1}, and σ_γ the standard deviation of the polarization position angles in radians. Here, it is assumed that the magnetic field is frozen in the cloud material. For a detailed discussion of this equation, see Crutcher (2012), and for an extension of the mean magnetic field strength, see Houde (2004).

For B335, the hydrogen number densities and the turbulence velocity from Frerking et al. (1987) are used, for details see Tab. 4.2. To account for helium and heavier elements, the total gas density ρ_{gas} is derived from

$$\rho_{\mathrm{gas}} = 1.36\ n_{\mathrm{H}_2}\ m_{\mathrm{H}_2}, \tag{4.2}$$

where $m_{\mathrm{H}_2} = 2.0158$ amu is the mass of a H_2 molecule. The corresponding values are listed in Tab. 4.2.

The mean magnetic field strength in the region north of the center, northwest of the center, and east of the center of B335 can be estimated (see Tab. 4.2). In doing so, similar magnetic field strengths in the different regions are found, $B_{\mathrm{B335,\ near-IR}} \approx (12 - 40)\ \mu\mathrm{G}$, which are less, by a factor of $3 - 10$, than the estimated field strength in the sub-mm, $B_{\mathrm{B335,\ smm}} \approx 130\ \mu\mathrm{G}$ (Wolf et al. 2003). Considering the inaccuracies in the estimations of the densities, the temperatures, and the gas velocities, no significant difference in the magnetic field strengths in the inner and outer parts of B335 are found.

For CB68 and CB54, information about the gas densities, temperatures, and turbulence velocities is not available in the parts of the globules that the observation of this study trace in the near-IR and in the optical. However, in the sub-mm, Vallée et al. (2003) and Henning et al. (2001) estimate the magnetic field strengths of CB68 and CB54 to $B_{\mathrm{CB68,\ smm}} \approx 150\ \mu\mathrm{G}$ and $B_{\mathrm{CB54,\ smm}} \approx 60\ \mu\mathrm{G}$.

4.5. Correlation between magnetic field structure and CO outflow of the Bok globules

Magnetic fields are believed not only to influence the collapse of Bok globules but also the formation of circumstellar disks and outflows. Many observations show a preferential alignment of the outflow axis along the cloud-scale magnetic field (e.g., Cohen et al. 1984; Vrba et al. 1986; Jones & Amini 2003), but misaligned orientations of the outflow axes and magnetic field direction have been reported as well (e.g., Hull et al. 2013; Wolf et al. 2003). Based on magnetohydrodynamic (MHD) simulations, Matsumoto et al. (2006) find that the degree of alignment between outflow and magnetic field depends on the magnetic field strength: the stronger the magnetic field, the better the alignment. However, one has to keep in mind that these simulations consider only the most inner regions of globules with outflows on scales of 150 − 200 AU. Thus, it is uncertain whether the findings of Matsumoto et al. (2006) can be extended to the scales of the observations in this study.

In the following, the relative positions of the outflow axes and the magnetic field directions are estimated for the observations of the three Bok globules, B335, CB68,

Region	n_{H_2} (cm^{-3})	ρ_{gas} (g cm^{-3})	T_{kin} (K)	Δv (km s^{-1})	v_{turb} (km s^{-1})	N_{vec}	$\bar{\gamma}$ (deg)	σ_γ (deg)	B (μG)
center-north	1.3×10^3 (a)	5.92×10^{-21}	10 (a)	0.82 ± 0.01 (a)	0.74	5	135.42°	31.59°	21.14
center-east	1.3×10^3 (a)	5.92×10^{-21}	10 (a)	0.82 ± 0.01 (a)	0.74	9	122.89°	16.72°	39.93
northwest	1.8×10^3 (a)	8.19×10^{-21}	10 (a)	0.73 ± 0.02 (a)	0.62	6	111.84°	33.61°	19.58
	6.5×10^2 (a)	2.96×10^{-21}	20 (a)	0.73 ± 0.02 (a)	0.62	6	111.84°	33.61°	11.69

References. (a) Frerking et al. (1987).

Table 4.2.: Gas densities, gas velocities, polarization, and magnetic field strengths of the outer parts of B335 traced in the near-IR.

and CB54, which all contain protostellar cores and drive collimated CO outflows (Chandler & Sargent 1993; Vallée et al. 2000; Yun & Clemens 1994).

In discussing the relative orientation between the CO outflow and the magnetic field structure, one has to consider that only one component of the spatial orientation of the outflow ($v \sin i$) is known from velocity measurements and that polarization vectors only trace the magnetic field structure projected on the plane of sky. In the sub-mm, Wolf et al. (2003) and Vallée et al. (2003) find the polarization vectors aligned with the CO outflows and discuss the relation to the magnetic field structure traced by the polarization maps. This study extends this analysis to the outer, less dense regions traced by our near-IR and optical observations. Consistent with the sub-mm studies, it is assumed that the magnetic field is oriented parallel to the observed polarization vectors in the near-IR and the optical (for details see Sect. 4.4).

B335 (Fig. 4.4) – The near-IR observations of this study trace the outflow region in the eastern part of this globule. Here, the near-IR polarization vectors are oriented by an angle $\overline{\gamma} = 115.06° \pm 6.32°$ with respect to the outflow axis (P.A. $\approx$ 0°). The sub-mm polarization vectors are aligned nearly parallel to the outflow axis (Wolf et al. 2003). The globule itself is clearly elongated in the north-south direction (see Fig. 4.4). Therefore, the magnetic field orientation changes from the inner 7×10^3 AU, where it is perpendicular to the outflow and parallel to the globule, to the outer 2×10^4 AU, where it is inclined toward the outflow.

CB68 (Fig. 4.5) – The observed extent of the CO outflow is limited to the inner 1.6×10^4 AU, and thereby traced only by the near-IR polarization vectors in the southeastern part of this globule. These polarization vectors are oriented roughly perpendicular ($\overline{\gamma} = 78.95° \pm 6.45°$) to the outflow axis (P.A. = 142° and −38°) (Vallée et al. 2000). Relative to the pseudo-disk (P.A. $\approx 51° \pm 1°$), which is located in the center of this globule ($< 10^3$ AU), Vallée et al. (2003), they also find twisted sub-mm polarization vectors that they interpret as influenced by the outflow. However, on scales of about 2×10^3 AU, the magnetic field orientation is nearly perpendicular to the outflow axis, and thereby almost parallel to the pseudo-disk.

CB54 (Fig. 4.6) – The near-IR observations of this study trace the red-shifted CO outflow very well. The observations show polarization vectors that are almost perfectly aligned with the outflow axis. This corresponds well to the findings of Wolf et al. (2003) in the sub-mm, where a mean polarization orientation perpendicular to the outflow direction was found. The blue-shifted outflow lobe is barely traced by the near-IR polarization vectors that are almost perpendicular to the outflow lobe. However, one has to consider that the distance between the polarization vectors and the CO contour lines is large, and the CO outflow shows a dip toward the vectors.

The magnetic field direction is clearly parallel to the red-shifted CO outflow lobe on scales of about 5×10^4 AU.

Following the discussion by Matsumoto et al. (2006), the observations of this study indicate that the magnetic field of B335 is stronger relative to the outflow in the very outer parts of the globule than in the inner core and the other way around in the case of CB68, while the magnetic field of CB54 dominates the outflow along its complete extent. These findings cannot be verified by the analysis of the magnetic field strength in B335 using the CF method (for details, see Sect. 4.4). However, one has to keep in mind that these interpretation may be highly influenced by projection effects.

4.6. Summary

For the first time, multi-wavelength polarization maps have been obtained that cover the extent of Bok globules over a range of $10^2 - 10^5$ AU, covering optically thin and optically thick regions. In this study, the three globules B335, CB68, and CB54 were observed in the near-IR and in the optical. Additionally, these observations were combined with archival sub-mm and optical data. The major results follow.

1. The polarization degrees in the near-IR and in the optical amount to several percent ($2\ \% \lesssim P \lesssim 10\ \%$).
2. In the case of B335 and CB68, two simple structured Bok globules, the orientation of the sub-mm polarization vectors in the dense inner part ($10^2 - 10^3$ AU) of the globules continue to the outer, less dense globule parts ($10^4 - 10^5$ AU).
3. In the case of CB54, a globule with large-scale turbulences, the orientation of the polarization vectors in the near-IR is well-ordered on scales of $\sim 10^4$ AU.
4. In the case of B335, comparable magnetic field strengths are found in the globule parts traced by the near-IR observations and in the parts traced by sub-mm observations, by using the CF method.
5. No general correlation could be found between the magnetic field structure and the CO outflow of the Bok globule. In CB54 a magnetic field orientation parallel to the CO outflow is found, while B335 shows a change in the orientation of the magnetic field toward the outflow axis from the inner core to the outer regions. In CB68, a magnetic field orientation nearly perpendicular to the CO outflow is found.
6. The instrumental polarization of ISAAC/VLT depends significantly on the elevation angle of the telescope. For the unpolarized standard star, EGGR118, the deviation of the polarization degree, $\Delta P \approx 1.4\ \%$, was determined.

The well-ordered polarization vectors indicate dominant magnetic fields from scales of $10^2 - 10^3$ AU to scales of $10^4 - 10^5$ AU. In the particular case of CB54, the randomly oriented polarization pattern in the sub-mm can be explained by, e.g., a change in the orientation from the region south of the sub-mm map to the region north of the sub-mm map (see Fig. 4.6).

A gap remains with a width of about $1' - 2'$ between the sub-mm observations conducted with SCUBA/JCMT and the near-IR observations performed with ISAAC/VLT and SOFI/NTT of B335, CB68, and CB54. Launhardt et al. (2013) derive typical hydrogen column densities for the region traced by the SCUBA/JCMT observations in Bok globules of $N_{\mathrm{H}} \gtrsim 10^{22}$ cm^{-2}, as well as $N_{\mathrm{H}} \lesssim 10^{21}$ cm^{-2}, for the regions observed with ISAAC/VLT and SOFI/NTT. To close the gap and, finally, spatially connect the magnetic field observations from the smallest to the largest scale, observations that trace the region of 10^{21} cm$^{-2} \lesssim N_{\mathrm{H}} \lesssim 10^{22}$ cm^{-2} need to be done. Based on the flux level determined at the edges of the sub-mm map of B335 and CB54 observed with SCUBA/JCMT (Wolf et al. 2003; Henning et al. 2001), in the context of this study, it is estimated that these observations can be performed in less than one hour with ALMA since cycle 2 (2014).

The key to understanding the influence of magnetic fields on the low-mass star formation process is knowledge about the three-dimensional structures of the magnetic field and the object itself. The presented observations, as well as all observations, suffer from projection effects along the line of sight. Thus, it is necessary to do three-dimensional modeling of Bok globules, which includes a proper description of dust, dust grain alignment, gaseous outflows, and polarimetric radiative transfer, in addition to polarimetric observations. However, this type of analysis is beyond the scope of this multi-wavelength polarimetry study.

Part II.

Magnetic Fields In Protoplanetary Disks – Simulations

5. Basics of radiative transfer and magnetic fields in protoplanetary disks

As introduced at the beginning of this thesis, part II addresses radiative transfer simulations of polarized dust emission of protoplanetary disks. The basis for this is presented in this chapter. In Sect. 5.1, the basic physics of magnetic fields in protoplanetary disks is described and Sect. 5.2 deals with the basics of radiative transfer of polarized dust emission. The extensions of the radiative transfer code MC3D (Wolf et al. 1999; Wolf 2003*b*) conducted in the context of this thesis are presented in chapter 6.

5.1. Magnetic fields in protoplanetary disks

Many physical processes in protoplanetary disks are affected by magnetic fields. Magnetic fields influence the transport of dust and gas (e.g., Ciesla 2007; Turner et al. 2014), the disk chemistry (e.g., Semenov et al. 2006), the meteoritic composition (e.g., Boss 2004), and the migration of planetesimals within the disk (e.g., Chambers 2006) through magnetohydrodynamic (MHD) turbulence. Even more importantly, MHD turbulence can provide the source of viscosity that drives the accretion (Lynden-Bell & Pringle 1974), and thus, the evolution of the disk (Shakura & Sunyaev 1973). One of the most promising mechanisms for driving turbulence, respectively accretion is the magneto-rotational instability (MRI; Balbus & Hawley 1991, 1998). Turbulence in unmagnetized disks is ineffectual in redistributing the angular momentum in the disks, thus, magnetic fields are needed to enable Shakura-Sunyaev viscosity (Balbus et al. 1996). The ionization fraction in the disk is high enough for magnetic coupling of material over large parts of the disk especially the thermally ionized inner disk and the highly ionized outer disk parts (e.g., Turner et al. 2007; Cleeves et al. 2015; Flock et al. 2015). However, the magnetic field properties of the disk, the field strength and structure, are still unconstrained.

Spatially resolved observations of polarized millimeter continuum emission of aligned dust grains are best suited to reveal the magnetic field strength and structure in the protoplanetary disk (e.g., Weintraub et al. 2000; Cho & Lazarian 2007). Within the disk, dust grains are aligned with the magnetic field by radiative torques. In the presence of an anisotropic radiation field, non-spherical dust grains, which have different cross section for left- and right-handed polarized light, get aligned with their longest grain axis perpendicular to the magnetic field (e.g., Dolginov & Mytrophanov 1976; Lazarian 2007). Additional grain alignment mechanisms, i.e., paramagnetic alignment and mechanical alignment by either supersonic or subsonic flows, are negligible: Paramagnetic alignment (Davis & Greenstein 1951) affects only dust grains smaller than 0.1 μm (Lazarian et al. 2015). Mechanical alignment by supersonic flows (Purcell 1969) does not occur because of purely widely observed subsonic velocities, (e.g., Hughes et al. 2011) and because of the subsonic nature of MRI turbulence (Flock et al. 2011). And mechanical alignment by subsonic flows (Lazarian & Hoang 2007*b*) appears to be inefficient in general, since non-spherical grains may not show well-defined helicity in the process of grain interaction with gaseous flows (Lazarian et al. 2015). In brief, the usual picture of non-spherical grains aligned perpendicular to magnetic field lines applies. The polarized thermal emission of these grains traces the magnetic field strength and structure within a protoplanetary disk. Here begins the second part of this thesis. Polarimetry is strongly influenced by many factors, e.g., dust grain shapes, dust grain alignment efficiency, magnetic field properties, and the projection effect along the line of sight. To take these effects into account, 3-dimensional radiative transfer simulations, i.e., simulated observations, are used as analysis tools for intensive interpretation and prediction of observational results. In the context of this thesis, one of the first radiative transfer codes that considers the effects of polarized dust emission and dust grain alignment has been developed by extending the established code MC3D (Wolf et al. 1999; Wolf 2003*b*). In the following, the basics of these radiative transfer simulations are described.

5.2. Radiative transfer simulations

This section addresses the basics of radiative transfer (Sect. 5.2.1), describes the code MC3D that was extended in the context of this thesis (Sect. 5.2.2), as well as the applied dust model (Sect. 5.2.3) and disk model (Sect. 5.2.4).

5.2.1. Radiative transfer

Radiative transfer is the basis of simulated observations which are needed to connect observational results with theoretical predictions. In general, radiative transfer describes the propagation of photons through a medium. In this thesis, the medium shall be a protoplanetary disk, consisting of gas and dust, around a central star, the primary radiation source. To simulate the photon propagation properly, it is necessary to consider the interaction of the photons with the disk material. The central star is described as a black body following Planck's law,

$$B_\nu\left(T\right) = \frac{2h\nu^3}{c^2}\,\frac{1}{\exp\left(\frac{h\nu}{k_\mathrm{B}T}\right)-1}\,, \tag{5.1}$$

where the spectral radiance B_ν is defined by a temperature T, a frequency ν, c as speed of light, h as Planck constant, and k_B as Boltzmann constant. Its spectral energy distribution and spatial brightness distribution depend on the dust within the disk. The photons travelling through the disk interact with dust grains by scattering, absorption, and emission. These photon-dust interactions are described by the equation of radiative transfer, here in the one-dimensional, time independent form (e.g., Unsöld & Bascheck 1988):

$$\frac{\mathrm{d}I_\nu}{\mathrm{d}s} = -k_\nu I_\nu + j_\nu. \tag{5.2}$$

It describes the change in intensity, I_ν, at a given frequency ν along the path s. This intensity change depends on the extinction coefficient, k_ν, along the path and the emission coefficient, j_ν. The extinction coefficient, in turn, is composed of the absorption coefficient, κ_ν, and the scattering coefficient, σ_ν. These coefficients are dependent on the material properties and the density distribution along the path s. Under the assumption of local thermodynamic equilibrium and following Kirchhoff's law of thermal radiation, the emission coefficient can be written as

$$j_\nu = \kappa_\nu B_\nu\left(T_\mathrm{d}\right), \tag{5.3}$$

with the dust temperature T_d (e.g., Kirchhoff 1860; Unsöld & Bascheck 1988).

Another quantity to describe the optical properties of the material along the path s is the frequency-dependent optical depth

$$\tau_\nu = \int_0^s \left(\kappa_\nu + \sigma_\nu\right)\mathrm{d}s. \tag{5.4}$$

By assuming that the medium is filled with homogeneous spheres (see Sect. 5.2.3), the absorption and emission of radiation can be derived by Mie theory (Mie 1908; Bohren & Huffman 1998). Based on the complex refractive index of the material and the dimensionless size parameter $x = 2\pi a\,/\,\lambda$, where $2\pi a$ is the circumference of the sphere and λ is the wavelength of the radiation, the cross sections for absorption C_abs, for scattering C_sca, and for extinction $C_\mathrm{ext} = C_\mathrm{abs} + C_\mathrm{sca}$, can be derived. Usually, either these cross sections or the dimensionless efficiency factors normalized to the geometrical cross sectional area, are given,

$$Q_{\mathrm{abs/sca/ext}} = \frac{C_{\mathrm{abs/sca/ext}}}{\pi a^2}. \tag{5.5}$$

With these coefficients and the equations above, the transfer of radiation along path s can be calculated.

5.2.2. The code to start with: MC3D

Radiative transfer is implemented in a number of codes (e.g., D'Alessio et al. 1998; Pinte et al. 2006; Dullemond 2012). In this thesis, the 3D radiative transfer code MC3D (Wolf et al. 1999; Wolf 2003*b*) is used as a basis. For a given central star and dust density distribution, MC3D simulates temperature distributions, spectral energy distributions, spatially resolved intensity maps, as well as polarization maps of scattered light. MC3D solves the radiative transfer equation indirectly using the Monte Carlo Method (e.g., Kroese et al. 2011). The path of a photon is traced from the central star, where it is emitted, along its way through the given density structure. Along this path, absorption and re-emission, as well as single and multiple scattering and anisotropic scattering effects are considered stochastically. MC3D simulates the radiative transfer problem self-consistently, i.e., based on the given density distribution. Temperature and therefore intensity result from the stellar heating and/or dust re-emission. The computation of the temperature distribution is based on the method of Bjorkman & Wood (2001) and on the concept for treating the absorption of radiation by Lucy (1999) which enables the simulations of thermal dust re-emission. For the scattering, the approach of Cashwell & Everett (1959) is used. The optical dust parameters, absorption, scattering, and extinction cross-sections are calculated via Mie theory (Mie 1908; Bohren & Huffman 1998). MC3D divides the model space into volume elements and assumes a local thermodynamic equilibrium in each of these cells. This thesis makes use of a spherical grid with a single star in the center. In (θ, φ)-directions, the grid is divided equidistantly, in r-direction logarithmically.

5.2.3. Dust model

To model dust, a dust density distribution (see Sect. 5.2.4) and a model for the dust grain itself is needed. Since Mie theory describes only compact, homogeneous, isotropic, spherical particles, MC3D processes only such ones (see chapter 6 for non-spherical grains). In this thesis, the basic dust model is assumed to be a homogeneous sphere with spatially independent optical properties. Of course, real dust grains have much more sophisticated structures. However, shape, chemical composition, and size of dust grains can be traced in astronomical observations only averaged over the complete sample (Voshchinnikov 2004). This motivates the usual restriction of dust models to the simplest but least ambiguous grain model, the homogeneous sphere. The necessary extensions for thermal polarization and grain alignment of non-spherical dust grains are discussed in chapter 6.

The dust is chemically composed of astronomical silicate and graphite in a mixing ratio of 62.5% : 37.5% (Draine & Lee 1984; Weingartner & Draine 2001). A grain has a median density of $\rho_{\mathrm{dust}} = 2.5\,\mathrm{g\,cm^{-3}}$. This dust model is a standard approach in circumstellar disk modeling and well tested (e.g, Sauter et al. 2009; Gräfe et al. 2013). Since graphite has highly anisotropic dielectric functions, its optical properties are computed on the basis of the so-called "2/3 − 1/3" approximation for the averaged extinction factors (e.g., Draine & Malhotra 1993),

$$Q_{\mathrm{ext}} = \frac{2}{3}\,Q_{\mathrm{ext}}(\epsilon_{\perp}) + \frac{1}{3}\,Q_{\mathrm{ext}}(\epsilon_{\parallel})\,, \tag{5.6}$$

where $\epsilon_{\perp}$ and $\epsilon_{\parallel}$ are the dielectric functions for two cases of orientation of the electric field relative to the basal plane of the graphite. $Q_{\mathrm{ext}}(\epsilon_{\perp})$ and $Q_{\mathrm{ext}}(\epsilon_{\parallel})$ are calculated with the Mie theory. Draine & Malhotra (1993) demonstrated the sufficient accuracy of this approximation.

The distribution of dust grain sizes is described by a power law (Dohnanyi 1969; Mathis et al. 1977)

$$\mathrm{d}N \sim a^{q}\,\mathrm{d}a \qquad \text{with} \qquad q = -3.5 \qquad \text{and} \qquad a_{\min} \leq a \leq a_{\max} \tag{5.7}$$

where a is the radius of the dust grain and $N(a)$ is the number of grains with a given radius. The assumed dust grain sizes, in particular the maximum grain size, $a_{\max}$, depends on the evolutionary stage of the modeled object. For very young objects of star and planet formation, e.g., Bok globules and Class 0/I objects, the commonly known MRN (Mathis-Rumpl-Nordsieck distribution; Mathis et al. 1977) dust distribution with grain sizes in the interval [5 nm, 250 nm] is used. In older disks, e.g., T Tauri disks, grain growth has occurred and dust grains up to ∼ 1 mm and even larger can be found (e.g., Gräfe et al. 2013). However, the implementation of thermal polarization and dust grain alignment is not sensitive to changes of this order of magnitude.

As shown by Wolf (2003*a*), the observational quantities computed with radiative transfer simulations considering each grain size separately are in good agreement with the result of radiative transfer simulations that consider a weighted average dust grain size. To optimize computing time, MC3D uses the weighted average dust grain size of a given grain size distribution.

5.2.4. Disk model

The underlying disk model is a flared disk, known as the Shakura-Sunyaev density distribution (Shakura & Sunyaev 1973), described by the dust and gas distribution,

$$\rho_{\text{disk}}\left(r,z\right)=\rho_0\left(\frac{r_0}{r_{\text{z}}}\right)^{\alpha}\exp\left(-\frac{1}{2}\left[\frac{z}{h\left(r_{\text{z}}\right)}\right]^2\right)\,, \tag{5.8}$$

with the radial distance r_{z} and the height above the mid-plane of the disk, z. The density parameter ρ_0 is determined by the total dust mass, m_{dust}, of the disk. The reference radius r_0 is usually set to 100 AU, and the vertical scale height of the disk $h\left(r_{\text{z}}\right)$, i.e. the disk height at which the disk density is reduced to $e^{-1/2}$ of the mid-plane density, is defined by

$$h\left(r_{\text{z}}\right)=h_0\left(\frac{r_{\text{z}}}{r_0}\right)^{\beta} \tag{5.9}$$

which is scaled by $h_0=h(r_0)$. The parameters α and β define the radial density profile as well as the flaring of the disk. The disk model has an inner radius, r_{in}, and an outer radius, r_{out}. These five parameters specify the disk. This disk model approach is observationally motivated and approved (e.g., Stapelfeldt et al. 1998; D'Alessio et al. 1999; Pinte et al. 2008; Sauter et al. 2009; Gräfe et al. 2013). Unless stated otherwise, this disk model is used with the parameters $\alpha=1.875$, $\beta=1.125$, $h_0=10\,\text{AU}$, $r_0=100\,\text{AU}$.

6. The extended MC3D: thermal polarization and grain alignment

The goal of this second part of this thesis is the development of one of the first radiative transfer codes capable of simulating the polarized thermal dust emission of aligned non-spherical dust grains within protoplanetary disks. This was done on the basis of the radiative transfer code MC3D (Wolf et al. 1999; Wolf 2003*b*; see Sect. 5.2.2). In this chapter, the implementation and the underlying theoretical background of dust grain alignment (Sect. 6.2) and thermal polarization (Sect. 6.3) of non-spherical grains are described. Furthermore, tests, including benchmark tests, are presented in Sect. 6.4. Applications of the extended MC3D are discussed in Sect. 6.5 and Sect. 6.6 summarizes part II of this thesis. This chapter begins with a discussion of the treatment of non-spherical grains within MC3D.

6.1. From sphericity to asphericity

The thermal dust emission is intrinsically polarized only if the grain is not spherically shaped. Up to this point, MC3D focused solely on the simulation of spherical grains. The key issue to this limitation is solving the light scattering problem for a given dust grain shape. There are different approaches, exact methods like the separation of variables method (SVM; e.g., Mie 1908; Voshchinnikov & Farafonov 1985, 1993), the T-Matrix method (TMM; e.g., Waterman 1971; Barber & Yeh 1975), and the discrete dipole approximation (e.g., Purcell & Pennypacker 1973; Draine 2000), as well as approximate approaches like the quasi-static approximation (e.g., van de Hulst 1957; Bohren & Huffman 1998), and the S-approximation (e.g., Perelman 1979; Perelman & Voshchinnikov 2002). The choice between exact and approximate methods is given by their dependence on:

1. the size parameter $x = 2\pi a \,/\, \lambda$, where a is the typical size of a grain, e.g., the radius of the equivolume sphere, and λ the wavelength of the incident radiation;
2. the modulus of the difference between the refractive index and unity $|m-1|$;
3. the phase shift $p = 2x\,|m-1|$.

The approximate approaches are well suited if at least two of these quantities are much smaller or larger than unity (van de Hulst 1957). They give estimations of the wavelength dependence extinction cross-sections, and thus, the interstellar extinction $A(\lambda)$. Observations show that $A(\lambda) \propto \lambda^{-1}$ in the visible part of the spectrum. None of the approximate approaches predicts such a wavelength dependency (Voshchinnikov et al. 2000). Therefore, it is recommendable to restrict the work to exact methods. Those exact methods, on the other hand, differ a lot in applicability, dependent on the size parameter x (see Fig. 6.1). SVMs like Mie theory, the method used by MC3D to solve the scattering problem, cover a wide range of size parameters.

The goal of this second part of this thesis is to implement the effects of thermal polarization and grain alignment into MC3D. To achieve this, a middle ground between the original design of MC3D and the needs of asphericity of dust grains in terms of thermal polarization and dust grain alignment is applied. The usual approach for this is to surrogate the aspherical grain by its equivolume sphere, i.e., the sphere with the same volume as the aspherical grain (e.g., Draine & Weingartner 1997; Voshchinnikov et al. 2000; Khlebtsov et al. 2011). The equivolume sphere is characterized by the equivolume radius r_V. For that reason, MC3D processes the photons through the model space assuming equivolume spheres while it calculates dust temperature distributions and anisotropy of the radiation field, and consideres non-spherical grains for calculating the polarization state (performed in an additional run of the code).

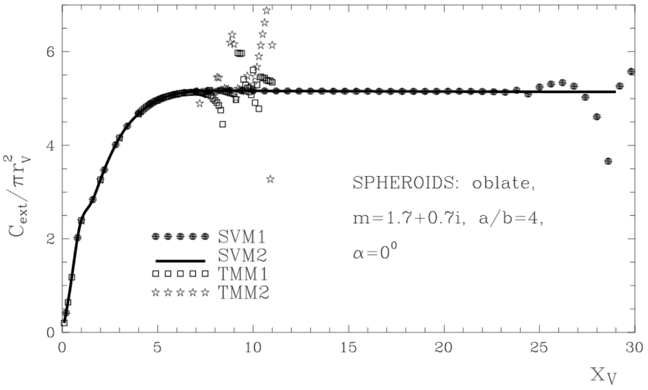

Fig. 6.1.: SVM vs TMM. The normalized extinction cross-section vs the size parameter x_V, for grains with the refractive index m, axis ratio a/b expressed by the equivolume radius r_V , and a propagation direction of the wave along the rotation axis of the grain α (reproduced from Voshchinnikov et al. 2000; with permission from Elsevier). Different methods cover different x_V ranges. Thus, their applicability depend on the problem.

6.2. Dust grain alignment

There are various grain alignment mechanisms, as pointed out in Sect. 2.4.3. The most conclusive of them, considering the typical dust grain sizes found in protoplanetary disks, are radiative torques. On the basis of Cho & Lazarian (2007), henceforth CL07, radiative torques have been implemented. CL07 had been limited to a rather simple disk model and had not been able to take the anisotropy of the radiation field into account. However, with MC3D it has been possible to combine radiative torques, a sophisticated disk model, and the anisotropy of the radiation field. The formulation of radiative torques used in this thesis as well as in CL07 goes back to the fundamental work of Draine & Weingartner (1996) which is described in this section.

To characterize the alignment of dust grains by radiative torques, it is necessary to consider the radiative forces and torques on the grain due to starlight. For a given grain exposed to an anisotropic radiation field with the energy density $\gamma_{\mathrm{rad}} u_{\mathrm{rad}}$, the force and torque on the grain are described by

$$\begin{aligned} \vec{F}_{\mathrm{rad}} &= \pi a_{\mathrm{eff}}^2 \gamma_{\mathrm{rad}} u_{\mathrm{rad}} \left\langle \vec{Q}_{\mathrm{pr}} \left(\theta, \varphi\right) \right\rangle , \\ \vec{\Gamma}_{\mathrm{rad}} &= \pi a_{\mathrm{eff}}^2 \gamma_{\mathrm{rad}} u_{\mathrm{rad}} \frac{\lambda}{2\pi} \left\langle \vec{Q}_{\Gamma} \left(\theta, \varphi\right) \right\rangle , \end{aligned} \tag{6.1}$$

with the (effective) grain radius a_{eff}, wavelength λ, the spectrally averaged energy density, u_{rad}, as well as efficiency factors of radiation pressure, $\vec{Q}_{\mathrm{pr}} \left(\theta, \varphi\right)$, and radiation torque, $\vec{Q}_{\Gamma} \left(\theta, \varphi\right)$:

$$u_{\mathrm{rad}} \equiv \int_0^\infty u_\lambda \mathrm{d}\lambda \, , \tag{6.2}$$

$$\left\langle \vec{Q}_{\mathrm{i}} \left(\theta, \varphi\right) \right\rangle \equiv \frac{\int_0^\infty \vec{Q}_{\mathrm{i}} \left(\theta, \varphi\right) \lambda u_\lambda \mathrm{d}\lambda}{\int_0^\infty \lambda u_\lambda \mathrm{d}\lambda}, \quad \text{with} \quad i = \begin{cases} \mathrm{pr}, \\ \Gamma \end{cases} , \tag{6.3}$$

and the anisotropy factor γ_{rad},

$$\gamma_{\mathrm{rad}} = \frac{\left| \int_\Omega I_\lambda \left(\vec{k}\right) \vec{k} \, \mathrm{d}\Omega \right|}{\int_\Omega I_\lambda \left(\vec{k}\right) \mathrm{d}\Omega} , \tag{6.4}$$

with the wave vector $\vec{k}$, the wavelength-dependent intensity I_λ, and the solid angle Ω.

Dust grains in the disk are surrounded by gas, so that rotational damping caused by gas-dust collisions must also be considered. For a grain in a neutral gas of hydrogen density $n_\mathrm{H} = n(H) + 2n(H_2)$ and temperature T, the gas drag torque on a grain with angular velocity ω around axis $\vec{a}_1$ can be written as

$$\vec{\Gamma}_\mathrm{drag,gas} = -\frac{2}{3}\delta n_\mathrm{H}\,(1.2)\,(8\pi m_\mathrm{H} k_\mathrm{B} T)^{1/2}\, a_\mathrm{eff}^4 \omega \vec{a}_1, \tag{6.5}$$

where m_H is the mass of an H atom and k_B is the Boltzmann constant. If all impinging gas atoms *stick* to a grain and then leave with negligible velocity relative to the local (moving) surface, then the geometrical parameter $\delta = 1$ in the case of a spherical grain, and $\delta = 2(\pi/3)^{1/3} = 2.01$ for an aspherical grain with axis ratio 2:2:1. The factor 1.2 in Eq. (6.5) takes effects of helium with $n_\mathrm{He} = 0.1 n_\mathrm{H}$ into account. Here, it is assumed that H is fully atomic, in the case of a fully molecular gas, the factor 1.2 should be replaced by 0.907.

Assuming that the grain is subject to a steady radiative torque along the grain rotation axis $\vec{a}_1$,

$$\vec{\Gamma}_\mathrm{rad} = \pi a_\mathrm{eff}^2 \gamma_\mathrm{rad} u_\mathrm{rad} \frac{\lambda}{2\pi} \left\langle \vec{Q}_\Gamma(\theta, \varphi) \right\rangle \cdot \|\vec{a}_1\|^2, \tag{6.6}$$

which shall be the only source of rotational excitation, i.e., mechanical alignment is ignored. By evaluating Eq. (6.5), (6.6) (under consideration of rotational damping times, τ, see below), it is found that the grain will rotate around $\vec{a}_1$ with an angular velocity

$$\omega_\mathrm{rad} = \frac{5\lambda}{8\delta a_\mathrm{eff}^2} \left(\frac{k_\mathrm{B} T}{8\pi m_\mathrm{H}}\right)^{1/2} \left(\frac{u_\mathrm{rad}}{n_\mathrm{H} k_\mathrm{B} T}\right) \gamma_\mathrm{rad} \left\langle \vec{Q}_\Gamma(\theta, \varphi) \right\rangle \cdot \vec{a}_1 \left(\frac{\tau_\mathrm{drag}}{\tau_\mathrm{drag,gas}}\right). \tag{6.7}$$

Additionally to $\left\langle \vec{Q}_\Gamma(\theta, \varphi) \right\rangle \cdot \vec{a}_1$, ω_rad depends on the ratio of radiation pressure to gas pressure $(u_\mathrm{rad}/n_\mathrm{H} k_\mathrm{B} T)$, on the anisotropy factor γ_rad, and the rotational damping times

$$\tau_\mathrm{drag}^{-1} = \tau_\mathrm{drag,gas}^{-1} + \tau_\mathrm{drag,em}^{-1}, \tag{6.8}$$

composed of i) rotational damping caused by gas-dust collisions,

$$\tau_\mathrm{drag,gas} = \frac{\pi \alpha_1 \rho a_\mathrm{eff}}{3\delta n_\mathrm{H}\,(2\pi m_\mathrm{H} k_\mathrm{B} T)^{1/2}}, \tag{6.9}$$

where α_1 is a geometrical parameter, and of ii) rotational damping caused by absorption and emission of photons by the grain (Purcell & Spitzer 1971; Roberge et al. 1993). Assuming that the grain is heated by the star to a temperature T_{dust}, then the damping time due to thermal emission may be written as

$$\tau_{\mathrm{drag,em}} = \frac{8\,\alpha_1\,(\beta+3)}{5}\,\frac{\zeta\,(\beta+4)}{\zeta\,(\beta+3)}\,\frac{\rho a_{\mathrm{eff}}^3\,(k_{\mathrm{B}}T_{\mathrm{dust}})^2}{\hbar c u_{\mathrm{rad}}\,\langle Q_{\mathrm{abs}}\rangle}\,. \tag{6.10}$$

$\zeta(x)$ depicts the Riemann ζ-function, and the parameter $\beta = 2$ which is a constant of order unity and depends on the character of the scattering at the boundary (Draine & Lee 1984; Draine 1994). However, the rotational damping time $\tau_{\mathrm{drag,em}}$ is insensitive to the exact value of β (Draine & Weingartner 1996). In Eq. (6.10) it is assumed that emitted photons have angular momentum $\hbar$ relative to the grain center of mass which is true for $a \ll hc/k_{\mathrm{B}}T_{\mathrm{dust}} = 800\,(18\mathrm{K}/T_{\mathrm{dust}})\,\mu\mathrm{m}$ and fulfilled by typical conditions in protoplanetary disks. The additional damping caused by absorption of photons is smaller than the damping time due to thermal emission by a factor $\sim T_{\mathrm{dust}}/T_{\mathrm{rad}} \approx 1/500$, where T_{rad} is the color temperature of the dust heating radiation (Purcell 1979), and thus, it is neglected. However, as the calculations in this thesis and in CL07 show, the term $(\tau_{\mathrm{drag}}/\tau_{\mathrm{drag,gas}})^2 \approx 1$ throughout in the disk.

While the grain is subject to a steady radiative torque, the rotational energy will exceed $k_{\mathrm{B}}T/2$ by a factor

$$\begin{aligned}\left(\frac{\omega_{\mathrm{rad}}}{\omega_{\mathrm{T}}}\right)^2 &= \frac{5\alpha_1}{192\delta^2}\left(\frac{u_{\mathrm{rad}}}{n_{\mathrm{H}}k_{\mathrm{B}}T}\right)^2\left(\frac{\rho a_{\mathrm{eff}}\lambda^2}{m_{\mathrm{H}}}\right)\gamma_{\mathrm{rad}}^2\left\langle\vec{Q}_\Gamma\,(\theta,\varphi)\right\rangle^2\cdot\vec{a}_1^{\,2}\left(\frac{\tau_{\mathrm{drag}}}{\tau_{\mathrm{drag,gas}}}\right)^2\\ &= 4.72\times10^9\cdot\frac{\alpha_1}{\delta^2}\rho_3 a_{-5}\left(\frac{\gamma_{\mathrm{rad}}\cdot u_{\mathrm{rad}}}{n_{\mathrm{H}}k_{\mathrm{B}}T}\right)^2\left(\frac{\lambda}{1\,\mu\mathrm{m}}\right)^2 Q_\Gamma^2\left(\frac{\tau_{\mathrm{drag}}}{\tau_{\mathrm{drag,gas}}}\right)^2\,.\end{aligned} \tag{6.11}$$

where ω_{T} is the thermal angular frequency, which is the rate at which the rotational kinetic energy of the grain is equal to $k_{\mathrm{B}}T/2$, $Q_\Gamma = \left\langle\vec{Q}_\Gamma\,(\theta,\varphi)\right\rangle\cdot\vec{a}_1$, the geometrical parameters $\delta \approx 2$, $\alpha_1 \approx 1.745$ for a grain with axis ratio 2:2:1, gas mass density $\rho_3 = \rho/3\,\mathrm{g\,cm^{-3}}$ (assuming a gas-to-dust ratio of 100), and $a_{-5} = a/10^{-5}\mathrm{cm}$.

All quantities in Eq. (6.11) can be extracted from MC3D or are fixed parameters, except for the efficiency factor of radiative torques, Q_Γ. The computation of Q_Γ for non-spherical dust grains were performed by Cho & Lazarian (2005) and Lazarian & Hoang (2007*b*) for grains with equivolume radii between $0.1\,\mu$m and $100\,\mu$m (see Fig. 6.2). However, in protoplanetary disks dust grains already started to grow and have sizes of about $1000\,\mu$m. For the resulting λ/a ratios, the computational time of DDSCAT increases significantly. For this reason, it is more applicable to approximate Q_Γ (see Fig. 6.2) with

$$Q_\Gamma = \begin{cases}\sim\mathcal{O}(1) & \text{, if } \lambda\sim a\,,\\ \sim(\lambda/a)^{-1/3} & \text{, if } \lambda > a.\end{cases} \tag{6.12}$$

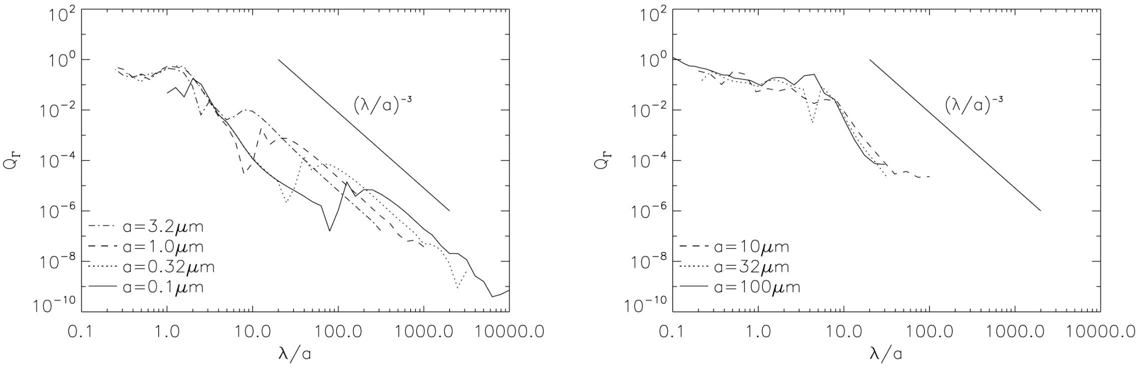

Fig. 6.2.: Behavior of the radiative torque: Based on DDSCAT simulations (*left panel:* Cho & Lazarian (2005); *right panel:* Lazarian & Hoang (2007*b*)), it can be approximated that $Q_\Gamma \sim \mathcal{O}(1)$ for $\lambda \sim a$, where a is the grain radius and λ the wavelength, and $Q_\Gamma \sim (\lambda/a)^{-1/3}$ otherwise (from CL07; reproduced with permission by AAS).

Together with Eq. (6.12), Eq. (6.11) may be written for $\lambda > a$ as

$$\left(\frac{\omega_\mathrm{rad}}{\omega_\mathrm{T}}\right)^2 \approx \left(\frac{\omega_\mathrm{rad}}{\omega_\mathrm{T}}\right)^2_{\lambda\sim\mathrm{a}} \left(\frac{Q_{\Gamma,\lambda\sim\mathrm{a}}}{Q_{\Gamma,\lambda}}\right)^2 \approx \left(\frac{\omega_\mathrm{rad}}{\omega_\mathrm{T}}\right)^2_{\lambda\sim\mathrm{a}} \left(\frac{\lambda}{a}\right)^{-6}, \tag{6.13}$$

where

$$\left(\frac{\omega_\mathrm{rad}}{\omega_\mathrm{T}}\right)^2_{\lambda\sim\mathrm{a}} \approx 4.72 \times 10^9 \, \frac{\alpha_1}{\delta^2}\, \rho_3 a_{-5} \left(\frac{\gamma_\mathrm{rad} u_\mathrm{rad}}{n_\mathrm{H} k_\mathrm{B} T}\right)^2 \left(\frac{\lambda}{1\,\mu\mathrm{m}}\right)^2 \left(\frac{\tau_\mathrm{drag}}{\tau_\mathrm{drag,gas}}\right)^2. \tag{6.14}$$

Grains with rotational energies much higher compared to thermal energy will stably align with the magnetic field. This condition is satisfied by $(\omega_\mathrm{rad}/\omega_\mathrm{T})^2 > 10$, as shown in the stability study of Draine & Weingartner (1997). It is assumed that all grains in the current cell are perfectly aligned as soon as $(\omega_\mathrm{rad}/\omega_\mathrm{T})^2 > 10$.

In the context of this thesis, Eq. (6.13) was implemented in MC3D. Tests, including benchmark tests with the results published in CL07 that demonstrate the successful implementation of grain alignment by radiative torques into MC3D are described in Sect. 6.4.

6.3. Thermal polarization

The emitted radiation of non-spherical dust grains is intrinsically polarized due to their non-spherical shape (see Sect. 2.4.2 for details). The relative orientation of the grain within the model space as well as the grain shape have to be considered while implementing the code. Both of them determine the shape of the polarization ellipse (see Fig. 2.8), and thus, the polarization state of the emitted wave. The angles γ, the polarization angle, and η, the opening angle of the polarization ellipse, define these parameters and are put directly into the Stokes parameters (see Eq. 2.3).

To compute the thermal polarization correctly, it is necessary to know exactly the relations between the coordinate system of the grain, i.e., the reference frame of the grain defined in Cartesian coordinates, the cell frame defined in spherical coordinates, the photon frame defined in Cartesian coordinates, and the observer's frame defined in spherical coordinates. The relative positions between all of these frames are known and can be handled with the usual rotation matrices. The procedure to compute the polarization of the thermal grain emission is implemented in a sequence of three steps, as outlined below.

Step 1: Determining the local magnetic field structure. It starts with the magnetic field structure which is defined by one 3-dimensional Cartesian vector for each cell. This vector represents the mean magnetic field within the cell.

In the context of this thesis, there are four optional definitions of a magnetic field vector given: a homogeneous magnetic field (e.g., $\vec{B} = (0,0,1) = \vec{e}_{\mathrm{z}}$), a toroidal magnetic field ($\vec{B} = (-y,x,0)$), an hourglass-shaped magnetic field ($\vec{B} = (\cos\varphi, \sin\varphi, 1)$), and the possibility to read-in a tabulated magnetic field, e.g., results of MHD simulations (see Sect. 6.5.2.2). Of course, these magnetic field definitions can be adapted and extended as necessary.

Step 2: Know your observer. The implementation of thermal polarization computation of this thesis takes the approach to first rotate the magnetic field together with the aligned dust grain into the observer's frame, and then computes the state of polarization of the current cell. While the photon moves through the model space, its direction of motion is determined by scattering events. During its travel from cell to cell, the photon interacts with the matter inside the cell and leaves the cells under varying angles. Additionally, it is possible that a photon interacts multiple times within one cell. For thermal polarization, it is important to take the orientation of the Stokes vector of the emitted photon into account. By changing nothing but the direction of the emitted photon, the state of polarization changes. Thus, during the radiative transfer, the photon plays the role of the observer of the aligned dust grain. Hence, to compute the change of the polarization state of the photon on its way through the model space, the magnetic field along with the aligned dust grain is rotated into the photon frame.

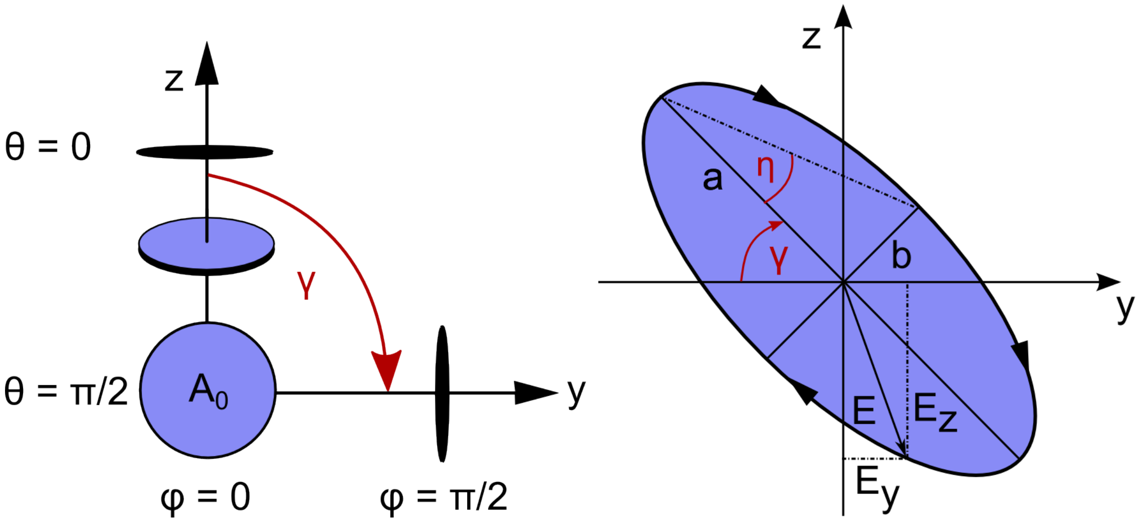

Fig. 6.3.: ANGLE DEFINITIONS FOR THERMAL POLARIZATION: *Left:* Within the photon frame (3D Cartesian coordinate system) the position and orientation of the grain can be defined relative to the photon which is, per definition, observing along the x-axis. The polarization angle, γ, and the opening angle of the ellipse, η, can be derived from the angles θ (xz-plane) and φ (xy-plane). The visible area of the grain surface is minimized for $\theta = 0$ or $\varphi = \pi/2$, and is maximized for $\theta = \pi/2$ or $\varphi = 0$. *Right:* The polarization ellipse (for details, see Fig. 2.8). The opening angle η can be expressed in the photon frame (resp. the observer's frame) by θ and φ as described in Eq. (2.2).

Step 3: What does the grain look like from the photon's point of view? Once the magnetic field vector and the dust grain are rotated into the photon frame, the following definitions can be made to quantify the projection of the grain (see Fig. 6.3). The magnetic field vector orientation and thus, the grain orientation within the photon frame are described by three angles, γ, θ, φ,

$$\begin{aligned} \gamma &= \arctan\left(B_{\mathrm{y}}/B_{\mathrm{z}}\right), \\ \theta &= \arctan\left(B_{\mathrm{x}}/B_{\mathrm{z}}\right), \\ \varphi &= \arctan\left(B_{\mathrm{x}}/B_{\mathrm{y}}\right). \end{aligned} \tag{6.15}$$

The angle γ enters the Stokes parameters (see Eq. 2.3) directly (see section 2.3.1). The opening angle η, also required in Eq. (2.3), can be expressed by the angles θ and φ. To compute the opening angle η, the approach derived in Bertrang (2010) is used here, which is described in the following. For the purposes of this description it is assumed that the grain is of oblate shape as sketched in Fig. 6.3. Since grain alignment requires a fast rotation of the grain, any non-spherical grain can be approximated by an oblate shape. The opening angle η is defined by the visible surface area of the grain, $A(\theta, \varphi)$. Following Fig. 6.3, $A(\theta, \varphi)$ can be described by

$$\begin{aligned} A(\theta) &= A_0 \left|\sin\theta\right| , \\ A(\varphi) &= A_0 \left|\cos\varphi\right| , \end{aligned} \tag{6.16}$$

where A_0 is the maximum of the visible surface area. Thus, $A(\theta, \varphi)$ reads

$$A(\theta, \varphi) = A_0 \left|\sin\theta \cdot \cos\varphi\right| . \tag{6.17}$$

For any symmetric grain, the observed length of its longest grain axis, a, is independent of the observer's position, i.e., θ and φ, thus

$$A_0 = \pi a^2. \tag{6.18}$$

This, together with the definition of η (see Eq. 2.2) and the common definition of the area of an ellipse, result in the opening angle dependence on the magnetic field vector orientation, given by θ and φ:

$$\eta\left(\theta, \varphi\right) = \arctan\left|\sin\theta \cdot \cos\varphi\right| . \tag{6.19}$$

Now, with the angles γ and η, as well as with the Stokes formalism (see Sect. 2.3.1), the thermal polarization can be computed by MC3D.

For testing this procedure, a model was set up with a spherical dust distribution $\rho(r) = r^{-1}$, perfectly aligned dust grains, and a homogeneous magnetic field $\vec{B} = \vec{e}_{\mathrm{z}}$. Analytical tests with this model show a very high accuracy of these simulations.

6.4. Tests and limitations of the code

The implementation of the computation of thermal polarization has been tested analytically which is not possible for the implementation of the anisotropy of the radiation field and the dust grain alignment. For this reason, tests have been conducted which are presented in this section. The first test is a comprehensible case of a spherical density distributions and discusses the corresponding distributions of temperature, anisotropy of the radiation field, and dust grain alignment (see Sect. 6.4.1). A more sophisticated case of a protoplanetary disks is described in Sect. 6.4.2 in the context of a benchmark test.

6.4.1. A simple test case: A sphere

As simple, comprehensible test case, a spherical dust density distributions, $\rho\left(r\right) = r^{-1}$, has been chosen with further model parameters described in Tab. 6.1. Based

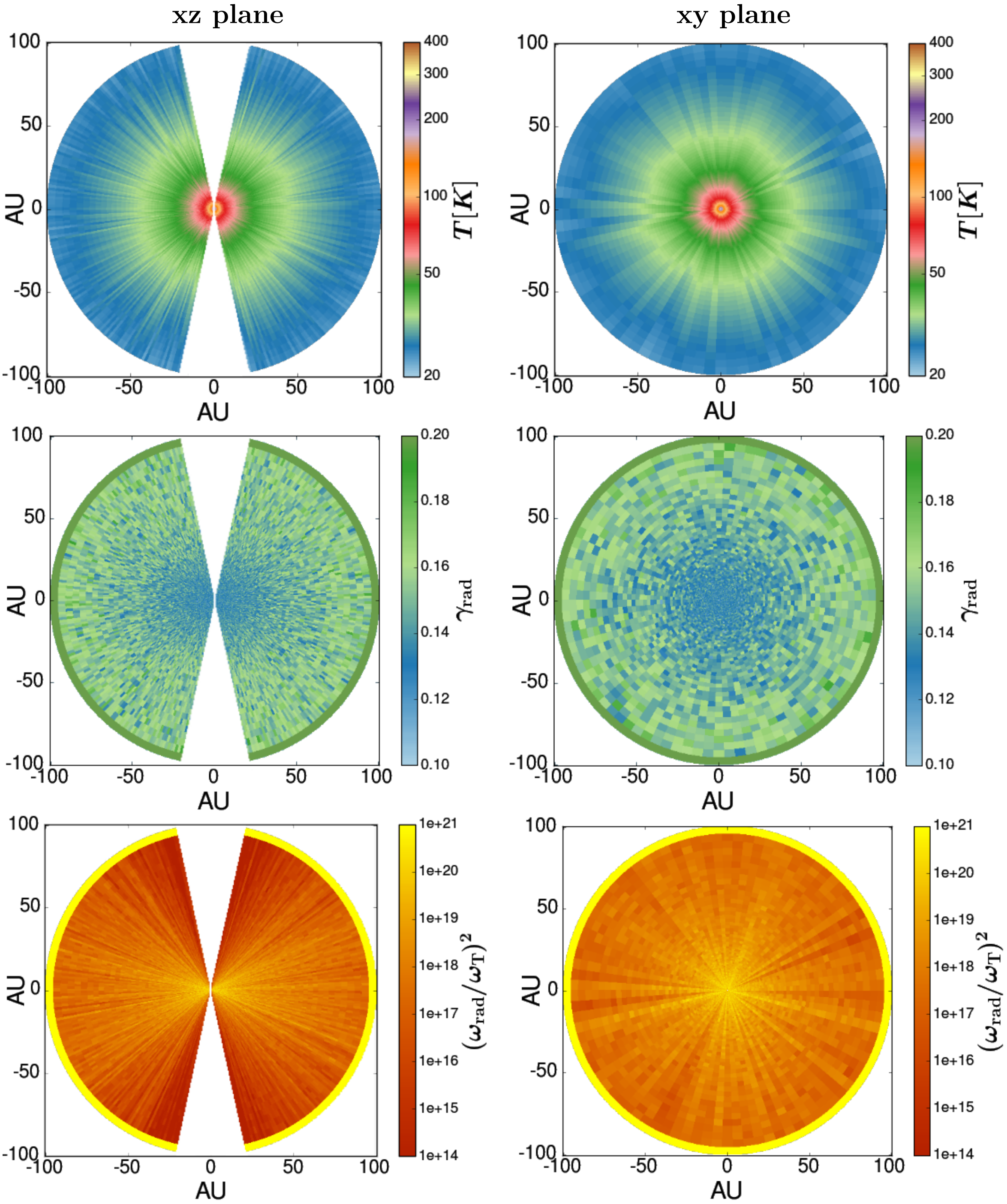

Fig. 6.4.: A SPHERICAL DUST DENSITY DISTRIBUTION in temperature T (*top row*), anisotropy of the radiation field $\gamma_{\rm rad}$ (*middle row*), and dust grain alignment $(\omega_{rad}/\omega_T)^2$ (*bottom row*), shown in the xz plane perpendicular to the mid plane (*left column*) and in the mid (xy) plane itself (*right column*). The grid of these simulations is made up of $N_{\rm r} \times N_\theta \times N_\varphi = 177 \times 181 \times 90$ cells.

R_{in}	R_{out}	Distance	a_{dust}	M_{dust}	R_*	T_*
1 AU	100 AU	100 pc	$[0.01, 1000]\,\mu$m	$10^{-6}\,M_\odot$	$2.5\,R_\odot$	$4000\,T_\odot$

Table 6.1.: Model parameters of the test case *sphere*.

on this model, distributions of temperature, anisotropy of the radiation field, and dust grain alignment has been computed (see Fig. 6.4). From the symmetry of the density distribution, a symmetry in temperature, radiative anisotropy, and grain alignment is expected. The numerical grid has been set up in the same way as in the simulations of protoplanetary disks in the following sections with $N_{\mathrm{r}} \times N_\theta \times N_\varphi = 177 \times 181 \times 90$ cells. The difference in the resolution in θ and φ directions creates a small but negligible deviation from exact symmetry. In the regions masked in Fig. 6.4 (*left column*), the simulations are not valid because of inaccuracies in the original MC3D. These regions are not relevant for the presented work, particularly in respect to protoplanetary disks, and fixing these issues was not a goal of the projects presented in this thesis. In the following, the results for each quantity, temperature, anisotropy, and grain alignment, is discussed separately.

The temperature distribution, T, of a spherical density distribution heated by a central star computed by MC3D behaves like expected. Close to the star where dust density and stellar radiation are maximized, the temperature reaches its maximum. Towards the model space boundaries, it is sloping radially. This behavior of the temperature distribution is found in both planes.

The anisotropy of the radiation field, γ_{rad}, is determined by the direction of photons and is computed per cell (see Eq. 6.4). In both planes, the anisotropy is minimal in the center of the sphere and raises radially. This is expected for the given model, since MC3D intrinsically neglects an interstellar radiation field. The most inner cells are the hottest. They are located close to the central star and emit a lot of photons, resulting in a low degree of anisotropy of the radiation field. At radii with decreasing temperatures, cells emit less photons and photons from the center of the model space are shielded by optical depth effects. In the boundary cells, the anisotropy of the radiation field is maximal. Due to the neglection of an interstellar radiation field, photons are only able to enter these cells from inside of the sphere. These cells do not carry any valid information. The anisotropy distribution in the xz plane does show a deviation from spherical symmetry along the z axis which is a boundary effect. Resulting from the inaccuracies in the masked regions, there are less photons entering the sphere at the boundaries of the masked region. This manifests itself in an increased anisotropy of the local radiation field. However, these regions are outside the domain of a protoplanetary disk and therefore, not relevant for the presented work.

The alignment of dust grains, $(\omega_{rad}/\omega_T)^2$, depends significantly on the ratio of temperature, energy density of the radiation field, and anisotropy of the radiation field, as well as on the local mass density (see Eq. 6.13). In general, $(\omega_{rad}/\omega_T)^2$ exceeds 10 throughout the sphere, resulting in an alignment of all grains in this test case. As expected for the given model, the value of $(\omega_{rad}/\omega_T)^2$ is maximal in the center of the sphere where temperature, energy density, and mass density are maximal. With increasing radial distance to the center, $(\omega_{rad}/\omega_T)^2$ decreases. The same boundary effects that have been described for the anisotropy in the paragraph above can be found for the grain alignment.

The simulations of this spherically symmetric test case illustrates the behavior and influences of the quantities involved in dust grain alignment simulations which cannot be tested analytically. A more sophisticated test, a benchmark test with the simulations of a protoplanetary disk published in CL07, is presented in the next section.

6.4.2. Benchmark test

The goal of this second part of this thesis has been to implement thermal polarization and dust grain alignment by radiative torques into MC3D based on the approach of Draine & Weingartner (1996) and CL07. In order to test this implementation, the results obtained with these new extensions of MC3D are compared to the results presented in CL07. It has to be noted that the evaluation can only be done qualitatively, since the work of CL07 is based on the model of Chiang et al. (2001), which is significantly different from the model of MC3D. Because of the partly substantial differences in fundamental assumptions (e.g., isothermality of the disk interior and neglection of the orientation of polarization vectors in SED simulations in the work of CL07) MC3D was not fully brought into conformity with regard to CL07. Yet, due to the lack of other work on thermal polarization simulations of aligned dust grains in protoplanetary disks, this method is the most suitable. The agreements found in the results of both MC3D and CL07 approve this approach. The differences between both underlying models and the results of the benchmark test as well as the limitations of the code are discussed in this section.

The differences of the underlying models

The results of radiative transfer simulations are, of course, sensitive to the applied model. Here, the differences between the basic assumptions of the models of CL07 and MC3D are described. Since the model used by MC3D has been described in Sect. 5.2.3 and 5.2.4, this section begins with the description of the model of CL07.

Figure 6.5 schematically shows the model used in CL07 which is motivated by the established model of Chiang et al. (2001). The disk is separated into differ-

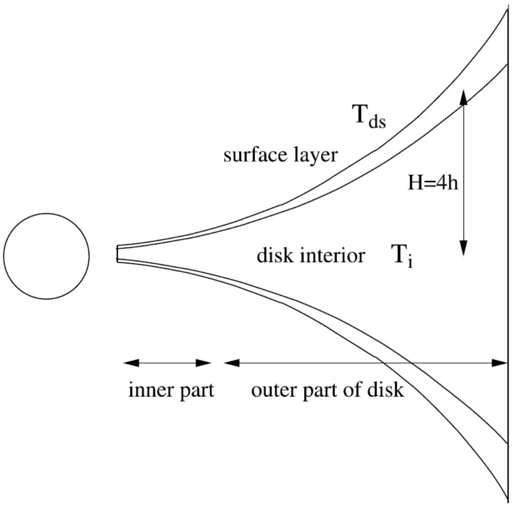

Fig. 6.5.: Disk model of CL07. The disk is separated in different sections: *The disk interior* consists of grains with a maximum size of $a_{\mathrm{max,i}} = 1000\,\mu\mathrm{m}$ and is isothermal. *The surface layer* is optically and geometrically thin, and contains of grains with $a_{\mathrm{max,ds}} = 1\,\mu\mathrm{m}$. Half of the dust emission of this layer immediately escapes, the other half enters the disk interior where it heats the dust. *The disk height H* is 4 times the disk scale height h. *The dust composition* changes with radial distance in both disk interior and surface layer (from CL07; reproduced with permission by AAS).

ent sections: disk interior, surface layer, as well as inner and outer region of the disk in radial direction. In each of these sections, the dust composition changes as described in the following. The disk interior contains dust grains with grain sizes $a_{\mathrm{i}} \in [0.1, 1000]\,\mu\mathrm{m}$, while the grain sizes in the surface layer are significantly smaller ($a_{\mathrm{ds}} \in [0.1, 1]\,\mu\mathrm{m}$). The grain size distributions in both sections of the disk follow the usual power-law $dN \propto a^{-3.5}\mathrm{d}a$. The central star radiates isotropically, and thus, heats the disk. The surface layer is geometrically and optically thin. CL07 assume that half of the thermal dust emission immediately escapes while the other half enters the disk interior which is then heated by both, the central star and the surface layer. In this model, the disk interior is isothermal. Furthermore, CL07 vary the dust composition with distance to the central star in both disk interior and surface layer. The grains in the surface layer are made of astronomical silicate only in the inner part of the disk ($r < 6\,\mathrm{AU}$), and astronomical silicate covered with water ice for $r > 6\,\mathrm{AU}$. In the disk interior the grains consist of astronomical silicate when $r < 0.8\,\mathrm{AU}$ and ice-silicate for $r > 0.8\,\mathrm{AU}$. The fractional thickness of the water ice mantle, $\Delta a/a$, is set to 0.4 in both disk interior and surface layer.

In both simulations, conducted with MC3D and by CL07, the magnetic field is assumed to be regular and toroidal, and both assume a flared disk structure. It is a common approach to assume layered disk models motivated by settling of large dust grains ($a \lesssim 1000\,\mu\mathrm{m}$) (e.g., Gräfe et al. 2013). However, in those cases the layer of large grains is much smaller with respect to the disk than it is the case for CL07. Therefore, the layered disk of CL07 is not considered as motivated by dust settlement. In that case, MC3D does not apply any layered design of the disk. Instead the given dust grains are distributed following the density distribution in Eq. (5.8) with $\alpha = 1.2, \beta = 1.14$ and with the same power-law for the grain size distribution as applied by CL07 (see Eq. 5.7). Additionally, the considered grain compositions are different. While CL07 consider only astronomical silicate, with and without water ice mantle, this thesis assumes the common mix of astronomical silicate and graphite but neglects ice (see Sect. 5.2.3). Furthermore, CL07 limit the radiation flux from the surface layer and the disk interior to a narrow spectrum around the wavelength $\sim 3000/T_{\mathrm{ds,i}}\,\mu$m, they limit the direction of the radiation flow within the disk to the vertical direction only, and they assume that the disk interior is isothermal. In opposition to this, MC3D computes the temperature distribution of the disk based on the Monte-Carlo radiative transfer method and assumes local thermodynamic equilibrium in each grid cell only. Additionally, MC3D takes the anisotropy of the radiation field into account (see Eq. 6.4). Both models do not consider effects of scattering during the computation of a SED or a map. Indeed, effects of scattering are less important in the sub-millimeter/millimeter wavelength regime.

The differences stemming from the deviations of these two models will result in different spectral energy distributions implicating different shapes of SEDs and intensities, polarized and unpolarized, traced in the spatially resolved maps. However, the qualitative behavior is comparable. Considering the very small number of simulations such as these, this is the best available testing method for this implementation.

Disk parameter			Dust parameter		Stellar parameter	
R_{in}	R_{out}	Distance	a_{dust}	M_{dust}	R_*	T_*
0.02 AU	100 AU	140 pc	$[0.01, 1000]\,\mu$m	$10^{-4}\,M_\odot$	$2.5\,R_\odot$	$4000\,T_\odot$

Table 6.2.: Initial parameters of the benchmark test.

The benchmark results

In order to compare both implementations to each other, a parameter setup of MC3D was chosen similar to the setup of parameters of CL07 (see Tab. 6.2). In the following, the grain alignment as well as the resulting spectral energy distributions and polarization maps are discussed. With these results, it is shown that the implementation of polarized dust emission of aligned grains has been successfully performed.

Grain alignment in disks. In Fig. 6.6, the dust grain alignment computed with MC3D is shown and compared to the results from CL07. Since CL07 discuss the surface layer ($a_{\mathrm{max}} = 1\,\mu$m) and the disk interior ($a_{\mathrm{max}} = 1000\,\mu$m) separately, two

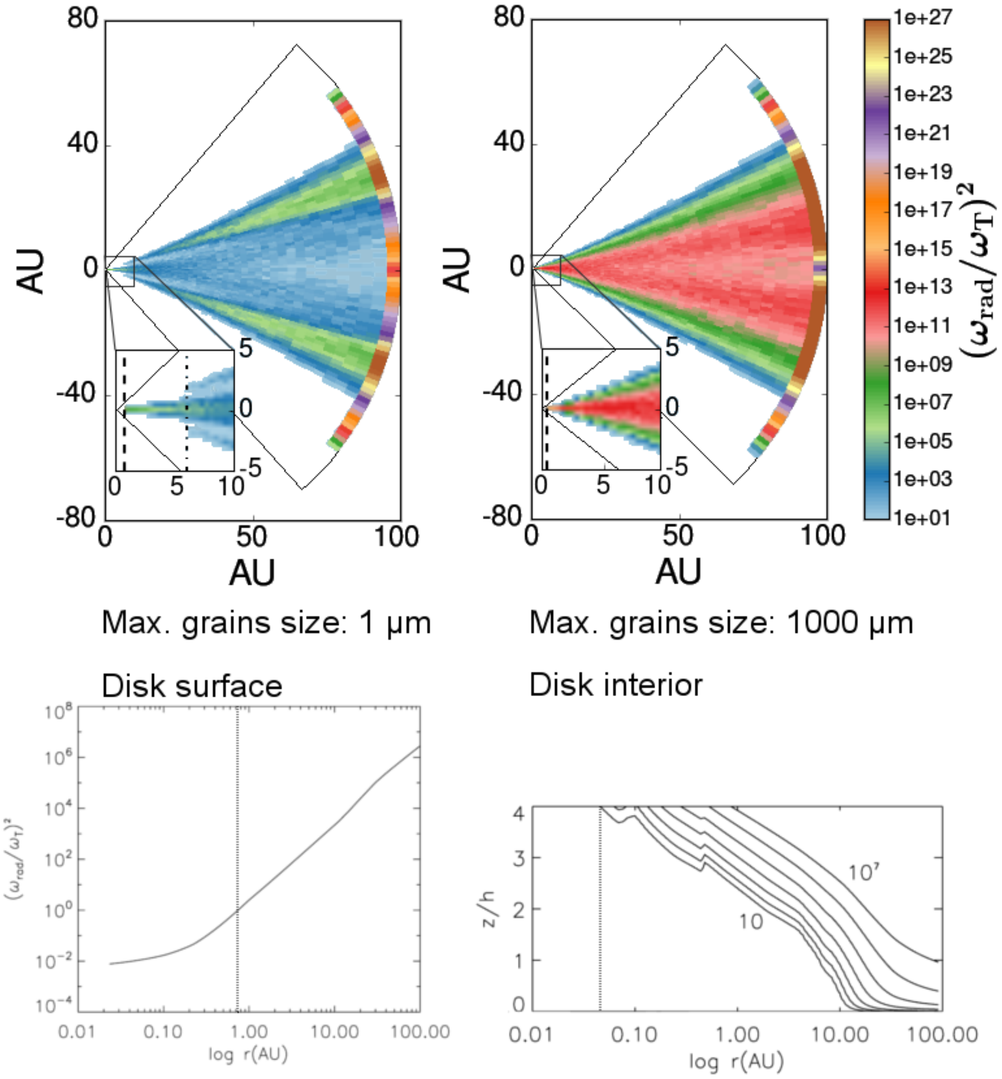

Max. grains size: 1 µm

Max. grains size: 1000 µm

Disk surface

Disk interior

Fig. 6.6.: Grain alignment in the disk computed with MC3D (*top:*, shown perpendicularly to the disk mid-plane) with maximal grain sizes of 1 μm *(top left)* and 1000 μm *(top right)*. The discontinuity in $(\omega_{\rm rad}/\omega_{\rm T})^2$ at the outer model space border (*black contours*) stems from the neglection of an interstellar radiation field. Small grains start to align close to the mid-plane at $r \geq 0.78$ AU (*dashed line*), at $r \geq 6$ AU (*dashed-dotted line*) grains also align towards the disk surface. Large grains with radii $\leq 1000\,\mu$m have only one initiation of grain alignment at $r = 0.08$ AU. *Bottom:* Grain alignment (reproduced from CL07, modified slightly for this thesis; reproduced with permission by AAS) in the surface layer *(bottom left)* starts at $r \gtrsim 0.7$ AU and in the disk interior $(\omega_{\rm rad}/\omega_{\rm T})^2$ (contour lines) exceeds 10 when $r \gtrsim 0.05$ AU (*bottom right*, the vertical disk height z is shown in units of the disk scale height h).

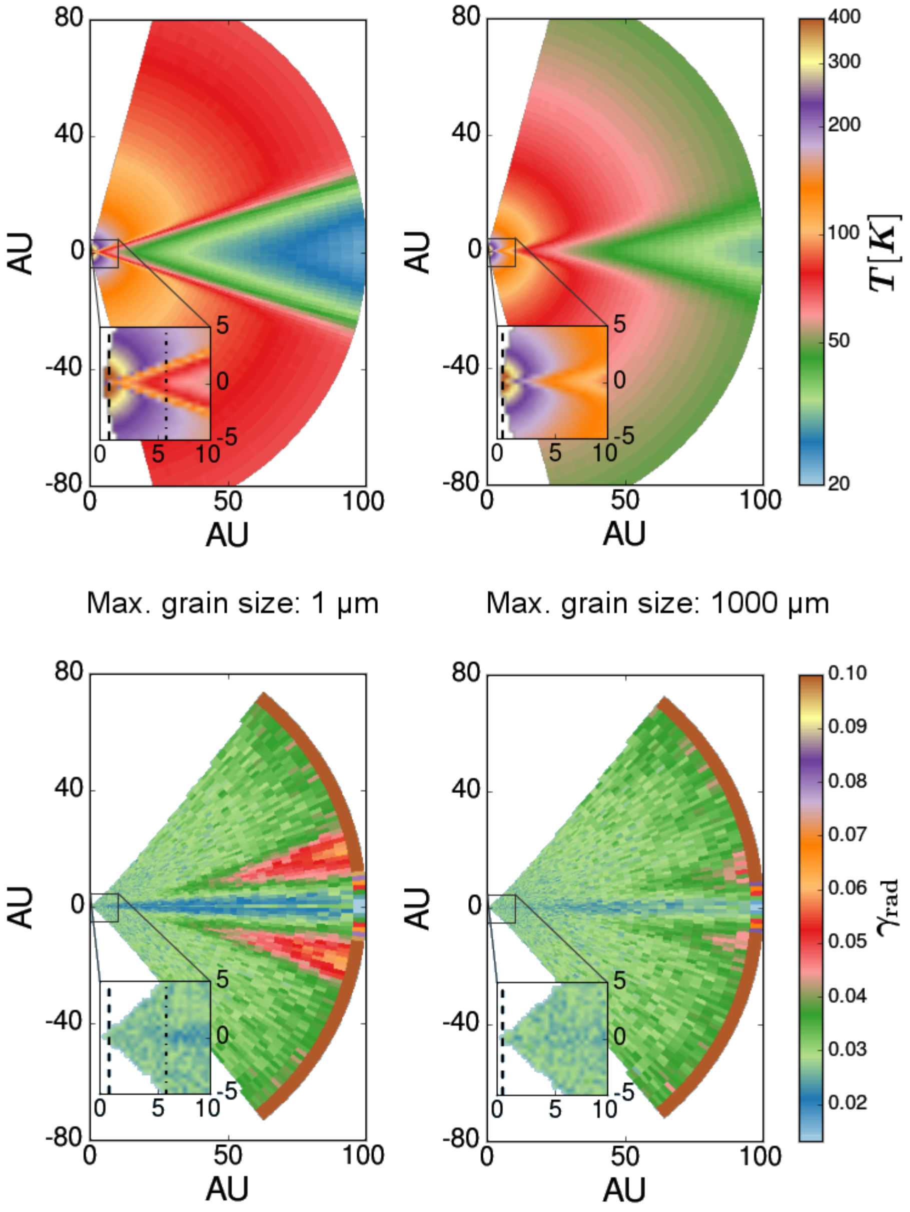

Fig. 6.7.: Temperature distribution and anisotropy of the radiation field in the disk. *Top:* The temperature distribution of the disk perpendicular to its mid-plane for $a_{\max} = 1\,\mu$m (*top left*) and $a_{\max} = 1000\,\mu$m (*top right*). *Bottom:* The anisotropy of the radiation field in the case of $a_{\max} = 1\,\mu$m (*bottom left*) and $a_{\max} = 1000\,\mu$m (*bottom right*). The different maximal grain sizes change the optical depth of the disk. The optical thick disk (*left*) shows sharp gradients in anisotropy and temperature, the optical thin(er) disk (*right*) shows much smoother gradients. While the smoother gradients lead to only one onset of grain alignment (dashed lines), the sharp gradients benefit the second jump in grain alignment (dashed-dotted line).

MC3D simulations with corresponding maximal grain sizes were computed. They demonstrate that the alignment of grains is dependent on the grain size. Small grains with radii $\leq 1\,\mu$m show two initialization steps of grain alignment, the first in the mid-plane of the disk at $r = 0.78\,$AU, the second towards the surface of the disk at $r = 6\,$AU. The first corresponds very well to the starting point of grain alignment in the simulations of CL07 which lies at $r \approx 0.7\,$AU. The grain alignment depends significantly on the ratio of temperature, energy density, and anisotropy of the radiation field, as well as on the local mass density (see Eq. 6.13). Small grains are very poor absorbers and emitters of radiation, thus, the disk with $a_{\max} \leq 1\,\mu$m is optically thick. As a result, temperature and anisotropy of the radiation field rapidly decrease with distance to the center of the disk. At the initial point of the dust grain alignment towards the surface of the disk, at $r = 6\,$AU, sharp gradients are present in the anisotropy of the radiation field and in the temperature distribution (see Fig. 6.7) resulting in $(\omega_{\rm rad}/\omega_{\rm T})^2$ which then exceeds 10 slightly.

Large grains with radii $\leq 1000\,\mu$m have only one initiation of grain alignment at $r = 0.08\,$AU what corresponds very well to the findings of CL07 who determined the initialization point for large grains in their disk interior to $r = 0.05\,$AU (see Fig. 6.6). Large grains are much more efficient in re-emitting the absorbed radiation. As a result, they cool down more efficiently, are optically thin(er) compared to small grains, and have much smoother gradients in temperature and anisotropy of the radiation field.

The discontinuity at the most outer cells in r direction is caused by the neglection of the interstellar radiation field in MC3D, they do not carry any valid information.

Spectral energy distribution. The second quantity of this benchmark test is the spectral energy distribution (see Fig. 6.8). CL07 plot the SEDs of the total emission and the polarized emission for each component of their model as well as the SED of the total emission. This includes the central star which is not part of the MC3D simulations of dust emission. The SEDs of both models show an emission peak around $10\,\mu$m which is the characteristic peak of silicate (Draine & Lee 1984). Additionally to this, the SED of CL07 shows a second and third peak at $40\,\mu$m and $60\,\mu$m caused by the water ice mantle of the grains in their model. CL07 used oblate dust grains with an axis ratio of 1:1.5, which results in slightly smaller polarization degrees compared the MC3D simulations. More importantly, CL07 ignored the orientation of polarization vectors in their calculations of the SEDs. The observed polarization degree is very sensitive to the orientation of polarization vectors, especially in the case of aligned dust grains. The new features of MC3D consider this effect. With a disk inclination of $i = 10°$, a good agreement with the calculations of CL07 was found by comparison of the behavior of the total emission relative to the polarized emission in both studies. As expected from the optical properties with respect to the wavelength, large dust grains dominate the emission spectrum at long wavelengths.

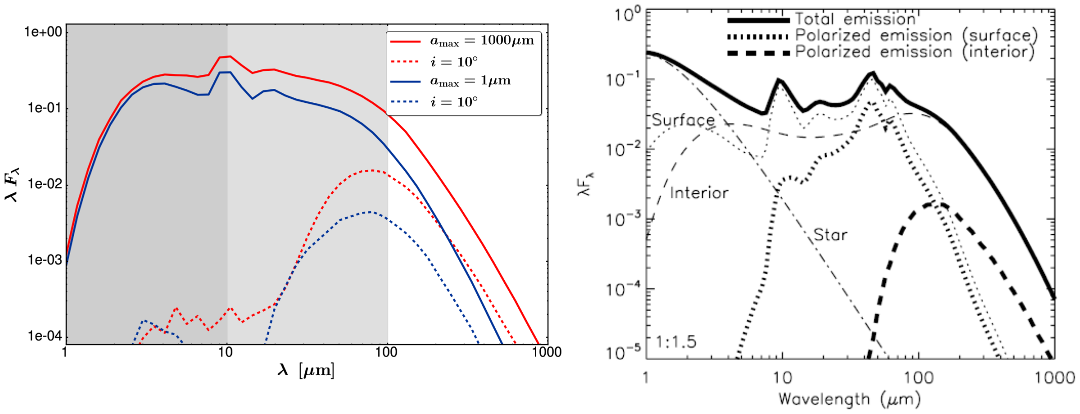

Fig. 6.8.: SPECTRAL ENERGY DISTRIBUTION. The vertical axis (λF_λ) is in arbitrary units. *Left:* Results for oblate grains with axis ratio 1:2. Total emission of model with $a_{\max} = 1\,\mu$m (*blue solid line*), polarized emission for $a_{\max} = 1\,\mu$m (*blue dashed line*) both at disk inclination of $i = 10°$, total emission of model with $a_{\max} = 1000\,\mu$m (*red solid line*), polarized emission for $a_{\max} = 1000\,\mu$m (*red dashed line*) both at disk inclination of $i = 10°$. The shaded region marks the wavelength range dominated by scattering for grains with $a_{\max} = 1\,\mu$m (*dark gray*) and $a_{\max} = 1000\,\mu$m (*light gray*). *Right:* Result for oblate grains with axis ratio 1:1.5 (from CL07; reproduced with permission by AAS). Total emission (disk interior + surface layer; *thick solid line*), total emission from surface layer (*thin dotted line*), polarized emission from surface layer (*thick dotted line*), total emission from disk interior (*thin dashed line*), polarized emission from disk interior (*thick dashed line*). Note that CL07 ignored the direction of polarization vectors for these calculations.

This is seen in the total emission and the polarized emission in both models. CL07 and this work are neglecting scattering effects. Since scattering dominates the signal on a wavelength range $\lesssim 100\,\mu$m for large, respectively $\lesssim 10\,\mu$m for small maximal grain sizes, these purely thermally polarized simulations are of significance only on wavelengths $\gtrsim 100\,\mu$m, respectively $\gtrsim 10\,\mu$m. With respect to the model differences, the relative behavior of total to polarized emission of both grain size distributions of CL07 and this thesis fit well to each other.

Polarization maps. Figure 6.9 shows the polarization maps computed with MC3D and from CL07. MC3D is configured to present polarization maps always as a composition of the total emission map over-plotted with polarization vectors, while CL07 limit their maps to polarization vectors. All maps presented in Fig. 6.9 show simulated observations at a wavelength of 850 μm at two different disk inclinations of 10° and 60°. Here again, the polarization degree computed by MC3D is higher than in the results of CL07. The maps display the characteristic polarization pattern of an underlying toroidal magnetic field structure. At an nearly face-on inclination of

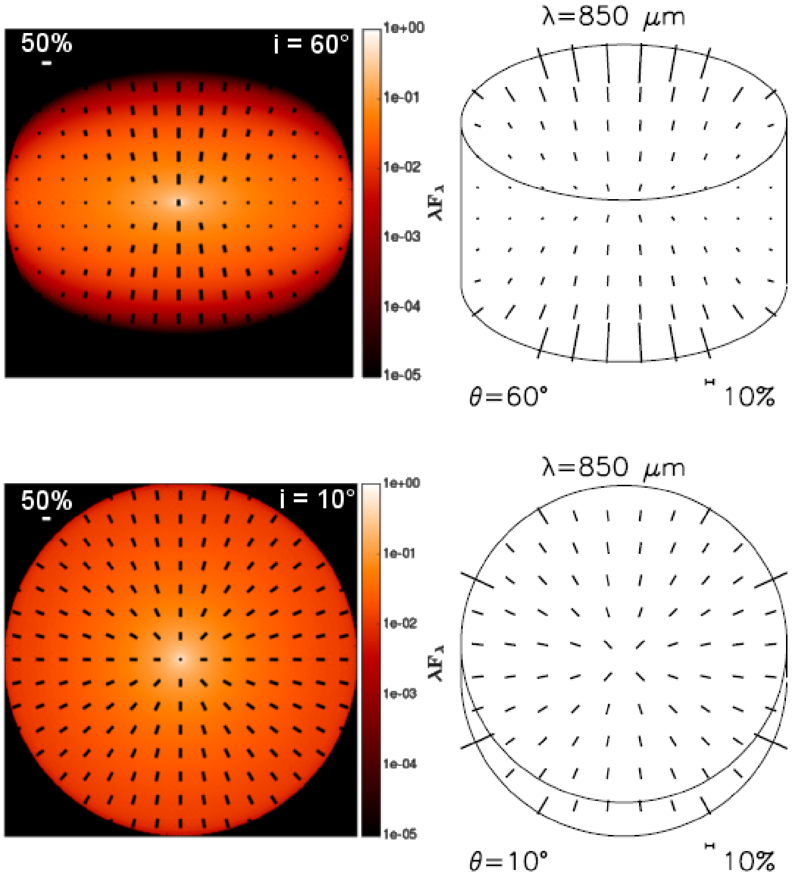

Fig. 6.9.: Polarization maps, *left:* computed with MC3D, showing total intensities in arbitrary units over-plotted by polarization vectors at a wavelength of 850 μm and disk inclinations of $i = 60°$ ($a_{\mathrm{max}} = 1000\,\mu$m, *top left*) and $i = 10°$ (*bottom left*). *Right:* Thermal polarization maps from CL07 (reproduced with permission by AAS) at a wavelength of 850 μm of the emission of disk interior + surface layer at two disk inclinations $\theta = 60°$ (*top left*) and $\theta = 10°$ (*bottom left*).

$i = 10°$, the radially symmetric pattern is clearly visible in both simulations and the polarization degree is constant as expected. Only four vectors in the maps of CL07 show an increase in polarization degree what is caused by boundary effects. In the more inclined maps ($i = 60°$), the radial polarization pattern converts into a rather hourglass-shaped structure which results from the projection effect along the line-of-sight and is found in both maps. The same also applies to the degree of polarization. Close to the vertical symmetry axis, the polarization signal is the strongest and drops only slowly towards the center of the disk. Along the horizontal symmetry axis of the disk, the polarization signal is canceled out almost completely due to projection effects. Only with increasing distance to this axis, the polarization signal becomes stronger again. This behavior is found in both simulations, computed with MC3D and by CL07.

6.4.3. Limitations of this implementation

Although, as pointed out above, the polarization of dust emission of aligned dust grains has been implemented successfully, there are limitations to these simulations that are discussed here. Two minor issues lie in the approaches for determination of polarization and grain alignment. The implementation of polarization is based on the assumption of a razor-thin dust grain which polarizes light between $P = 0\%$ (face-on) and $P = 100\%$ (edge-on). However, the behavior of the change in polarization degree is not affected by this approach and the effective polarization degree can be adapted to any grain shape by adapting the maximal polarization degree possible to the given grain shape. The alignment of the grains, on the other hand, assumes that all grains within the current cell are aligned perfectly as soon as $(\omega_{\mathrm{rad}}/\omega_{\mathrm{T}})^2 > 10$. This neglects the possibility of varying degrees of grain alignment. Since this pioneering code is a first step towards treating full radiative transfer of polarized emission of aligned non-spherical dust grains, this simplifying assumption is used.

Additionally to this, there is the handling of grain asphericity, respectively the scattering on non-spherical particles. As described in Sect. 6.1, for the implementation of non-spherical dust grains into MC3D it was necessary to work with a hybrid approach for the model of grain shapes. During the Monte Carlo radiative transfer simulations, i.e., the calculations of temperature distributions and anisotropy of the radiation field, scattering effects are indispensable. Scattering on spherical grain shapes is relatively easy to handle numerically and is the basis of the radiative transfer of MC3D and many other codes. However, scattering on non-spherical grain shapes is still an issue for both, the mathematical description and the numerical implementation. For that reason, MC3D processes the photons through the model space assuming spherical grain shapes while it calculates dust temperature distributions and anisotropy of the radiation field, and skips to non-spherical grains for calculating the polarization state (performed in an additional run of the code). Here, the scattering is neglected, and thus, the significance of these simulations is limited to long wavelengths where scattering effects play only a tangential role for observations of protoplanetary disks. However, this code is one of the first of its kind and already opens unprecedented possibilities to investigate the effects of polarized dust emission and grain alignment in protoplanetary disks. A discussion of the applications of this code is presented in the next section.

6.5. Applications

Observations of polarized sub-millimeter radiation from T-Tauri disks enable us to study their magnetic fields. Motivated by this, the 3D radiative transfer code

MC3D was extended by polarized emission of aligned non-spherical dust grains in the context of this thesis. These polarized radiative transfer simulations aim at modeling, characterizing, and explaining polarimetric observations of T-Tauri disks. This code is able to model polarized spectral energy distributions and spatially resolved polarization maps of the thermal dust emission of circumstellar disks. In this section, applications of these new features of MC3D are discussed.

6.5.1. Spectro-polarimetry of protoplanetary disks

If a protoplanetary disk cannot be spatially resolved, it is still possible to derive properties of the disk from observations by determining its spectral energy distribution. In an SED, the spatial information is abandoned in favor of the spectral information. If these observations are conducted polarimetricly, this is termed spectro-polarimetry. Since polarimetry is very sensitive to projection effects along the LOS, the loss of the spatial resolution will show effects on the resulting signal. Because of the radial symmetry of the polarization pattern stemming from a toroidal magnetic field structure if the disk is face-on oriented to the observer, the polarized signal will be extinguished. Thus, the disk inclination can be derived from such observations. Furthermore, SEDs are commonly used to derive the dust properties of an object by fitting radiative transfer models to the observed SED, and to classify the evolutionary stage of the object (see Sect. 2.2).

In this section, the effect of polarization on SEDs is shown for a toy model (Sect. 6.5.1.1) as well as for a model of a protoplanetary disk (Sect. 6.5.1.2).

6.5.1.1. The toy model: A sphere

The most simple case for spectro-polarimetry that can be analyzed with this code is a spherical dust distribution, $\rho_{\mathrm{dust}}(r)$, containing a homogenous magnetic field $\vec{B}$,

$$\rho_{\mathrm{dust}}(r) = r^{-1}, \qquad \vec{B} = \vec{e}_{\mathrm{z}}, \tag{6.20}$$

where $\vec{e}_{\mathrm{z}}$ is the unit vector in z-direction. With the goal of demonstrating the influence of the inclination of the disk on the SED in a comprehensible example, simulations of this setup were conducted at different inclinations i (see Fig. 6.10). To restrict the analysis only to effects of inclination, all dust grains are perfectly aligned to the magnetic field. The total emission of this model is independent of the inclination. However, by changing the inclination from an edge-on position to a face-on position relative to the non-spherical dust grain, the polarization degree changes. The polarization degree is maximal ($P = 100\%$ in the case of a razor-thin grain) at the edge-on position ($i = 90°$), drops to $P = 33\%$ at an inclination of

$i = 45°$, and at the face-on position ($i = 0°$) the polarization degree disappears ($P = 0\%$). Thus, by determining the spectral energy distribution of the polarized dust emission, the inclination of the object can be derived from the SED. Of course, this is just a very simple toy model. A model of a protoplanetary disk is discussed in the next section.

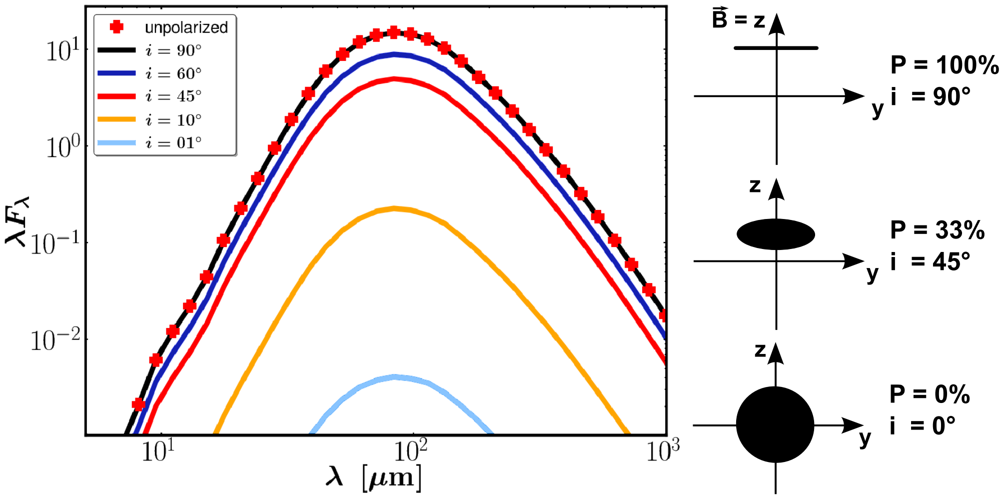

Fig. 6.10.: Spectro-polarimetry of a sphere containing a homogenous magnetic field. The effect of inclination is clearly identifiable in the SED of the polarized emission. At an inclination $i = 90°$ the observer looks directly at the edge of all dust grains, thus the emission increases to its maximum ($P = 100\%$, assuming razor-thin dust grains). By changing inclination towards a face-on observation of the dust grains, the polarization degree drops to $P = 33\%$ at $i = 45°$ and becomes $P = 0\%$ at the face-on position where $i = 0°$.

6.5.1.2. The protoplanetary disk

As mentioned before, SEDs are commonly used to determine properties of the protoplanetary disk such as the evolutionary stage of the disk (see Sect. 2.2), the disk orientation, and the dust properties of the disk. Examining if it is possible to derive disk properties with spectro-polarimetry additionally to the usual measurements of the total intensity across the spectrum has been part of this thesis. For this reason, SEDs of the polarized emission of aligned non-spherical dust grains in a protoplanetary disk have been computed. In Figure 6.11, the SEDs are shown for two cases, small dust grains with $a_{\max} = 1\,\mu$m and large grains with $a_{\max} = 1000\,\mu$m. Obviously, the larger grains are more dominant at longer wavelengths than small grains. This originates from the lower temperatures of small grains as well as the fact that large grains emit more efficiently at those wavelengths. The characteristic $10\,\mu$m silicate feature is clearly seen in all SEDs. The disk with small grains is op-

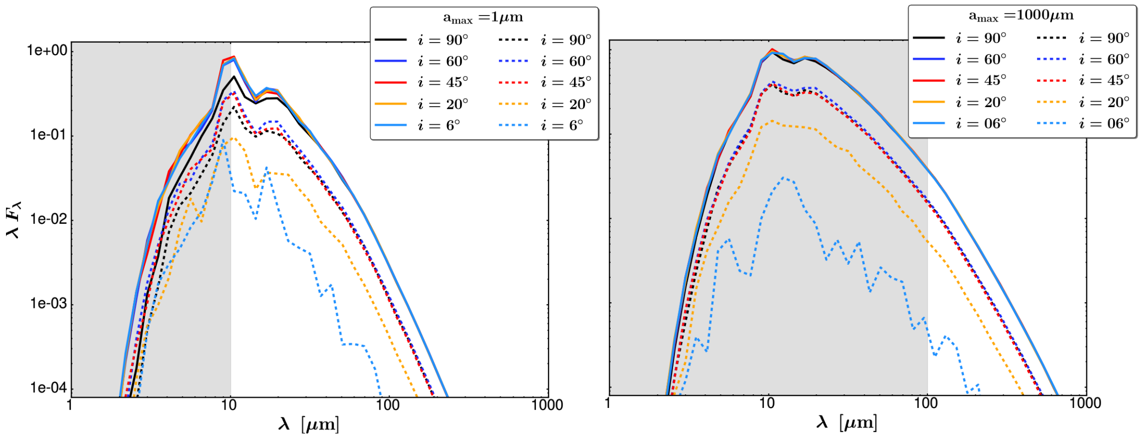

Fig. 6.11.: Spectro-polarimetry of a protoplanetary disk containing a toroidal magnetic field, computed for a maximal dust grain size of 1 μm (*left*) and 1000 μm (*right*). The total (unpolarized) emission is shown in *solid lines*, the polarized emission in *dashed lines* both at different inclinations i, the intensity (λF_λ) is in arbitrary units. Note that the solid lines are overlapping each other most of the time. The scattering dominated part of the spectrum is shaded gray.

tically thick which results in a lower total emissivity at high inclinations ($i \approx 90°$). On the other hand, the disk with large grains is optically thin, thus its SEDs at different inclination angles are indifferent in total emission. It is prominent that the SEDs in polarized light are indistinguishable for high inclinations ($i \gtrsim 45°$) in both cases, small and large grains. In these cases, the polarization pattern observed at high inclinations is dominated by parallel polarization vectors. The parallel polarization patterns vary in the outer disk regions towards the mid-plane in the polarization degree (see Fig. 6.12), but this is only a minor effect seen in the spatially unresolved SED compared to the cancellation of radial symmetric polarization patterns. A significant drop in the amplitude of the SEDs is found for lower inclinations ($i < 45°$). As it is expected from the radial symmetric polarization pattern corresponding to a toroidal magnetic field structure, the signal tends to vanish with very small inclinations, the polarized SED at $i = 6°$ is already noise dominated in both cases.

As shown here, both the inclination of the disk and the dust properties (grain sizes and chemical composition of the dust) affect the SED in polarized light as well. These simulations show that it is possible to distinguish between different models of protoplanetary disks and magnetic fields therein by taking into account not only the SED in the unpolarized light but also the polarization information that is carried by the radiation. Observations of the polarized thermal dust emission in the (sub-)mm wavelength range with, e.g., PolKa/APEX (Wiesemeyer et al. 2014), PLANCK (European Space AGENCY (ESA) 2000), CARMA (Hull & Plambeck

2015) and SCUBA2-POL/JCMT (Holland et al. 2013; available from 2016/2017), will benefit from this analysis tool.

6.5.2. Magnetic fields in protoplanetary disks traced with polarization maps of aligned non-spherical dust grains

With ALMA it is now possible to spatially resolve protoplanetary disks and measure their polarized dust emission for the first time. Thus, spatially resolved radiative transfer simulations of the polarized dust emission are necessary to analyze such observations. In this section, two examples for radiative transfer simulations of the spatially resolved polarized dust emission are presented. The first example is based on the standard approach of radiative transfer, the analytical approach for the dust density distribution and the magnetic field (Sect. 6.5.2.1). A new development in radiative transfer that came up with recent observations of large asymmetries in the dust density distribution of protoplanetary disks and the gain in computational power, is the coupling of radiative transfer simulations to magnetohydrodynamic simulations. An example for radiative transfer simulations based on this approach is presented in Sect. 6.5.2.2.

6.5.2.1. Spatially resolved polarization maps

The standard approach in radiative transfer simulations is to set up the model parameters (e.g., dust density distribution, magnetic field structure) analytically and, if necessary, adapt the parameters to fit observational results. Then, based on these analytical approaches, spatially resolved maps are computed. Figure 6.12 shows such simulations of spatially resolved observations of polarized radiation of a protoplanetary disk. The underlying magnetic field structure is toroidal and the dust grain alignment is computed as described in Eq. (6.13).

Figure 6.12 displays the polarization maps of a protoplanetary disk at three different inclinations ($i = 90°$, $60°$, $1°$). In the edge-on case ($i = 90°$), the polarization vectors are strictly parallel and only deviating in length. The polarization angle, the vector orientation, indicates a homogenous field structure but the polarization degree, the vector length, implies a twist in the orientation of aligned dust grains caused by the toroidal field structure. However, without the knowledge of the underlying magnetic field structure, the drop in the polarization degree may be as well interpreted as a lack of order in the magnetic field structure, and thus, an insufficiently strong magnetic field influence in this region. At an inclination of $i = 60°$, the polarization vectors remain constant along the vertical symmetry axis of the disk, but change in length and direction with increasing distance to that symmetry axis. Towards the horizontal symmetry axis of the disk, the polarization degree drops to zero. The characteristic polarization pattern of a toroidal magnetic field in an edge-on observation is still recognizable, yet, the first indications of a radial variance are there as well. Finally, in the face-on case, the polarization degree is maximal since the dust grains are aligned in an edge-on position to the observer. The polarization pattern shows the characteristic radial polarization structure of a purely toroidal magnetic field as well as the drop of the polarization degree towards the center of the disk. The observations of edge-on oriented disks are the ideal case for identifying this radial symmetric magnetic field structure. It is obvious that spatially unresolved observations of such structures would lead to a non-detection because of the radial symmetry of the polarization pattern. In unresolved face-on observations of a protoplanetary disk, the polarization states of the waves emitted from different points in that disk will cancel each other out. Therefore, the spatial resolution is essential for polarization observations of protoplanetary disks performed with the polarization modes of , e.g., ALMA. These simulations can be used to derive physical parameters from observations of polarized dust emission, or to predict observational results, by adaption of the parameters of the underlying disk, dust, and magnetic field model of these simulations.

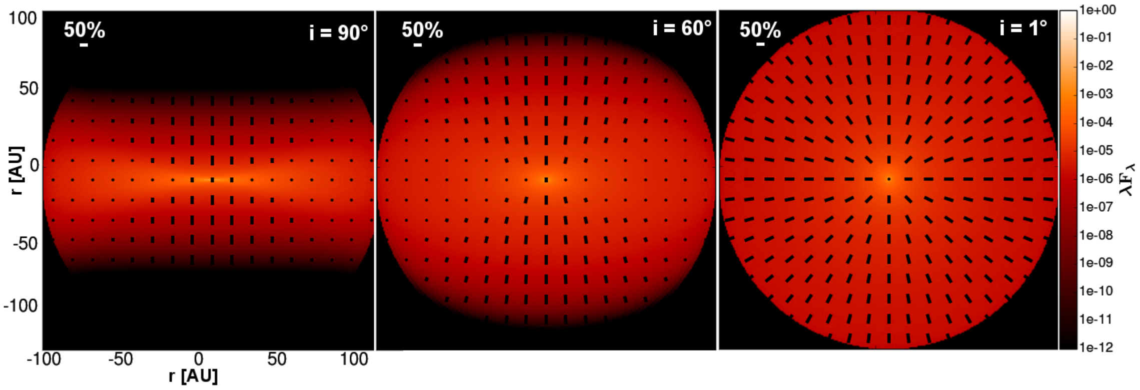

Fig. 6.12.: SPATIALLY RESOLVED POLARIZATION MAPS of the dust emission at 850 μm of protoplanetary disks at three different inclinations. The total intensity (color map in arbitrary units) is over-plotted with polarization vectors that show the polarization degree (vector length) and polarization angle (vector orientation) of the signal. Each vector represents the signal binned over 15 × 15 px. The underlying magnetic field structure is toroidal. *Left:* The edge-on case, $i = 90°$; *middle:* an inclination of $i = 60°$; *right:* the face-on case. It is obvious that spatially unresolved observations of such structures would lead to a non-detection. Thus, the spatially resolution is essentially for polarization observations of protoplanetary disks.

6.5.2.2. 3D MHD + RT in polarized light

Observations with ALMA are able, for the first time, to resolve the detailed structure of protoplanetary disks in the thermal dust emission. Recently, a number of observations showed large asymmetries in the dust density distribution, for instance, in the protoplanetary disks HD142527 (Casassus et al. 2013), SAO206462 and SR21 (Pérez et al. 2014). Such observational results are the motivation to further use not only analytical approaches for the dust density distribution and the magnetic field, but to couple radiative transfer simulations with the results of magnetohydrodynamic (MHD) simulations. At the same time, this finally enables the comparison of MHD results with observations.

The example presented in this section is based on non-ideal global MHD stratified simulations of protoplanetary disks computed with the FARGO MHD code PLUTO (Mignone et al. 2007, 2012) published in the work of Flock et al. (2015). These MHD simulations take the stellar and disk parameters from a parametrized disk model applied to fitting high-angular resolution multi-wavelength observations of various circumstellar disks (see Tab. 6.3 and Fig. 6.13). Flock et al. (2015) present two models, with different dust-to-gas mass ratios of 10^{-2} (model D2G_e-2) and 10^{-4} (model D2G_e-4). The deviations in the setup result in significantly different structures, both in the density distribution and the magnetic field (see Fig. 6.14, Fig. 6.15).

Model name	$N_\mathrm{r} \times N_\theta \times N_\varphi$	$\Delta r_\mathrm{AU} : \Delta\theta_\mathrm{rad} : \Delta\varphi_\mathrm{rad}$	D2G	Inner orbits
D2G_e-2	$256 \times 128 \times 512$	$20 - 100 : 0.72 : 2\pi$	10^{-2}	350
D2G_e-4	$256 \times 128 \times 512$	$20 - 100 : 0.72 : 2\pi$	10^{-4}	800
Disk parameter		Stellar parameter		
$M_\mathrm{total} \cong 0.085 M_*$	$\Sigma_0 = 5.94 \mathrm{g\,cm}^2 \, \frac{100\,\mathrm{AU}}{R}$	$T_* = 4000\,\mathrm{K}$	$0.95\,\mathrm{L}_\odot$	$M_* = 0.5\,\mathrm{M}_\odot$

Table 6.3.: Initial parameters of the MHD simulations (from Flock et al. 2015).

The questions arising from these MHD results are: Can these magnetic field structures actually be traced? How can the differences between these models be detected to determine the physics taking place in a certain observational object? This part of this thesis focuses on the aspect of observations of the polarized dust emission; the discussion of the density structure is covered by the work of Flock et al. (2015).

MC3D was prepared to take both the dust density distribution as well as the magnetic field as input parameters as they result from these MHD simulations (see Fig. 6.14, Fig. 6.15). The dust temperature distribution as well as the polarization maps of the dust emission are computed by applying MC3D to the MHD results. For computational reasons, it is assumed that the dust grains are perfectly aligned by the magnetic field. The resulting polarization maps are discussed in the following. For clarity, the model names D2G_e-2 and D2G_e-4, have been kept unchanged in order to compare to the MHD simulations. However, note that the models in Flock et al. (2015) are discussed sometimes at a different number of inner orbits, i.e., different computing time steps.

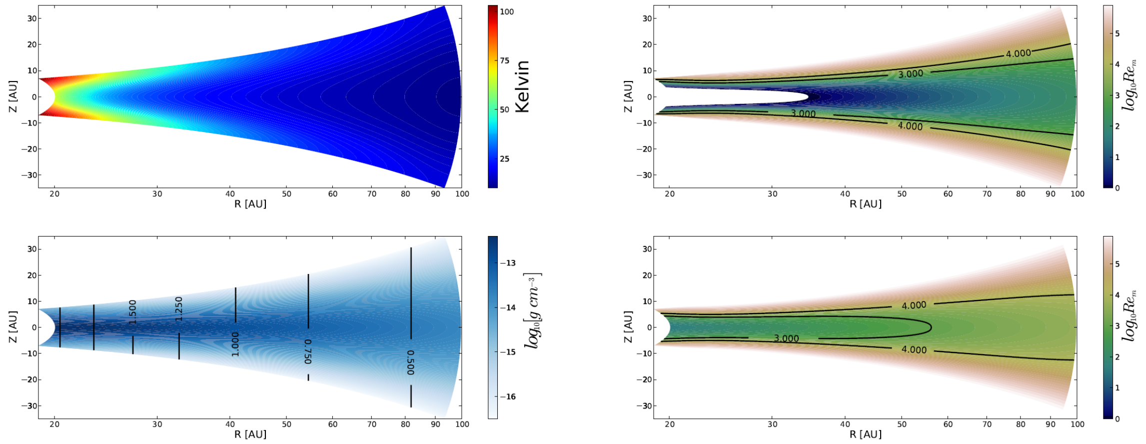

Fig. 6.13.: INITIAL PARAMETERS FOR MHD SIMULATIONS: Temperature distribution (*top left*), density distribution (*bottom left*), with black contour lines showing the strength of the initial vertical magnetic field in mG. Initial resistivity profile with a dust-to-gas mass ratio of 10^{-2} (*top right*) and 10^{-4} (*bottom right*), with contour lines showing the magnetic Reynolds number (from Flock et al. 2015; reproduced with permission © ESO).

The first glance on the polarization maps of both models, D2G_e-2 and D2G_e-4, reveals that both are characterized by the dominating toroidal structure of the magnetic field (see Fig. 6.16, *top row*). Model D2G_e-2 shows a gap in the dust density structure resulting from magneto-rotational instability (MRI). In the case of non-self-gravitating disks, such as protoplanetary disks, axisymmetric bumps in the surface density may occur and trigger Rossby Wave Instability (RWI) decreasing the surface gas density in the bump. At the same time, MRI within and out of the gap region increases the surface gas density in the bump again. MRI occurring in higher disk layers generates a small amount of accretion within gap and bump limiting the amount of matter inside the gap. Nevertheless, the magnetic field is dominated by its toroidal component, also inside the density gap (see Fig. 6.14) which results in a radially symmetric polarization pattern that does not trace the density gap. Towards the center of the disk, the polarization pattern becomes twisted by tracing the slight twist in the magnetic field structure caused by angular momentum conservation. Model D2G_e-4, on the contrary, shows a strong vortex traced in both in the total (unpolarized) dust emission and in the polarized signal. In the center of the vortex, where the dust emits the strongest and the vortex structure is ordered across a larger region, the polarization signal is the strongest, yet it is reduced compared to regions outside the vortex. Here, the polarization vectors trace the large-scale structure of the vortex. In this region, the magnetic field shows poloidal components, as well. Towards the outer regions of the vortex, left and right from its center, the structures become turbulent on smaller scales and the magnetic field becomes poloidal (see Fig. 6.14). Thus, the projected polarization along the line of sight extinguishes.

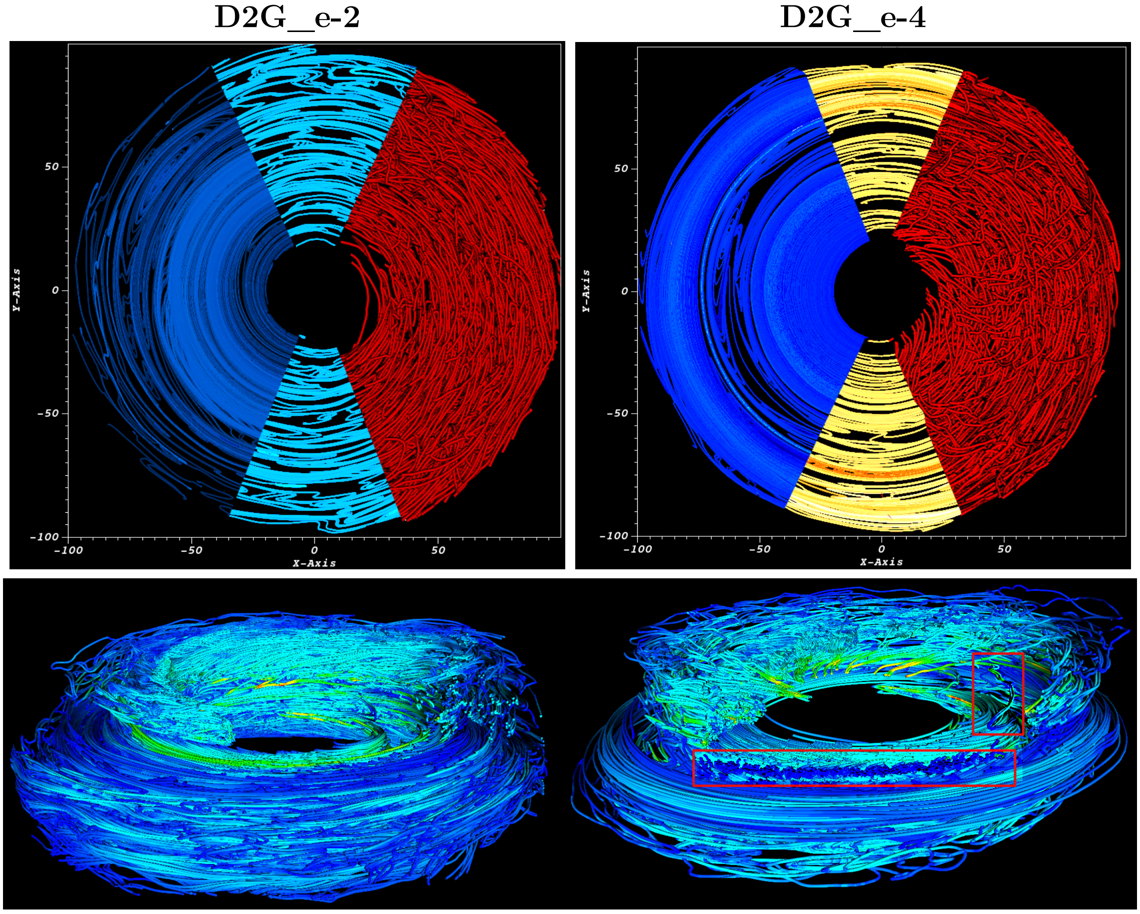

Fig. 6.14.: Magnetic field lines resulting from the MHD simulations of Flock et al. (2015). *Top:* cutaway face-on view of the magnetic field lines of D2G_e-2 (*left*) and D2G_e-4 (*right*), mid-plane (dark blue), half disk height (cyan / yellow), complete 3D view of the magnetic field lines in the disk (red). *Bottom:* Inclined cutaway view on the magnetic field lines of D2G_e-2 (*left*) and D2G_e-4 (*right*). While the magnetic field structure of D2G_e-2 is mainly toroidal, D2G_e-4 shows poloidal magnetic field components (red boxes) that are found in the slide cuts (*top panels*) as blank regions. [These images were produced with the visualizing tool VisIT (Childs et al. 2012).]

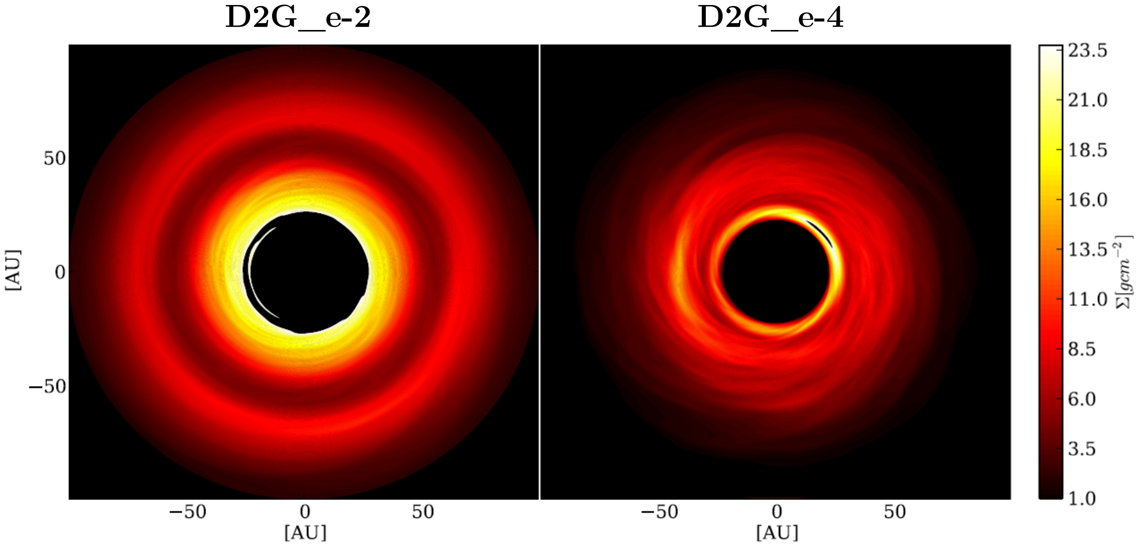

Fig. 6.15.: Surface density maps resulting from the MHD simulations of Flock et al. (2015). *Left:* model D2G_e-2, *right:* model D2G_e-4. While the dust density gap is clearly seen in the D2G_e-2 model, the most prominent characteristic of the D2G_e-4 model is the vortex that appears as density enhancement in these maps (from Flock et al. 2015; reproduced with permission © ESO).

The magnetic field structure as well as the MRI-induced vortex can be derived from and distinguished by simulated observations of polarized dust emission computed with MC3D. However, these simulations do not include the instrumental influence on the observed signal. The interesting effects and structures in protoplanetary disks can be found on scales of a few AU in disks with typical distances of $50 - 140$ pc, corresponding to the necessity to resolve sub-arcsecond scales. The spatial resolution of these observations is crucial to reveal the magnetic field structure, or even to detect a polarization signal in a protoplanetary disk. In the case of a polarization pattern as in Fig. 6.16, the measured signal would be canceled out in an unresolved observation, especially in a disk observed face-on. These scales can be resolved with the unprecedented sensitivity and resolution of ALMA. In contrast to single-dish telescopes, the instrumental effects of interferometers like ALMA cannot be taken into account by simple convolution of the simulated data with an artificial telescope beam. For this reason, the Common Astronomy Software Applications (CASA *v4.2*; CASA Group 2014) package was applied. CASA is a software package to reduce and analyze observational data as well as data of simulated observations. It is specialized for a number of different interferometers, including ALMA. The CASA simulations are based on a set of specifications such as the configuration of the ALMA antennae, the wavelength of observation, and the considered noise sources. These specifications were chosen to fit well for a planned observation of the

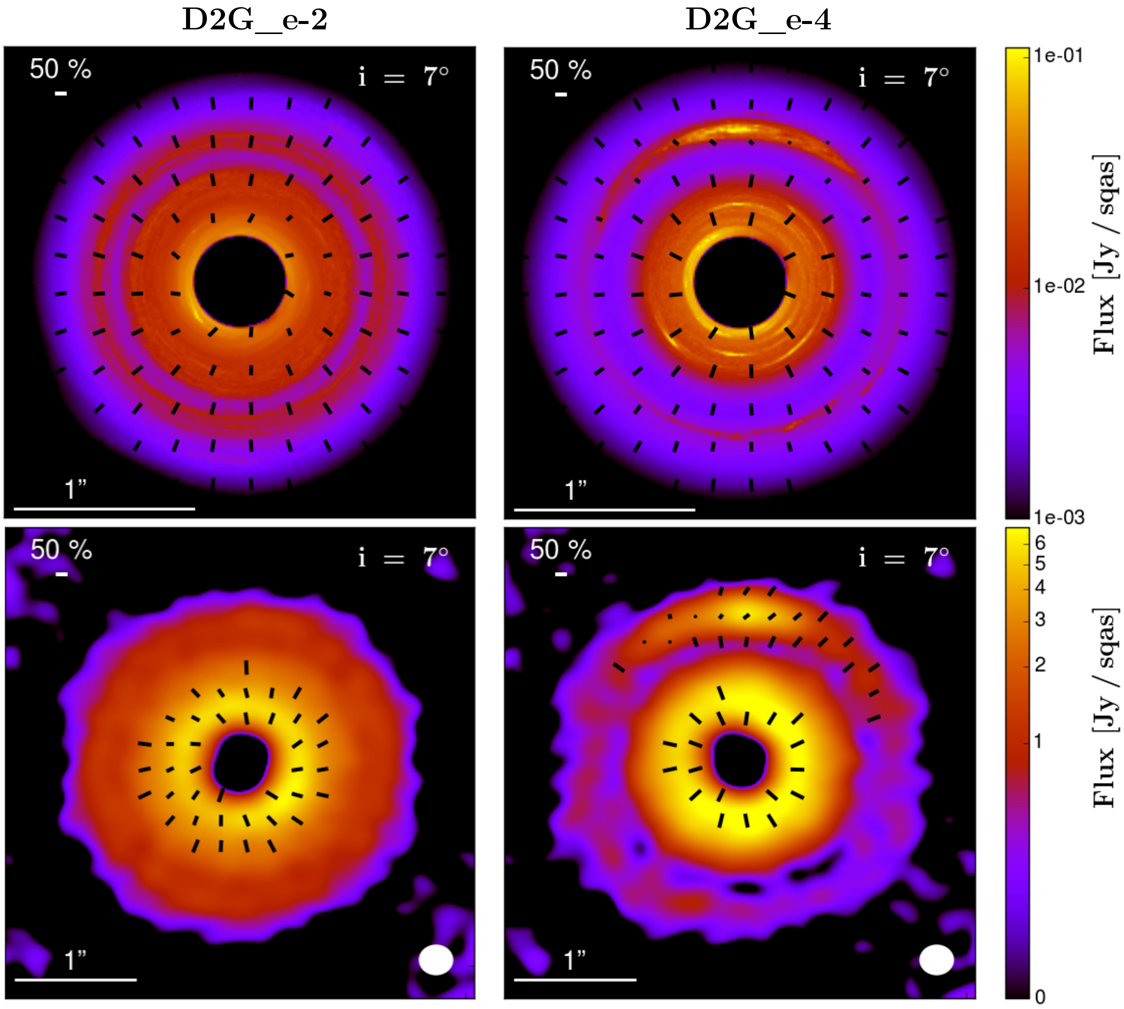

Fig. 6.16.: Upper panels: 3D radiative transfer simulations of polarized thermal dust emission with underlying magnetohydrodynamic simulations (Flock et al. 2015). The continuum emission (color-map) is over-plotted by polarization vectors (*left*: model D2G_e-2 showing an MRI induced gap; *right*: turbulent model, D2G_e-4, showing a vortex clearly seen in both, continuum and thermal polarization). Lower panels: Simulated ALMA observations of these maps at 230GHz using the ALMA configuration C36-5 (including thermal noise; CASA *v4.2*). The data is binned over the beam size (see white ellipse in the lower panels) to create the polarization vectors. Here, it is assumed that the dust grains are aligned perfectly with the magnetic field.

T Tauri disk TW Hya. The proposal was submitted in April 2015 for the ALMA Cycle 3 call for proposals (PI: Bertrang; status pending). The results of the coupled MHD + RT + CASA simulations are shown in Fig. 6.16 (*lower panels*). Most importantly, there is a detectable polarization pattern which is limited to the brightest regions of the disk for both models. The limit to the brightest regions stems from the sensitivity limit in conjunction with the effects of polarization. Not only Stokes I, the total intensity, must be detected, but also the polarized intensities Stokes Q and U, each of them significantly weaker than Stokes I. This is the general challenge of polarimetry at (sub-)mm wavelength ranges and the advantage of ALMA being the most sensitive (sub-)mm instrument with this resolution at the moment. In the case of D2G_e-2, the clear radial polarization pattern and corresponding toroidal magnetic field structure can be identified in the simulated ALMA observation. The density gap, on the other hand, is observable with this setup neither in total nor in polarized emission. Furthermore, the polarization pattern shows a shallow twist. The twist in the CASA images, however, has a slightly different direction than CASA's input. The same effect is seen in the vortex of D2G_e-4 and likely originates from the resolution and corresponding data binning of the simulated observation or the simulation with CASA itself. In the case of D2G_e-4, the vortex as well as the toroidal magnetic field structure is detectable in the polarization pattern that would be observed by ALMA.

Concluding, by observing the polarized emission of the aligned dust in the disk, it is not possible to detect the density gap (model D2G_e-2) but the toroidal magnetic field structure as well as the vortex in model D2G_e-4. These simulations are able to distinguish between different models of protoplanetary disks and magnetic fields therein. Future observations, such as the proposed observations of TW Hya with ALMA, will strongly benefit from this analysis tool.

6.6. Summary

The extended version of MC3D that has been developed in the context of this thesis is one of the first 3D radiative transfer codes available today that consider dust grain alignment and polarized dust emission of non-spherical grains. This tool enables the comprehensive analysis of (sub-)mm observations of polarized radiation of protoplanetary disks performed with, e.g., ALMA and CARMA. Tests have been conducted that demonstrate the validity of the code. The major features, implemented in the context of this thesis, are the following.

1. MC3D makes use of a hybrid approach that combines treatment of spherical and non-spherical grain shape models.
2. The anisotropy of the radiation field, as well as the efficiency of dust grain alignment is computed for a given dust and disk model.
3. MC3D is able to read-in dust density distributions and magnetic fields from MHD simulations of protoplanetary disks.

4. SEDs of the polarized emission of aligned non-spherical dust grains are a tool to distinguish between different disk models and magnetic fields therein, where SEDs of the total emission do not trace differences.
5. Spatially resolved polarization maps trace the polarized dust emission of protoplanetary disks depending on dust and disk parameters, as well as dependent on magnetic field and resolution of the simulated observation. They enable the preparation and analysis of observations of polarized dust emission obtained with, e.g., ALMA.

The unprecedented sensitivity and resolution of ALMA finally allow for spatially observations of the polarized dust emission of protoplanetary disks. The polarization signal which was previously canceled out by a lack of sufficient spatial resolution, is now observable. Such observations need radiative transfer simulation as analysis tool. In this way, differences in underlying dust models, disk models, and magnetic field models can be revealed.

7. Summary of the thesis, concluding remarks and future directions

7.1. Summary of the thesis

The goal of this thesis has been to find new insights into the role of magnetic fields during the formation of stars and planets by investigating new analysis methods that can move the ongoing debate forward. The way to realize this challenge was to follow two different but complementary approaches: observations and simulations of polarized radiation from star- and planet-forming regions in different evolutionary stages.

The first part of this thesis was dedicated to observations of the earliest stage of star formation in the form of a multi-wavelength polarimetry study. The aim of this study was to detect the large-scale magnetic fields in the three low-mass star formation regions B335, CB68, and CB54. The observations of these three Bok globules were performed at three different telescopes, with the instruments ISAAC/VLT and SOFI/NTT in the near-IR wavelength range, and with IFOSC/IGO in the optical wavelength range. None of these instruments supports pipelines for the reduction of polarimetric data. Therefore, pipelines for data reduction and analysis had to be developed for each of these instruments. Through the course of the analysis, it was found that polarimetry with ISAAC/VLT is significantly biased by an hitherto unknown influence of instrumental polarization. This instrumental bias was quantified and corrected by calculating a calibration curve which is applicable to all polarimetric observations performed with ISAAC/VLT. The other two instruments did not show any evidence of such an instrumental influence. The near-IR and optical observations of the three Bok globules that trace the large-scale structures of the objects were combined with archival optical observations and sub-millimeter observations that trace the small-scale structures of the objects. The outcome of these observations are magnetic field measurements on scales of $10^2 - 10^5$ AU within the globules. The three observed Bok globules have different complex structures, different sizes and masses. Yet, they all show strongly aligned polarization vectors that indicate dominant magnetic fields on a wide range of spatial scales.

The second part of this thesis was devoted to radiative transfer simulations of polarized dust emission of protoplanetary disks. The goal was to create one of the first 3D radiative transfer codes that compute the polarized emission of aligned non-spherical dust grains. Therefore, the 3D radiative transfer code MC3D was extended in the context of this thesis by the concepts of polarized dust emission and alignment of dust grains situated in a radiation field. The implementation has been successfully verified in tests. This extended version of MC3D is capable of predicting and analyzing observations of polarized dust emission with both spectrally resolved SEDs and spatially resolved polarization maps. Now, with the previously unattainable sensitivity and spatial resolution of ALMA, it is finally possible to observe the polarized dust emission of protoplanetary disks. Codes like MC3D, as it was extended in the context of this thesis, are necessary to support such observations of polarized radiation. Furthermore, in order to pay tribute to recent observations of asymmetries in protoplanetary disks, and further make use of the gain in computational power, MC3D was prepared to take results from magnetohydrodynamic simulations as input data. That way, the magnetic field and the dust density distribution are no longer defined solely by an analytical approach. An application of these 3D MHD + RT simulations coupled with the ALMA simulator CASA demonstrated the conjunction of basic theoretical work with radiative transfer and observations. This conjunction allows for a deeper understanding of the physics derived from observations of polarized radiation of protoplanetary disks by revealing the differences of underlying dust, disk, and magnetic field models.

7.2. Concluding remarks and future directions

During the last couple of years, the interest in magnetic fields in the star and planet formation community has grown. This change was incited by a number of factors. On the one hand, by new developments in the theory of dust grain alignment as well as the gain in computational power that opened possibilities in magnetohydrodynamic and radiative transfer simulations. On the other hand, polarimetry has experienced a new boost as it had just become an important element in the design of a number of new high-performance instruments like the Spectro-Polarimetric High-contrast Exoplanet REsearch instrument (SPHERE) at the VLT or the Gemini Planet Imager (GPI) at Gemini South. Even ALMA supports continuum polarimetry and will soon support spatially resolved spectro-polarimetry as well (scheduled for Cycle 4, April 2016). These are currently the most sensitive polarimeters able to observe with high spatial resolution. Observations like the planned study of the protoplanetary disk TW Hya (see Sect. 6.5.2.2) with ALMA will reveal unprecedented insights in the physics, respectively, the role of magnetic fields in star- and planet-forming objects. With the upcoming 40m-class telescope European Extremely Large Telescope (E-ELT, scheduled for 2026) and its polarization modes, the field will be pushed forward even more. On the short term, the multi-wavelength polarimetry study of Bok globules will be expanded by observations of two globules with complex density structures, CB34 and [OMK2002] 18 (accepted project 096.C−0115, PI: Bertrang). These observations will broaden the study conducted in the context of this thesis to test whether dominant magnetic fields are the general case. Further observations are planned.

However, as shown in this thesis, observations alone are not sufficient to investigate the complete physical picture. The previous developments of dust grain alignment mechanisms are valuable, nevertheless, the development needs to keep going on. There are still too many unknowns in the theory of alignment mechanisms. The same is true for radiative transfer simulations of polarized emission. The major point here will be the investigation of scattering effects due to large, non-spherical dust grains. So far, it is assumed that scattering is negligible in the (sub-)mm wavelength range. With further developments of radiative transfer simulations, this could finally be validated. Additional to scattering effects, radiative transfer simulations including the Zeeman splitting of spectral lines will be required in the close future to support observations with upcoming observation modes of, e.g., ALMA, for spatially resolved spectro-polarimetry that directly measure the magnetic field strength. On the short term, the code developed in the context of this thesis will be used to further investigate the influences of different parameters in the model setup and will be applied to planned observations with ALMA.

The importance of magnetic field investigations, and thus, polarimetry will grow further in the future. With the necessary instruments, both observations and simulations, we may finally answer the question about the role of magnetic fields in star formation, and push the techniques we used for this to new fields like characterizing atmospheres of exo-planets, maybe even an exo-Earth, and, of course, discover things we do not even dream of yet.

Appendices

A. Data reduction and analysis pipelines

Flowcharts of the data reduction and analysis pipelines are shown in Fig. A.1. In the following, some pipeline parts are described in more detail.

Bad pixels. To detect and clean cosmic ray hits from all data frames, the publicly available Python script `cosmics.py` (Tewes 2010) has been applied. `cosmics.py` is based on the Laplacian Cosmic Ray Identification algorithm (L.A. Comics by van Dokkum 2001). To distinguish cosmic ray hits from saturated stars, `cosmics.py` requires a maximum number of connected pixels that shall be recognized as cosmic ray hits. Typically, this number is set to 5; (saturated) stars occupy a much more larger region of the detector. In multiple iterations (typically 4), `cosmics.py` locates the saturated pixels. If they are identified as cosmic ray hits, they are masked and the corresponding pixel value is replaced by the median of the surrounding pixel values.

Dark current reduction. Master dark frames are prepared for and subtracted from the data obtained with IFOSC/IGO and ISAAC/VLT. In the latter case, the the ESO Recipe Execution Tool (`EsoRex` v3.9.6; ESO 2012). The corresponding ISAAC/VLT recipe `isaac_img_dark` is applied.

Flat fielding procedure for SOFI/NTT. For SOFI/NTT, the recommended procedure for flat field correction are Dome flat fields where a series of exposures with the lamp turned on and off is taken (Wolf et al. 2002*a*). Since the Wollaston prism changes the flat field in comparison to the flat field without Wollaston prism, the prism needs to be in the optical path when the Dome flats are obtained. The exposures for the flat field should be carried out as follows:

$$\begin{aligned}\text{Exposure 1 } (e_1) &: \text{lamp-off}\\ \text{Exposure 2 } (e_2) &: \text{lamp-on}\\ \text{Exposure 3 } (e_3) &: \text{lamp-on}\\ \text{Exposure 4 } (e_4) &: \text{lamp-off}\end{aligned} \tag{A.1}$$

where the lamp that illuminates the Dome is turned on and off. For the exposures with lamp-on, the flat field frame should show typically a signal of 4000 ADU (Analog-to-Digital Unit, i.e., detector counts).
The Dome flat, f, is derived from the exposure sequence as:

$$f = (e_2 - e_1) + (e_3 - e_4). \tag{A.2}$$

Since the complete instrument is rotated to observe different polarization filter orientations, separate flat fields for different orientations are not required. The relative brightness profiles in the fields #3 and #4 (see Fig. 3.3) occur only in polarization mode and originate from the Wollaston prism and the polarimetric mask (and are independent from Dark current, in first order, Wolf et al. 2002*a*).

The resulting flat field, f, is polarized, i.e., the median value of the O field differs from the median value of the E field (see Fig. 3.3). This can be adjusted by an independent normalization of each field, $f_{\mathrm{O},0}$ and $f_{\mathrm{E},0}$:

$$\begin{aligned} f_{\mathrm{O},1} &= \frac{f_{\mathrm{O},0}}{\mathrm{median}(f_{\mathrm{O},0})}, \\ f_{\mathrm{E},1} &= \frac{f_{\mathrm{E},0}}{\mathrm{median}(f_{\mathrm{E},0})}, \end{aligned} \tag{A.3}$$

assuming that the pixel-to-pixel variation is negligible, i.e., the fields themselves are not polarized. Measurements of the polarization within $f_{\mathrm{O},0}$ and $f_{\mathrm{E},0}$ in K band support this: The degree of polarization is less than 0.05%, thus, negligible compared to other sources of error (Wolf et al. 2002*a*).
To perform the flat field correction, O field and E field of the image, $i_{\mathrm{O},0}$ and $i_{\mathrm{E},0}$, must be divided by the corresponding normalized flat field:

$$\begin{aligned} i_{\mathrm{O},1} &= \frac{i_{\mathrm{O},0}}{f_{\mathrm{O},1}}, \\ i_{\mathrm{E},1} &= \frac{i_{\mathrm{E},0}}{f_{\mathrm{E},1}}. \end{aligned} \tag{A.4}$$

In this way, the flat field correction does not introduce any artificial polarization to the image data.

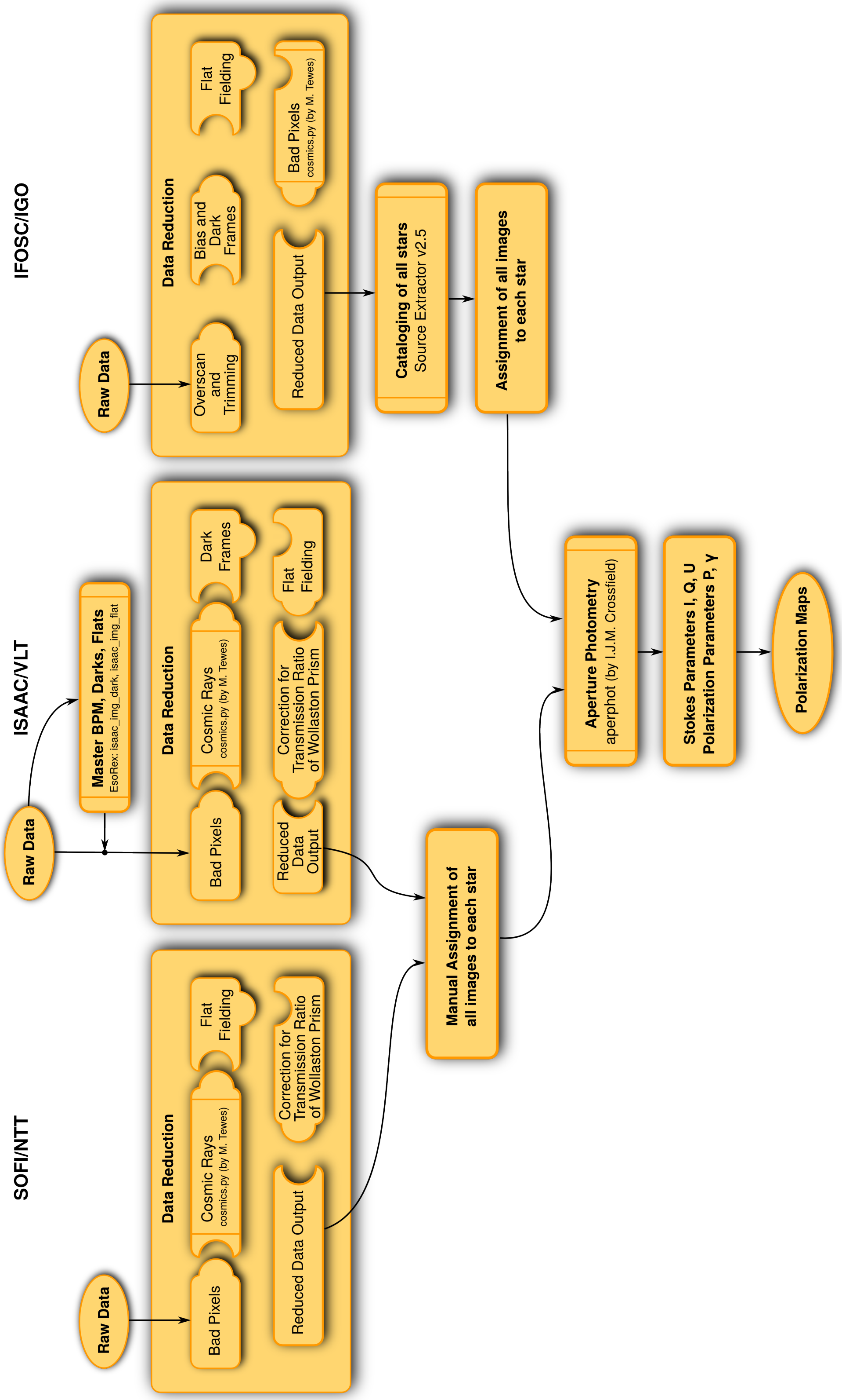

Fig. A.1.: Flow charts of the data reduction and analysis pipelines for SOFI/NTT (*left*), ISAAC/VLT (*middle*), and IFOSC/IGO (*right*).

List of Figures

List of Tables

List of Abbreviations

ADU	Analog-to-Digital Unit, i.e. detector counts
ALMA	Atacama Large Millimeter/submillimeter Array
AMO	Analytical MOdel (Lazarian & Hoang 2007*a*)
AE	Astronomische Einheit (1.4960×10^{11} m)
AU	Astronomical unit (1.4960×10^{11} m)
BPM	Bad pixel map
CASA	Common Astronomy Software Applications (CASA Group 2014)
CCD	Charge-coupled Device
CF method	Chandrasekhar-Fermi method (Chandrasekhar & Fermi 1953)
CL07	Cho & Lazarian (2007)
CO	Carbon monoxide
cTTS	Classical T Tauri star
DDSCAT	Discrete dipole approximation code (Draine & Flatau 1994, 2013)
dia.	Diameter
DSS	Digitized Sky Survey, optical wavelength range
E-ELT	European Extremely Large Telescope
ESO	European Southern Observatories
far-IR	far infrared wavelength range (approx. $25 - 350\,\mu$m)
FOV	Field-of-view
FWHM	Full Width at Half Maximum
GMC	Giant molecular cloud
GPI	Gemini Planet Imager at Gemini South
HHT	Heinrich Hertz Submillimeter Telescope
HWP	Half-wave plate
IGO	IUCAA Girawali Observatory, Maharashtra, India

IFOSC	IUCAA Faint Object Spectrograph & Camera
IR	Infrared wavelength range (approx. $0.7 - 350\,\mu$m)
ISAAC	Infrared Spectrometer And Array Camera
ISM	Interstellar medium
IUCAA	Inter-University Center for Astronomy and Astrophysics, India
Js	Js-band filter with a central wavelength of $1.24\,\mu$m
L.A. Comics	Laplacian Cosmic Ray Identification algorithm (van Dokkum 2001)
LOS	Line-of-sight
MHD	Magnetohydrodynamic
mid-IR	mid infrared wavelength range (approx. $5 - 25\,\mu$m)
MRI	Magneto-rotational instability
MRN	Mathis Rumpl Nordsieck dust grain size distribution (Mathis et al. 1977)
Near-IR	Near-infrared wavelength range (approx. $0.7 - 5\,\mu$m)
NTT	New Technology Telescope, ESO, La Silla, Chile
optical	Optical wavelength range (approx. $0.4 - 0.7\,\mu$m)
OTF	On The Fly observation
pc	Parsec, the parallax of one arcsecond (3.0857×10^{16} m)
POS	Plane-of-sky
PSF	Point spread function
R	R-band filter covering 550 nm − 800 nm
RAT	Radiative torque
RT	Radiative transfer
RWI	Rossby Wave Instability
SED	Spectral energy distribution
SFR	Star formation rate
SNR	Signal-to-noise ratio
SOFI	Son OF ISAAC
SPHERE	Spectro-Polarimetric High-contrast Exoplanet REsearch instrument at VLT
Sub-mm	Sub-millimeter wavelength range (approx. $350 - 1000\,\mu$m)

SURF	SCUBA User Reduction Facility (Jenness & Lightfoot 1998)
SVM	Separation of variables method
TMM	T-Matrix method
UV	Ultraviolet wavelength range (approx. $0.01 - 0.4\,\mu$m)
VLT	Very Large Telescope, ESO, Paranal, Chile
wTTS	Weak-line T Tauri star
YSO	Young stellar objects

Bibliography

Abbas, M. M., P. D. Craven, J. F. Spann, D. Tankosic, A. LeClair, D. L. Gallagher, E. A. West, J. C. Weingartner, W. K. Witherow, and A. G. G. M. Tielens. 2004. Laboratory Experiments on Rotation and Alignment of the Analogs of Interstellar Dust Grains by Radiation. ApJ**614:**781–795.

Ade, P. A. R., R. W. Aikin, D. Barkats, S. J. Benton, C. A. Bischoff, J. J. Bock, J. A. Brevik, I. Buder, E. Bullock, C. D. Dowell, L. Duband, J. P. Filippini, S. Fliescher, S. R. Golwala, M. Halpern, M. Hasselfield, S. R. Hildebrandt, G. C. Hilton, V. V. Hristov, K. D. Irwin, K. S. Karkare, J. P. Kaufman, B. G. Keating, S. A. Kernasovskiy, J. M. Kovac, C. L. Kuo, E. M. Leitch, M. Lueker, P. Mason, C. B. Netterfield, H. T. Nguyen, R. O'Brient, R. W. Ogburn, A. Orlando, C. Pryke, C. D. Reintsema, S. Richter, R. Schwarz, C. D. Sheehy, Z. K. Staniszewski, R. V. Sudiwala, G. P. Teply, J. E. Tolan, A. D. Turner, A. G. Vieregg, C. L. Wong, K. W. Yoon, and Bicep2 Collaboration. 2014. Detection of B-Mode Polarization at Degree Angular Scales by BICEP2. Physical Review Letters **112:**241101.

Agertz, O., A. V. Kravtsov, S. N. Leitner, and N. Y. Gnedin. 2013. Toward a Complete Accounting of Energy and Momentum from Stellar Feedback in Galaxy Formation Simulations. ApJ**770:**25.

Alves, F. O., J. A. Acosta-Pulido, J. M. Girart, G. A. P. Franco, and R. López. 2011. Infrared and Optical Polarimetry around the Low-mass Star-forming Region NGC 1333 IRAS 4A. AJ**142:**33.

Andersson, B.-G. 2015. Interstellar grain alignment: Observational status. Pages 59–87 in A. Lazarian, E. M. de Gouveia Dal Pino, and C. Melioli, editors. Magnetic fields in diffuse media, volume 407 of *Astrophysics and Space Science Library*. Springer Berlin Heidelberg.
URL `http://dx.doi.org/10.1007/978-3-662-44625-6_4`

Balbus, S. A., and J. F. Hawley. 1991. A powerful local shear instability in weakly magnetized disks. I - Linear analysis. II - Nonlinear evolution. ApJ**376:**214–233.

Balbus, S. A., and J. F. Hawley. 1998. Instability, turbulence, and enhanced transport in accretion disks. RMP **70:**1–53.

Balbus, S. A., J. F. Hawley, and J. M. Stone. 1996. Nonlinear Stability, Hydrodynamical Turbulence, and Transport in Disks. ApJ**467:**76.

Barber, P., and C. Yeh. 1975. Scattering of electromagnetic waves by arbitrarily shaped dielectric bodies. Appl. Opt.**14:**2864–2872.

Bertin, E. 2012. SExtractor – astronomical source extractor.
URL `http://sextractor.sourceforge.net/`

Bertrang, G. 2010. Magnetic fields in star-forming regions, Diploma thesis, Kiel University, Germany.

Bertrang, G., S. Wolf, and H. S. Das. 2014. Large-scale magnetic fields in Bok globules. A&A**565:**A94.

BICEP2/Keck and Planck Collaborations, P. A. R. Ade, N. Aghanim, Z. Ahmed, R. W. Aikin, K. D. Alexander, M. Arnaud, J. Aumont, C. Baccigalupi, A. J. Banday, and et al. 2015. Joint Analysis of BICEP2/Keck Array and Planck Data. Physical Review Letters **114:**101301.

Bjorkman, J. E., and K. Wood. 2001. Radiative Equilibrium and Temperature Correction in Monte Carlo Radiation Transfer. ApJ**554:**615–623.

Bohren, C. F., and D. R. Huffman. 1998. Absorption and scattering of light by small particles. Wiley-VCH.

Bok, B. J. 1977. Dark Nebulae, Globules, and Protostars. PASP**89:**597.

Boss, A. P. 2004. Evolution of the Solar Nebula. VI. Mixing and Transport of Isotopic Heterogeneity. ApJ**616:**1265–1277.

Bouvier, J., S. H. P. Alencar, T. J. Harries, C. M. Johns-Krull, and M. M. Romanova. 2007. Magnetospheric Accretion in Classical T Tauri Stars. Protostars and Planets V pages 479–494 .

Brand, J., and L. Blitz. 1993. The Velocity Field of the Outer Galaxy. A&A**275:**67.

Burlaga, L. F., N. F. Ness, and E. C. Stone. 2013. Magnetic field observations as voyager 1 entered the heliosheath depletion region. Science **341:**147–150.

CASA Group. 2014. Common Astronomy Software Applications, *v4.2*. `http://casa.nrao.edu`.

Casassus, S., G. van der Plas, S. P. M, W. R. F. Dent, E. Fomalont, J. Hagelberg, A. Hales, A. Jordán, D. Mawet, F. Ménard, A. Wootten, D. Wilner, A. M. Hughes, M. R. Schreiber, J. H. Girard, B. Ercolano, H. Canovas, P. E. Román, and V. Salinas. 2013. Flows of gas through a protoplanetary gap. Nature**493:**191–194.

Cashwell, E., and C. Everett. 1959. A practical manual on the Monte Carlo method for random walk problems, International tracts in computer science and technology and their application. Pergamon Press.

Chambers, J. E. 2006. Planet Formation with Migration. ApJ**652:**L133–L136.

Chandler, C. J., and A. I. Sargent. 1993. The small-scale structure and kinematics of B335. ApJ**414:**L29–L32.

Chandrasekhar, S., and E. Fermi. 1953. Magnetic Fields in Spiral Arms. ApJ**118:**113.

Chiang, E. I., M. K. Joung, M. J. Creech-Eakman, C. Qi, J. E. Kessler, G. A. Blake, and E. F. van Dishoeck. 2001. Spectral Energy Distributions of Passive T Tauri and Herbig Ae Disks: Grain Mineralogy, Parameter Dependences, and Comparison with Infrared Space Observatory LWS Observations. ApJ**547:**1077–1089.

Childs, H., E. Brugger, B. Whitlock, J. Meredith, S. Ahern, D. Pugmire, K. Biagas, M. Miller, C. Harrison, G. H. Weber, H. Krishnan, T. Fogal, A. Sanderson, C. Garth, E. W. Bethel, D. Camp, O. Rübel, M. Durant, J. M. Favre, and P. Navrátil. 2012. VisIt: An End-User Tool For Visualizing and Analyzing Very Large Data. In High Performance Visualization–Enabling Extreme-Scale Scientific Insight.

Cho, J., and A. Lazarian. 2005. Grain Alignment by Radiation in Dark Clouds and Cores. ApJ**631:**361–370.

Cho, J., and A. Lazarian. 2007. Grain Alignment and Polarized Emission from Magnetized T Tauri Disks. ApJ**669:**1085–1097.

Choi, M., N. J. Evans, II, E. M. Gregersen, and Y. Wang. 1995. Modeling Line Profiles of Protostellar Collapse in B335 with the Monte Carlo Method. ApJ**448:**742.

Ciesla, F. J. 2007. Dust Coagulation and Settling in Layered Protoplanetary Disks. ApJ**654:**L159–L162.

Clayton, G. C., and P. G. Martin. 1981. On the intrinsic polarization of red dwarfs. AJ**86:**1518.

Cleeves, L. I., E. A. Bergin, C. Qi, F. C. Adams, and K. I. Öberg. 2015. Constraining the X-Ray and Cosmic-Ray Ionization Chemistry of the TW Hya Protoplanetary Disk: Evidence for a Sub-interstellar Cosmic-Ray Rate. ApJ**799:**204.

Clemens, D. P., J. L. Yun, and M. H. Heyer. 1991. BOK globules and small molecular clouds - Deep IRAS photometry and (C-12)O spectroscopy. ApJS**75:**877–904.

Cohen, R. J., P. R. Rowland, and M. M. Blair. 1984. The source of the bipolar outflow in Cepheus A. MNRAS**210:**425–438.

Crutcher, R. M. 2006. ASTRONOMY: Testing star formation theory. Science **313:**771–772.

Crutcher, R. M. 2012. Magnetic Fields in Molecular Clouds. ARA&A**50:**29–63.

D'Alessio, P., N. Calvet, and L. Hartmann. 2001. Accretion Disks around Young Objects. III. Grain Growth. ApJ**553:**321–334.

D'Alessio, P., N. Calvet, L. Hartmann, S. Lizano, and J. Cantó. 1999. Accretion Disks around Young Objects. II. Tests of Well-mixed Models with ISM Dust. ApJ**527:**893–909.

D'Alessio, P., J. Cantö, N. Calvet, and S. Lizano. 1998. Accretion Disks around Young Objects. I. The Detailed Vertical Structure. ApJ**500:**411–427.

Davis, L., Jr., and J. L. Greenstein. 1951. The Polarization of Starlight by Aligned Dust Grains. ApJ**114:**206.

Dohnanyi, J. S. 1969. Collisional Model of Asteroids and Their Debris. J. Geophys. Res.**74:**2531–2554.

Dolginov, A. Z., and I. G. Mytrophanov. 1976. Orientation of cosmic dust grains. Ap&SS**43:**291–317.

Dotson, J. L., J. E. Vaillancourt, L. Kirby, C. D. Dowell, R. H. Hildebrand, and J. A. Davidson. 2010. 350 μm Polarimetry from the Caltech Submillimeter Observatory. ApJS**186:**406–426.

Draine, B. T. 1994. Dust in Diffuse Interstellar Clouds. In R. M. Cutri and W. B. Latter, editors. The first symposium on the infrared cirrus and diffuse interstellar clouds, volume 58 of *Astronomical Society of the Pacific Conference Series*, page 227 .

Draine, B. T. 1996. Optical and Magnetic Properties of Dust Grains. In W. G. Roberge and D. C. B. Whittet, editors. Polarimetry of the interstellar medium, volume 97 of *Astronomical Society of the Pacific Conference Series*, page 16 .

Draine, B. T. 2000. The Discrete Dipole Approximation for Light Scattering by Irregular Targets, page 131 .

Draine, B. T. 2003. Interstellar Dust Grains. ARA&A**41:**241–289.

Draine, B. T., and P. J. Flatau. 1994. Discrete-dipole approximation for scattering calculations. Journal of the Optical Society of America A **11:**1491–1499.

Draine, B. T., and P. J. Flatau. 2013. User Guide for the Discrete Dipole Approximation Code DDSCAT 7.3. ArXiv e-prints .

Draine, B. T., and H. M. Lee. 1984. Optical properties of interstellar graphite and silicate grains. ApJ**285:**89–108.

Draine, B. T., and S. Malhotra. 1993. On graphite and the 2175 A extinction profile. ApJ**414:**632–645.

Draine, B. T., and J. C. Weingartner. 1996. Radiative Torques on Interstellar Grains. I. Superthermal Spin-up. ApJ**470:**551.

Draine, B. T., and J. C. Weingartner. 1997. Radiative Torques on Interstellar Grains. II. Grain Alignment. ApJ**480:**633.

Dullemond, C. P. 2012. RADMC-3D: A multi-purpose radiative transfer tool. Astrophysics Source Code Library.

Efroimsky, M. 2002. Mechanical Alignment of Suprathermal Paramagnetic Cosmic-Dust Granules: The Cross Section Mechanism. ApJ**575:**886–899.

Epstein, E. E. 1977. The Aerospace Corporation, El Segundo, California. Observatory report. In Bulletin of the american astronomical society, volume 9 of *Bulletin of the American Astronomical Society*, pages 1–7 .

ESO. 2012. `EsoRex` v3.9.6, European Southern Observatory (ESO) Recipe Execution Tool.
URL `http://www.eso.org/sci/software/cpl/esorex.html`

European Space AGENCY (ESA). 2000. PLANCK.

Evans, N. J., II, J.-E. Lee, J. M. C. Rawlings, and M. Choi. 2005. B335: A Laboratory for Astrochemistry in a Collapsing Cloud. ApJ**626:**919–932.

Fischer, O. 1992. Modellierung der Polarisation in zirkumstellaren Staubhüllen unter Anwendung der Monte-Carlo-Methode, PhD thesis, Friedrich Schiller University Jena .

Flock, M., N. Dzyurkevich, H. Klahr, N. J. Turner, and T. Henning. 2011. Turbulence and Steady Flows in Three-dimensional Global Stratified Magnetohydrodynamic Simulations of Accretion Disks. ApJ**735:**122.

Flock, M., J. P. Ruge, N. Dzyurkevich, T. Henning, H. Klahr, and S. Wolf. 2015. Gaps, rings, and non-axisymmetric structures in protoplanetary disks. From simulations to ALMA observations. A&A**574:**A68.

Fossati, L., S. Bagnulo, E. Mason, and E. Landi Degl'Innocenti. 2007. Standard Stars for Linear Polarization Observed with FORS1. In C. Sterken, editor. The future of photometric, spectrophotometric and polarimetric standardization, volume 364 of *Astronomical Society of the Pacific Conference Series*, page 503 .

Fowler, M. 1997. Historical Beginnings of Theories of Electricity and Magnetism. URL `http://galileoandeinstein.physics.virginia.edu/more_stuff/E&M_Hist.html`

Frerking, M. A., W. D. Langer, and R. W. Wilson. 1987. The structure and dynamics of BOK globule B335. ApJ**313:**320–346.

Girart, J. M., R. Rao, and D. P. Marrone. 2006. Magnetic Fields in the Formation of Sun-Like Stars. Science **313:**812–814.

Gold, T. 1952*a*. Polarization of Starlight. Nature**169:**322.

Gold, T. 1952*b*. The alignment of galactic dust. MNRAS**112:**215.

Goodman, A. A., T. J. Jones, E. A. Lada, and P. C. Myers. 1995. Does Near-Infrared Polarimetry Reveal the Magnetic Field in Cold Dark Clouds? The Astrophysical Journal **448:**748–+.

Gräfe, C. 2013. Beobachtung und Modellierung zirkumstellarer Scheiben, PhD thesis, Kiel University, Germany.

Gräfe, C., S. Wolf, S. Guilloteau, A. Dutrey, K. R. Stapelfeldt, K. M. Pontoppidan, and J. Sauter. 2013. Vertical settling and radial segregation of large dust grains in the circumstellar disk of the Butterfly Star. A&A**553:**A69.

Gupta, R., M. Burse, H. K. Das, A. Kohok, and A. N. Ramaprakash. 2002. IUCAA 2 meter telescope and its first light instrument IFOSC. Bull. Astr. Soc. India **30:**785.

Hales, A. S., I. De Gregorio-Monsalvo, B. Montesinos, S. Casassus, W. F. R. Dent, C. Dougados, C. Eiroa, A. M. Hughes, G. Garay, D. Mardones, F. Ménard, A. Palau, S. Pérez, N. Phillips, J. M. Torrelles, and D. Wilner. 2014. A CO Survey in Planet-forming Disks: Characterizing the Gas Content in the Epoch of Planet Formation. AJ**148:**47.

Hall, J. S. 1949. Observations of the Polarized Light from Stars. Science **109:**166–167.

Harvey, D. W. A., D. J. Wilner, P. C. Myers, and M. Tafalla. 2003. Disk Properties and Density Structure of the Star-forming Dense Core B335. ApJ**596:**383–388.

Henning, T., S. Wolf, R. Launhardt, and R. Waters. 2001. Measurements of the Magnetic Field Geometry and Strength in Bok Globules. ApJ**561:**871–879.

Hiltner, W. A. 1949. On the Presence of Polarization in the Continuous Radiation of Stars. II. ApJ**109:**471.

Holland, W. S., D. Bintley, E. L. Chapin, A. Chrysostomou, G. R. Davis, J. T. Dempsey, W. D. Duncan, M. Fich, P. Friberg, M. Halpern, K. D. Irwin, T. Jenness, B. D. Kelly, M. J. MacIntosh, E. I. Robson, D. Scott, P. A. R. Ade, E. Atad-Ettedgui, D. S. Berry, S. C. Craig, X. Gao, A. G. Gibb, G. C. Hilton, M. I. Hollister, J. B. Kycia, D. W. Lunney, H. McGregor, D. Montgomery, W. Parkes, R. P. J. Tilanus, J. N. Ullom, C. A. Walther, A. J. Walton, A. L. Woodcraft, M. Amiri, D. Atkinson, B. Burger, T. Chuter, I. M. Coulson, W. B. Doriese, C. Dunare, F. Economou, M. D. Niemack, H. A. L. Parsons, C. D. Reintsema, B. Sibthorpe, I. Smail, R. Sudiwala, and H. S. Thomas. 2013. SCUBA-2: the 10 000 pixel bolometer camera on the James Clerk Maxwell Telescope. MNRAS**430:**2513–2533.

Houde, M. 2004. Evaluating the Magnetic Field Strength in Molecular Clouds. ApJ**616:**L111–L114.

Hughes, A. M., D. J. Wilner, S. M. Andrews, C. Qi, and M. R. Hogerheijde. 2011. Empirical Constraints on Turbulence in Protoplanetary Accretion Disks. ApJ**727:**85.

Hull, C. L. H., and R. L. Plambeck. 2015. The 1.3 mm Full-Stokes Polarization System at CARMA. ArXiv e-prints .

Hull, C. L. H., R. L. Plambeck, A. D. Bolatto, G. C. Bower, J. M. Carpenter, R. M. Crutcher, J. D. Fiege, E. Franzmann, N. S. Hakobian, C. Heiles, M. Houde, A. M. Hughes, K. Jameson, W. Kwon, J. W. Lamb, L. W. Looney, B. C. Matthews, L. Mundy, T. Pillai, M. W. Pound, I. W. Stephens, J. J. Tobin, J. E. Vaillancourt, N. H. Volgenau, and M. C. H. Wright. 2013. Misalignment of Magnetic Fields and Outflows in Protostellar Cores. ApJ**768:**159.

Ichiki, K., K. Takahashi, H. Ohno, H. Hanayama, and N. Sugiyama. 2006. Cosmological magnetic field: a fossil of density perturbations in the early universe. Science **311:**827.

Isella, A. 2006. Interferometric observations of pre-main sequence disks, PhD thesis, University of Milan, Italy.

Jenness, T., and J. F. Lightfoot. 1998. Reducing SCUBA Data at the James Clerk Maxwell Telescope. In R. Albrecht, R. N. Hook, and H. A. Bushouse, editors.

Astronomical data analysis software and systems vii, volume 145 of *Astronomical Society of the Pacific Conference Series*, page 216 .

Jones, R. V., and L. Spitzer, Jr. 1967. Magnetic Alignment of Interstellar Grains. ApJ**147:**943.

Jones, T. J., and H. Amini. 2003. The Magnetic Field Geometry in DR 21. AJ**125:**1418–1425.

Kennicutt, R. C., and N. J. Evans. 2012. Star Formation in the Milky Way and Nearby Galaxies. ARA&A**50:**531–608.

Khlebtsov, B., V. Khanadeev, T. Pylaev, and N. Khlebtsov. 2011. A new t-matrix solvable model for nanorods: TEM-based ensemble simulations supported by experiments. J. Phys. Chem. C **115:**6317–6323.

Kim, S.-H., and P. G. Martin. 1995. The size distribution of interstellar dust particles as determined from polarization: Spheroids. ApJ**444:**293–305.

Kirchhoff, G. 1860. Ueber das Verhältniss zwischen dem Emissionsvermögen und dem Absorptionsvermögen der Körper für Wärme und Licht. Annalen der Physik **185:**275–301.

Kirchschlager, F., and S. Wolf. 2014. Effect of dust grain porosity on the appearance of protoplanetary disks. A&A**568:**A103.

Krause, M. 2009. Magnetic Fields and Star Formation in Spiral Galaxies. In Revista mexicana de astronomia y astrofisica conference series, volume 36 of *Revista Mexicana de Astronomia y Astrofisica, vol. 27*, pages 25–29 .

Kroese, D. P., T. Taimre, and Z. I. Botev. 2011. Handbook of monte carlo methods. Wiley.

Lada, C. J. 1987. Star formation - From OB associations to protostars. In M. Peimbert and J. Jugaku, editors. Star forming regions, volume 115 of *IAU Symposium*, pages 1–17 .

Lada, C. J. 1999. The Formation of Low Mass Stars: An Observational Overview. In C. J. Lada and N. D. Kylafis, editors. Nato advanced science institutes (asi) series c, volume 540 of *NATO Advanced Science Institutes (ASI) Series C*, page 143 .

Lada, C. J., J. F. Alves, and M. Lombardi. 2007. Near-Infrared Extinction and Molecular Cloud Structure. Protostars and Planets V pages 3–15 .

Lada, C. J., and B. A. Wilking. 1984. The nature of the embedded population in the Rho Ophiuchi dark cloud - Mid-infrared observations. ApJ**287:**610–621.

Launhardt, R., and T. Henning. 1997. Millimetre dust emission from northern BOK globules. A&A**326:**329–346.

Launhardt, R., A. M. Stutz, A. Schmiedeke, T. Henning, O. Krause, Z. Balog, H. Beuther, S. Birkmann, M. Hennemann, J. Kainulainen, T. Khanzadyan, H. Linz, N. Lippok, M. Nielbock, J. Pitann, S. Ragan, C. Risacher, M. Schmalzl, Y. L. Shirley, B. Stecklum, J. Steinacker, and J. Tackenberg. 2013. The Earliest Phases of Star Formation (EPoS): a Herschel key project. The thermal structure of low-mass molecular cloud cores. A&A**551:**A98.

Lazarian, A. 1995. Mechanical Alignment of Suprathermally Rotating Grains. ApJ**451:**660.

Lazarian, A. 2007. Tracing magnetic fields with aligned grains. J. Quant. Spec. Radiat. Transf.**106:**225–256.

Lazarian, A., B. G. Andersson, and T. Hoang. 2015. CUP, in press.

Lazarian, A., and D. Finkbeiner. 2003. Microwave emission from aligned dust. New A Rev.**47:**1107–1116.

Lazarian, A., A. A. Goodman, and P. C. Myers. 1997. On the Efficiency of Grain Alignment in Dark Clouds. The Astrophysical Journal **490:**273–+.

Lazarian, A., and T. Hoang. 2007*a*. Radiative torques: analytical model and basic properties. MNRAS**378:**910–946.

Lazarian, A., and T. Hoang. 2007*b*. Subsonic Mechanical Alignment of Irregular Grains. ApJ**669:**L77–L80.

Leung, C. M. 1985. Physical conditions in isolated dark globules. In D. C. Black and M. S. Matthews, editors. Protostars and planets ii, pages 104–136 .

Li, H.-B., and T. Henning. 2011. The alignment of molecular cloud magnetic fields with the spiral arms in M33. Nature**479:**499–501.

Liddle, A. R., and D. H. Lyth. 2000. Cosmological inflation and large-scale structure. Cambridge University Press .

Lilley, A. E. 1955. The Association of Gas and Dust from 21-CM Hydrogen Radio Observations. ApJ**121:**559.

Lucy, L. B. 1999. Computing radiative equilibria with Monte Carlo techniques. A&A**344:**282–288.

Lynden-Bell, D., and J. E. Pringle. 1974. The evolution of viscous discs and the origin of the nebular variables. MNRAS**168:**603–637.

Marino, S., S. Perez, and S. Casassus. 2015. Shadows Cast by a Warp in the HD 142527 Protoplanetary Disk. ApJ**798:**L44.

Mason, E., A. Kaufer, and O. Hainaut. 2007. Very Large Telescope Paranal Science Operations INSTRUMENT data reduction cookbook, Issue 80.0. URL `http://www.eso.org/sci/facilities/paranal/decommissioned/isaac/doc/VLT-MAN-ESO-14100-4031_v80.pdf`

Mathis, J. S. 1986. The alignment of interstellar grains. ApJ**308:**281–287.

Mathis, J. S., W. Rumpl, and K. H. Nordsieck. 1977. The size distribution of interstellar grains. ApJ**217:**425–433.

Matsumoto, T., T. Nakazato, and K. Tomisaka. 2006. Alignment of Outflows with Magnetic Fields in Cloud Cores. ApJ**637:**L105–L108.

Matthews, B. C., C. A. McPhee, L. M. Fissel, and R. L. Curran. 2009. The Legacy of SCUPOL: 850 μm Imaging Polarimetry from 1997 to 2005. ApJS**182:**143–204.

Meru, F., M. Galvagni, C. Olczak, and P. Garaud. 2014. Large grains can grow in circumstellar discs. In M. Booth, B. C. Matthews, and J. R. Graham, editors. Iau symposium, volume 299 of *IAU Symposium*, pages 169–170 .

Meyer, M. R., D. E. Backman, A. J. Weinberger, and M. C. Wyatt. 2007. Evolution of Circumstellar Disks Around Normal Stars: Placing Our Solar System in Context. PP V pages 573–588 .

Mie, G. 1908. Beiträge zur Optik trüber Medien, speziell kolloidaler Metallösungen. Annalen der Physik **330:**377–445.

Mignone, A., G. Bodo, S. Massaglia, T. Matsakos, O. Tesileanu, C. Zanni, and A. Ferrari. 2007. PLUTO: A Numerical Code for Computational Astrophysics. ApJS**170:**228–242.

Mignone, A., M. Flock, M. Stute, S. M. Kolb, and G. Muscianisi. 2012. A conservative orbital advection scheme for simulations of magnetized shear flows with the PLUTO code. A&A**545:**A152.

Moorwood, A., J.-G. Cuby, P. Biereichel, J. Brynnel, B. Delabre, N. Devillard, A. van Dijsseldonk, G. Finger, H. Gemperlein, R. Gilmozzi, T. Herlin, G. Huster, J. Knudstrup, C. Lidman, J.-L. Lizon, H. Mehrgan, M. Meyer, G. Nicolini, M. Petr, J. Spyromilio, and J. Stegmeier. 1998. ISAAC sees first light at the VLT. The Messenger **94:**7–9.

Mouschovias, T. C., and G. E. Ciolek. 1999. Magnetic Fields and Star Formation: A Theory Reaching Adulthood. In C. J. Lada and N. D. Kylafis, editors. Nato advanced science institutes (asi) series c, volume 540 of *NATO Advanced Science Institutes (ASI) Series C*, page 305 .

Mrówczyński, S., and M. H. Thoma. 2007. What Do Electromagnetic Plasmas Tell Us about the Quark-Gluon Plasma? Annual Review of Nuclear and Particle Science **57:**61–94.

Natta, A., L. Testi, N. Calvet, T. Henning, R. Waters, and D. Wilner. 2007. Dust in Protoplanetary Disks: Properties and Evolution. PP V pages 767–781 .

Olofsson, S., and G. Olofsson. 2009. A new method of determining distances to dark globules. The distance to B 335. A&A**498:**455–461.

Padoan, P., C. Federrath, G. Chabrier, N. J. Evans, II, D. Johnstone, J. K. Jørgensen, C. F. McKee, and Å. Nordlund. 2013. The Star Formation Rate of Molecular Clouds. ArXiv e-prints .

Perelman, A. Y. 1979. Scattering in spherically symmetric media. Appl. Opt.**18:**2307–2314.

Perelman, A. Y., and N. V. Voshchinnikov. 2002. Improved S-approximation for dielectric particles. J. Quant. Spec. Radiat. Transf.**72:**607–621.

Pérez, L. M., A. Isella, J. M. Carpenter, and C. J. Chandler. 2014. Large-scale Asymmetries in the Transitional Disks of SAO 206462 and SR 21. ApJ**783:**L13.

Pinte, C., F. Ménard, G. Duchêne, and P. Bastien. 2006. Monte Carlo radiative transfer in protoplanetary disks. A&A**459:**797–804.

Pinte, C., D. L. Padgett, F. Ménard, K. R. Stapelfeldt, G. Schneider, J. Olofsson, O. Panić, J. C. Augereau, G. Duchêne, J. Krist, K. Pontoppidan, M. D. Perrin, C. A. Grady, J. Kessler-Silacci, E. F. van Dishoeck, D. Lommen, M. Silverstone, D. C. Hines, S. Wolf, G. A. Blake, T. Henning, and B. Stecklum. 2008. Probing dust grain evolution in IM Lupi's circumstellar disc. Multi-wavelength observations and modelling of the dust disc. A&A**489:**633–650.

Pudritz, R. E., R. Ouyed, C. Fendt, and A. Brandenburg. 2007. Disk Winds, Jets, and Outflows: Theoretical and Computational Foundations. Protostars and Planets V pages 277–294 .

Purcell, E. M. 1969. On the alignment of interstellar dust. Physica **41:**100–127.

Purcell, E. M. 1979. Suprathermal rotation of interstellar grains. The Astrophysical Journal **231:**404–416.

Purcell, E. M., and C. R. Pennypacker. 1973. Scattering and Absorption of Light by Nonspherical Dielectric Grains. ApJ**186:**705–714.

Purcell, E. M., and L. Spitzer, Jr. 1971. Orientation of Rotating Grains. ApJ**167:**31.

Quashnock, J. M., A. Loeb, and D. N. Spergel. 1989. Magnetic field generation during the cosmological qcd phase transition. Astrophys. J. Lett .

Rao, R., R. M. Crutcher, R. L. Plambeck, and M. C. H. Wright. 1998. High-Resolution Millimeter-Wave Mapping of Linearly Polarized Dust Emission: Magnetic Field Structure in Orion. The Astrophysical Journal Letters **502:**L75+.

Ricci, L., L. Testi, A. Natta, and K. J. Brooks. 2010. Dust grain growth in ρ-Ophiuchi protoplanetary disks. A&A**521:**A66.

Roberge, W. G., T. A. Degraff, and J. E. Flaherty. 1993. The Langevin Equation and Its Application to Grain Alignment in Molecular Clouds. ApJ**418:**287.

Roberge, W. G., and A. Lazarian. 1999. Davis-Greenstein alignment of oblate spheroidal grains. MNRAS**305:**615–630.

Russell, D. M., and R. P. Fender. 2008. Polarized infrared emission from X-ray binary jets. MNRAS**387:**713–723.

Sauter, J., S. Wolf, R. Launhardt, D. L. Padgett, K. R. Stapelfeldt, C. Pinte, G. Duchêne, F. Ménard, C.-E. McCabe, K. Pontoppidan, M. Dunham, T. L. Bourke, and J.-H. Chen. 2009. The circumstellar disc in the Bok globule CB 26. Multi-wavelength observations and modelling of the dust disc and envelope. A&A**505:**1167–1182.

Saviane, I. 2012. SOFI User's Manual, Issue 2.3.
URL `http://www.eso.org/sci/facilities/lasilla/instruments/sofi/doc/manual/sofiman_2p30.pdf`

Schmidtobreick and the IOT, L. 2011. Very Large Telescope Paranal Science Operations ISAAC User Manual, Issue 89.0.
URL `http://www.eso.org/sci/facilities/paranal/decommissioned/isaac/doc/VLT-MAN-ESO-14100-0841_v92.pdf`

Semenov, D., D. Wiebe, and T. Henning. 2006. Gas-Phase CO in Protoplanetary Disks: A Challenge for Turbulent Mixing. ApJ**647:**L57–L60.

Sen, A. K., R. Gupta, A. N. Ramaprakash, and S. N. Tandon. 2000. Imaging polarimetry of some selected dark clouds. A&AS**141:**175–183.

Shakura, N. I., and R. A. Sunyaev. 1973. Black holes in binary systems. Observational appearance. A&A**24:**337–355.

Shu, F. H. 1977. Self-similar collapse of isothermal spheres and star formation. ApJ**214:**488–497.

Stapelfeldt, K. R., J. E. Krist, F. Ménard, J. Bouvier, D. L. Padgett, and C. J. Burrows. 1998. An Edge-On Circumstellar Disk in the Young Binary System HK Tauri. ApJ**502:**L65–L69.

Stephens, I. W., L. W. Looney, C. D. Dowell, J. E. Vaillancourt, and K. Tassis. 2011. The Galactic Magnetic Field's Effect in Star-forming Regions. ApJ**728:**99.

Stephens, I. W., L. W. Looney, W. Kwon, C. L. H. Hull, R. L. Plambeck, R. M. Crutcher, N. Chapman, G. Novak, J. Davidson, J. E. Vaillancourt, H. Shinnaga, and T. Matthews. 2013. The Magnetic Field Morphology of the Class 0 Protostar L1157-mm. ApJ**769:**L15.

Stokes, G. G. 1852. On the Composition and Resolution of Streams of Polarized Light from different Sources. Transactions of the Cambridge Philosophical Society **9:**399–416.

Stutz, A. M., M. Rubin, M. W. Werner, G. H. Rieke, J. H. Bieging, J. Keene, M. Kang, Y. L. Shirley, K. Y. L. Su, T. Velusamy, and D. J. Wilner. 2008. Spitzer and HHT Observations of Bok Globule B335: Isolated Star Formation Efficiency and Cloud Structure. ApJ**687:**389–405.

Suzuki, T. K., and S.-i. Inutsuka. 2009. Disk Winds Driven by Magnetorotational Instability and Dispersal of Protoplanetary Disks. ApJ**691:**L49–L54.

Tarduno, J. A., R. D. Cottrell, M. K. Watkeys, A. Hofmann, P. V. Doubrovine, E. E. Mamajek, D. Liu, D. G. Sibeck, L. P. Neukirch, and Y. Usui. 2010. Geodynamo, Solar Wind, and Magnetopause 3.4 to 3.45 Billion Years Ago. Science **327:**1238–.

Tewes, M. 2010. cosmics.py: L.A.Cosmic in python.
URL `http://obswww.unige.ch/~tewes/cosmics_dot_py/`

Turner, N. J., S. Fromang, C. Gammie, H. Klahr, G. Lesur, M. Wardle, and X.-N. Bai. 2014. Transport and Accretion in Planet-Forming Disks. PP VI pages 411–432 .

Turner, N. J., T. Sano, and N. Dziourkevitch. 2007. Turbulent Mixing and the Dead Zone in Protostellar Disks. ApJ**659:**729–737.

Turnshek, D. A., R. C. Bohlin, R. L. Williamson, II, O. L. Lupie, J. Koornneef, and D. H. Morgan. 1990. An atlas of Hubble Space Telescope photometric, spectrophotometric, and polarimetric calibration objects. AJ**99:**1243–1261.

Unsöld, A., and B. Bascheck. 1988. Der neue Kosmos. Springer-Verlag.

Vallée, J. P. 2002. Empirical Radial Dependencies of the Energy Components in Magnetized Young Stellar Objects. AJ**123:**382–386.

Vallée, J. P., P. Bastien, and J. S. Greaves. 2000. Highly Polarized Thermal Dust Emission in the Bok Globule CB 068. ApJ**542:**352–358.

Vallée, J. P., and J. D. Fiege. 2007. The Cool Dark Globule CB68 and Its Associated Protostar: Geometry, Kinematics, Magnetic Vectors, and Pressure Balance. AJ**134:**628–636.

Vallée, J. P., J. S. Greaves, and J. D. Fiege. 2003. Magnetic Structure of a Dark Bok Globule. ApJ**588:**910–917.

van de Hulst, H. C. 1957. Light Scattering by Small Particles.

van Dokkum, P. G. 2001. Cosmic-Ray Rejection by Laplacian Edge Detection. PASP**113:**1420–1427.

Voshchinnikov, N. V. 2004. Optics of cosmic dust I. Astrophysics and Space Physics Reviews **12:**1.

Voshchinnikov, N. V., and V. G. Farafonov. 1985. Light scattering by dielectric spheroids. Part 1. Optics and Spectroscopy **58:**81–85.

Voshchinnikov, N. V., and V. G. Farafonov. 1993. Optical properties of spheroidal particles. Ap&SS**204:**19–86.

Voshchinnikov, N. V., V. B. Il'in, T. Henning, B. Michel, and V. G. Farafonov. 2000. Extinction and polarization of radiation by absorbing spheroids: shape/size effects and benchmark results. J. Quant. Spec. Radiat. Transf.**65:**877–893.

Vowles, H. P. 1932. Early evolution of power engineering. ISIS **17:**412.

Vrba, F. J., C. B. Luginbuhl, S. E. Strom, K. M. Strom, and M. H. Heyer. 1986. An optical imaging and polarimetric study of the LYNDS 723 and Barnard 335 molecular outflow regions. AJ**92:**633–636.

Wardle, J. F. C., and P. P. Kronberg. 1974. The linear polarization of quasi-stellar radio sources at 3.71 and 11.1 centimeters. ApJ**194:**249–255.

Waterman, P. C. 1971. Symmetry, Unitarity, and Geometry in Electromagnetic Scattering. Phys. Rev. D**3:**825–839.

Weingartner, J. C., and B. T. Draine. 2001. Dust Grain-Size Distributions and Extinction in the Milky Way, Large Magellanic Cloud, and Small Magellanic Cloud. ApJ**548:**296–309.

Weingartner, J. C., and B. T. Draine. 2003. Radiative Torques on Interstellar Grains. III. Dynamics with Thermal Relaxation. ApJ**589:**289–318.

Weintraub, D. A., A. A. Goodman, and R. L. Akeson. 2000. Polarized Light from Star-Forming Regions. PP IV page 247 .

Whittet, D. C. B., P. G. Martin, J. H. Hough, M. F. Rouse, J. A. Bailey, and D. J. Axon. 1992. Systematic variations in the wavelength dependence of interstellar linear polarization. ApJ**386:**562–577.

Wiesemeyer, H., T. Hezareh, E. Kreysa, A. Weiss, R. Güsten, K. M. Menten, G. Siringo, F. Schuller, and A. Kovacs. 2014. Submillimeter Polarimetry with PolKa, a Reflection-Type Modulator for the APEX Telescope. PASP**126:**1027–1047.

Williams, J. P., and L. A. Cieza. 2011. Protoplanetary Disks and Their Evolution. ARA&A**49:**67–117.

Wolf, S. 2003*a*. Efficient Radiative Transfer in Dust Grain Mixtures. ApJ**582:**859–868.

Wolf, S. 2003*b*. MC3D-3D continuum radiative transfer, Version 2. CPC **150:**99–115.

Wolf, S., T. Henning, and B. Stecklum. 1999. Multidimensional self-consistent radiative transfer simulations based on the Monte-Carlo method. A&A**349:**839–850.

Wolf, S., R. Launhardt, and T. Henning. 2003. Magnetic Field Evolution in Bok Globules. ApJ**592:**233–244.

Wolf, S., R. Launhardt, and T. Henning. 2004. Evolution of Magnetic fields in Bok Globules? Ap&SS**292:**239–246.

Wolf, S., L. Vanzi, and N. Ageorges. 2002*a*. How To Reduce SOFI/NTT Polarimetric Data.
URL `http://www.eso.org/sci/facilities/lasilla/instruments/sofi/tools/report.ps`

Wolf, S., N. V. Voshchinnikov, and T. Henning. 2002*b*. Multiple scattering of polarized radiation by non-spherical grains: First results. A&A**385:**365–376.

Wootten, A., and A. R. Thompson. 2009. The Atacama Large Millimeter/Submillimeter Array. IEEE Proceedings **97:**1463–1471.

Yen, H.-W., P. M. Koch, S. Takakuwa, P. T. P. Ho, N. Ohashi, and Y.-W. Tang. 2014. Observations of Infalling and Rotational Motions on a 1,000-AU Scale around 17 Class 0 and 0/I Protostars: Hints of Disk Growth and Magnetic Braking? ArXiv e-prints, accepted by ApJ.

Yun, J. L., and D. P. Clemens. 1994. Outflows from young stellar objects in BOK globules: Maps. ApJS**92:**145–161.

Acknowledgments

I would like to thank all those who supported me in writing this thesis. In particular, I thank

my advisor Prof. Dr. Sebastian Wolf for giving me the opportunity to conduct research in the fascinating field of astronomy, for his support, and the possibility to pursue my goals,

my collaborators, especially Prof. Dr. Himadri S. Das and Arindam Chakraborty from Assam University, India, for their support during the development of the IFOSC/IGO pipeline,

my proofreaders, Mandy, Stjepan, Flo, Steve, Jürgen, for criticizing, scrutinizing, and making suggestions to improve this thesis,

the Kiel astronomy group for continuous and enjoyable entertainment over the years,

and my family for their ongoing support of my drive for astronomy.

Erklärung

Hiermit erkläre ich, dass

1. die Arbeit, abgesehen von Beratung durch den Betreuer Prof. Dr. Sebastian Wolf, nach Inhalt und Form die eigene Arbeit ist, sofern nicht im Text ausdrücklich anders angegeben,

2. die Arbeit keiner anderen Stelle im Rahmen eines Prüfungsverfahrens vorgelegen hat oder vorliegt,

3. Teile der Arbeit veröffentlicht worden sind: Bertrang et al. (2014)

4. die Arbeit unter Einhaltung der Regeln guter wissenschaftlicher Praxis der Deutschen Forschungsgemeinschaft einstanden ist.

Gesa H.-M. Bertrang